CHEMISTRY AND APPLICATIONS OF METAL-ORGANIC MATERIALS

A Dissertation

by

DAN ZHAO

Submitted to the Office of Graduate Studies of
Texas A&M University
in partial fulfillment of the requirements for the degree of

DOCTOR OF PHILOSOPHY

December 2010

Major Subject: Chemistry

Chemistry and Applications of Metal-Organic Materials

CHEMISTRY AND APPLICATIONS OF METAL-ORGANIC MATERIALS

A Dissertation

by

DAN ZHAO

Submitted to the Office of Graduate Studies of
Texas A&M University
in partial fulfillment of the requirements for the degree of

DOCTOR OF PHILOSOPHY

Approved by:

Chair of Committee,	Hong-Cai Zhou
Committee Members,	Abraham Clearfield
	François P. Gabbaï
	Hung-Jue Sue
Head of Department,	David H. Russell

December 2010

Major Subject: Chemistry

ABSTRACT

Chemistry and Applications of Metal-Organic Materials. (December 2010)

Dan Zhao, B.A., Zhejiang University; M.S., Zhejiang University

Chair of Advisory Committee: Dr. Hong-Cai Zhou

Developing the synthetic control required for the intentional 3-D arrangement of atoms remains a holy grail in crystal engineering and materials chemistry. The explosive development of metal-organic materials in recent decades has shed light on the above problem. Their properties can be tuned by varying the organic and/or inorganic building units. In addition, their crystallinity makes it possible to determine their structures via the X-ray diffraction method. This dissertation will focus on the chemistry and applications of two kinds of metal-organic materials, namely, metal-organic frameworks (MOFs) and metal-organic polyhedra (MOP).

MOFs are coordination polymers. Their permanent porosity makes them a good "gas sponge". In the first section, an isoreticular series of MOFs with dendritic hexa-carboxylate ligands has been synthesized and characterized structurally. One of the MOFs in this series, PCN-68, has a Langmuir surface area as high as 6033 $m^2 g^{-1}$. The MOFs also possess excellent gas (H_2, CH_4, and CO_2) adsorption capacity.

In the second section, a NbO-type MOF, PCN-46, was constructed based on a polyyne-coupled di-isophthalate linker formed in situ. Its lasting porosity was confirmed

by N_2 adsorption isotherm, and its H_2, CH_4 and CO_2 adsorption capacity was examined at 77 K and 298 K over a wide pressure range (0-110 bar).

Unlike MOFs, MOP are discrete porous coordination nanocages. In the third section, a MOP covered with bulky triisopropylsilyl group was synthesized, which exhibits a thermosensitive gate opening property. This material demonstrates a molecular sieving effect at a certain temperature range, which could be used for gas separation purpose.

In the last section, a MOP covered with alkyne group was synthesized through kinetic control. The postsynthetic modification via click reaction with azide-terminated polyethylene glycol turned them into metallomicelles, which showed controlled release of an anticancer drug 5-fluorouracil.

In summary, two kinds of metal-organic materials have been discussed in this dissertation, with the applications in gas storage, gas separation, and drug delivery. These findings greatly enrich the chemistry and applications of metal-organic materials.

DEDICATION

To Shanshan, James, and Michael, for their love and patience.

To my parents, for their love and constant support.

ACKNOWLEDGEMENTS

I would like to thank my committee chair, Dr. Zhou, and my committee members, Dr. Clearfield, Dr. Gabbaï, and Dr. Sue, for their guidance and support throughout the course of this research. I will always appreciate my advisor, Dr. Zhou, for giving me the chance to work in his lab. His insightful guidance and generous support was critical for the completion of my degree.

The Zhou's lab was a wonderful place to work in. I've learned a lot from the visiting scholars, post-docs, and graduate student peers. I want to give my special thank to Dr. Daqiang Yuan and Dr. Daofeng Sun, for giving me valuable help in crystallography and organic synthesis. I also want to thank my collaborators, Dr. Li-Qun Wang in Zhejiang University and Dr. Rajamani Krishna in University of Amsterdam, for their help with the characterization and simulation of materials reported in this dissertation. Thanks also go to my friends and colleagues, and the department faculty and staff, for making my time at Texas A&M University a great experience.

Finally, thanks to my parents for their encouragement, and to my wife for her love. I also owe my sons, James and Michael, my time and appreciation. They teach me how to be patient and show gratitude for what has been offered.

NOMENCLATURE

5-FU	5-Fluorouracil
ANG	Adsorbed Natural Gas
BDC	Benzenedicarboxylate
BET	Brunauer, Emmett and Teller
BTC	1,3,5-Benzenetricarboxylate
CCS	Carbon Capture and Sequestration
CNG	Compressed Natural Gas
DEF	Diethyl Formamide
DLS	Dynamic Light Scattering
DMA	Dimethyl Acetamide
DMF	Dimethyl Formamide
DMSO	Dimethyl Sulfoxide
DOE	U.S. Department of Energy
EDS	Energy Dispersive Spectroscopy
FTIR	Fourier Transform Infrared Spectroscopy
GPC	Gel Permeation Chromatography
HPLC	High Performance Liquid Chromatography
INS	Inelastic Neutron Scattering
LNG	Liquefied Natural Gas
MALDI	Matrix Assisted Laser Desorption Ionization

MAMSs	Mesh-Adjustable Molecular Sieves
MD	Molecular Dynamics
MOFs	Metal-Organic Frameworks
MOP	Metal-Organic Polyhedra / Metal-Organic Polyhedron
MS	Mass Spectrometry
NG	Natural Gas
NbO	Niobium Oxide
NMR	Nuclear Magnetic Resonance
PCN	Porous Coordination Network
PEG	Polyethylene Glycol
PXRD	Powder X-Ray Diffraction
SBUs	Secondary Building Units
SEM	Scanning Electron Microscopy
TEM	Transmission Electron Microscopy
TGA	Thermogravimetry Analyses
THF	Tetrahydrofuran
TIPS	Triisopropylsilyl

TABLE OF CONTENTS

Page

LIST OF FIGURES

FIGURE Page

FIGURE Page

FIGURE Page

LIST OF TABLES

1. INTRODUCTION[†‡]

According to the definition given by George M. Whitesides, self-assembly is "the spontaneous, noncovalent association of two or more molecules under equilibrium conditions into stable, well-defined aggregates".[1] Typical noncovalent associations include ion-ion interactions, ion-dipole interactions, dipole-dipole interactions, hydrogen bonding, cation-π interactions, anion-π interactions, π-π interactions, van der Waals forces and crystal close packing, closed shell interactions, etc.[2] Among these interactions, the metal-ligand interactions (ion-ion interactions) typically offer greater strength and more rigidity due to stronger bonding interaction and direction. In recent years, there is a rapid development of metal-organic materials based on this interaction. This dissertation will focus on the chemistry and applications of two kinds of metal-organic materials, namely, metal-organic frameworks (MOFs) and metal-organic polyhedra (MOP).

This dissertation follows the style of *Inorganic Chemistry.*

[†]Reprinted with permission from "The Current Status of Hydrogen Storage in Metal-Organic Frameworks" by Zhao, D.; Yuan, D. Q.; Zhou, H. C., 2008. *Energy Environ. Sci.*, 1, 222-235, Copyright 2008 by Royal Society of Chemistry.

[‡]Reprinted in part with permission from "Potential Applications of Metal-Organic Frameworks" by Kuppler, R. J.; Timmons, D. J.; Fang, Q. R.; Li, J. R.; Makal, T. A.; Young, M. D.; Yuan, D. Q.; Zhao, D.; Zhuang, W. J.; Zhou, H. C., 2009. *Coord. Chem. Rev.*, 253, 3042-3066, Copyright 2009 by Elsevier.

MOFs are crystalline coordination polymers, containing organic ligands as the linkers and metal ions or clusters (secondary building units, SBUs) as the nodes (Figure 1).[3-5] Solvothermal reactions have proven to be an effective synthetic approach to synthesize MOFs. A routine solvothermal reaction procedure involves loading ligands (typically organic carboxylic acids), metal salts and solvents in thick-wall glass tubes, sealing the tubes under vacuum after flash freezing, and heating at elevated temperatures. With the proper conditions and good geometry match between the ligands and metal ions, crystalline products will form within several days. The nature of the solvothermal synthesis is actually a Lewis acid-base reaction, in which the deprotonated ligands act as Lewis bases while the metal ions serve as the Lewis acids. If the reaction goes too quickly, bulk precipitation occurs instead of the growth of single crystals. Modifying the reaction conditions so that the rate of ligand deprotonation matches that of the coordination bond formation is crucial. Solvents such as dimethyl formamide (DMF), diethyl formamide (DEF), and dimethyl acetamide (DMA) tend to undergo hydrolysis at elevated temperatures (60 °C – 85 °C), releasing amines capable of deprotonating the carboxylic acid ligands and facilitating the reaction. Without being hydrolyzed, dimethyl sulfoxide (DMSO) can be used at higher temperature conditions (100 °C or above), which helps to overcome the energy barrier and generate products with novel geometry. If necessary, the pH and polarity of the reaction media can be adjusted by adding inorganic acid or mixing in additional solvents. There is no universal reaction condition incorporating all ligands and metal ions, and different conditions are required for

specific ligand and metal ion combinations. It is here that experience and serendipity combine to give success.

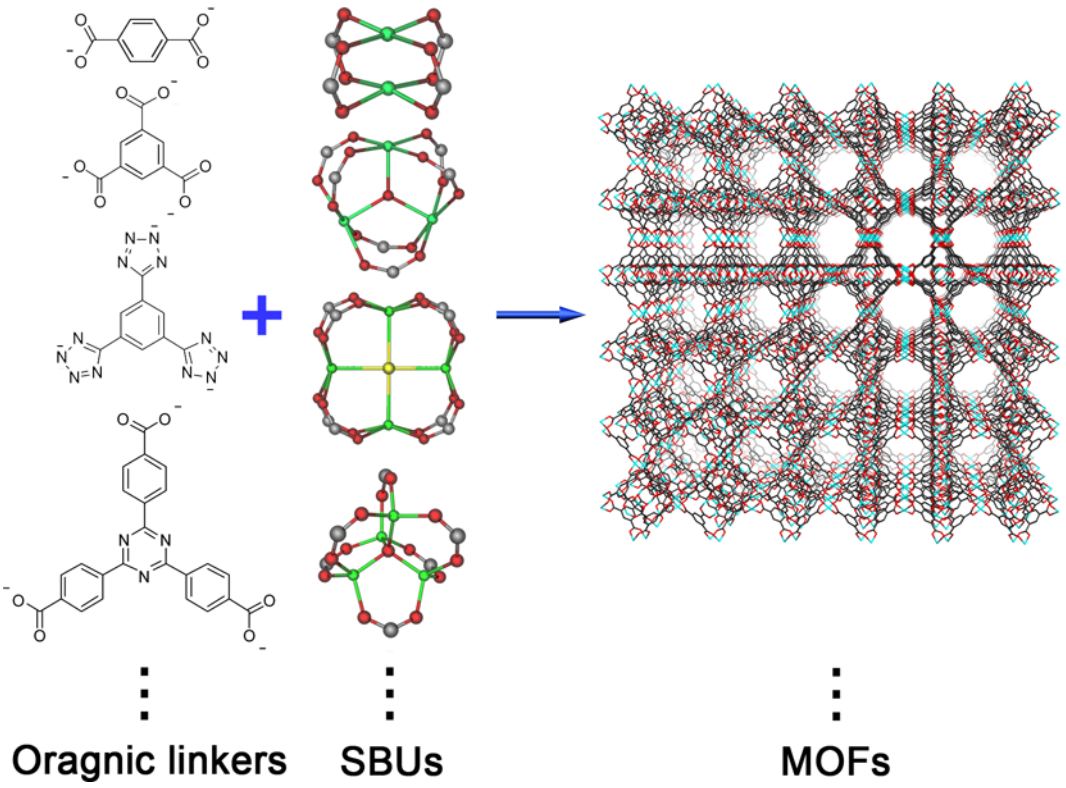

Figure 1. Illustration of MOFs' synthesis and chemical composition.

Unlike MOFs, which have infinite framework structure, MOP exist as discrete molecules, which offers them higher stability and special applications in solution chemistry. The synthesis of MOP single crystals suitable for X-ray diffraction study can be reached via either solvothermal reactions as MOFs, or recrystallization just like the small molecules. MOP are porous coordination nanocages and are represented by the

cuboctahedron nanoball formed between 12 dimetal paddlewheel clusters and 24 isophthalate structural moieties.[6-11] Due to their robust porous structure and versatile functionality, they have found applications as plasticizer, gas sponge, ion channel, coatings, and building units.[12-17]

The solvent or guest molecules, which occupy the pore spaces in MOFs or MOP, can be removed upon solvent exchange and heating under vacuum to generate a stable porous structure. Compared to their porous counterparts, such as zeolite and activated carbon, MOFs have much higher surface area. The porosity of MOP comes from the inner void of these discrete nanocages, although it is possible that the spacing between these nanocages contributes to their porosity as well.[13,18-20] The combination of different organic ligands and SBUs gives these metal-organic materials almost infinite geometrical and chemical variation, which makes them good candidates in gas storage and host-guest chemistry applications.

A tank charged with a porous adsorbent enables a gas to be stored at a much lower pressure than an identical tank without an adsorbent. This provides a safer and more economical gas storage method because high pressure tanks and multi-stage compressors can be avoided. Many gas storage studies have been conducted on porous adsorbents such as activated carbon, carbon nanotubes, and zeolites.[21] MOFs have received growing attention as such adsorbents due to their tunable pore geometries and flexible frameworks. The need to reduce global reliance on fossil fuels and the demand for carbon capture have pushed hydrogen, methane and carbon dioxide gases to the forefront of gas storage applications.

Albeit not a primary energy source, hydrogen is an ideal energy carrier. It almost triples the gravimetric heat of combustion of gasoline (120 MJ kg^{-1} *vs.* 44.5 MJ kg^{-1}).[22] More importantly, the energy-releasing procedure of hydrogen oxidation, in either an internal combustion engine or a fuel-cell stack, produces only water as a by-product. For a modern vehicle with a driving range of 400 km per tank of fuel, about 8 kg of hydrogen are needed for a combustion-engine-driven automobile and 4 kg for a fuel-cell-driven one.[23] Although these gravimetric requirements are far less demanding than that of gasoline (24 kg), hydrogen is notoriously difficult to compress for on-board storage. Volumetrically, even liquid hydrogen has a much smaller combustion heat than that of gasoline (8960 MJ m^{-3} *vs.* 31170 MJ m^{-3}). In the gas phase, 4 kg of hydrogen occupy 45 m^3 of space at room temperature and 1 atm.[23]

In order to facilitate the research and application of hydrogen as an energy carrier, the U.S. Department of Energy (DOE) reset the gravimetric and volumetric storage targets for on-board hydrogen storage for years 2010 (4.5 wt %, 28 g L^{-1}) and 2015 (5.5 wt %, 40 g L^{-1}).[24] These targets should be reached at ambient temperature (from -40 to 85 °C) and applicable pressure (less than 100 atm). Note that these are the goals for the system including container and any necessary accessories, the hydrogen storage capacity of the material itself should be even higher.

A safe and effective hydrogen storage technique has become the bottleneck for a possible hydrogen economy. High-pressure or cryogenic liquid hydrogen tanks have been certified worldwide and demonstrated in some prototype fuel-cell vehicles. However, their limited storage densities prevent them from reaching the DOE targets.

For example, high-pressure tanks can reach a pressure of 10000 psi (680 atm) with a 2.35 safety factor (23500 psi burst pressure). However, the heavy weight of the system offsets the gain in gravimetric storage density under pressurized conditions, and the volumetric density is far from that of liquid hydrogen (70.8 g L^{-1}). Cryogenic liquid-hydrogen tanks, on the other hand, can be used to improve the volumetric hydrogen storage capacity. However, about 20% of the recoverable energy is needed to liquefy the hydrogen and another 2% is spent to keep the tank cool.[22] The hydrogen storage capacity of the aforementioned tanks is demonstrated to be between 3.4 to 4.7 wt% gravimetrically and 14 to 28 g L^{-1} volumetrically.

In solid-state storage systems, a hydrogen atom/molecule either forms a strong chemical bond to a solid support (chemisorption) or interacts weakly with a sorbent (physisorption).

In chemisorption, dihydrogen molecules split into hydrogen atoms upon contacting the solid support. The highly reactive hydrogen atoms can form chemical bonds with the solid, leading to the formation of metal hydrides or chemical hydrides, depending on the nature of the solid support. Due to the short bonds between hydrogen and the solid, some hydride compounds can reach a relatively high hydrogen storage capacity. However, this strong bonding also leads to severe kinetic and thermodynamic problems during the charging and discharging procedures. Complete charging may take several hours, and the hydrogen-releasing temperature is typically very high (300 °C or higher).[25]

The physisorption method, on the other hand, stores hydrogen in the molecular form in a sorbent with a large surface area. The most frequently-studied sorbents are activated carbons, carbon nanostructures, zeolites, porous polymers, and metal-organic frameworks (MOFs). Because of the weak sorbent-sorbate interaction, physisorption-based hydrogen storage systems show fast kinetics with a charging time of minutes. However, the same weak interaction results in gravimetric hydrogen uptake of a sorbent at ambient temperature and applicable pressure of typically less than 2 wt%.

In 2003, Rosi *et al.* reported the first MOF-based hydrogen storage result.[26] Since then, the hydrogen storage capacities of more than 200 MOFs have been reported.[27] Although the DOE targets require hydrogen uptake measurements carried out at ambient temperature (from -40 to 85 °C) and applicable pressure (up to 100 atm), most reported hydrogen uptake measurements in MOFs are carried out at 77 K and 1 atm. This is largely because of the availability of that condition in commercially available gas adsorption equipment. Although far from DOE-target conditions, hydrogen uptake data obtained at low temperature and pressure are still useful in the initial exploration and comparison of hydrogen uptake capacities in different MOFs. As high-pressure hydrogen uptake measurement equipment becomes more widely available, more and more data of high-pressure hydrogen uptake in MOFs have been reported. At room temperature, the binding energy between hydrogen and the MOFs is comparable to thermal vibration energies, which leads to very poor hydrogen uptake (typically less than 1 wt%) and makes the comparison and discussion of hydrogen uptake capacity ambiguous and difficult. At the cryogenic condition, however, the relatively strong

interaction between hydrogen and MOFs (as compared to thermal energies) gives rise to greatly enhanced hydrogen uptake. This enhancement is so pronounced that some saturation hydrogen uptake data obtained at 77 K have reached or even surpassed the DOE targets.[28-30] Thus the comparison of saturation hydrogen uptake data at 77 K is more reliable and instructive in determining the MOFs' hydrogen uptake capacity.

By applying the Clausius-Clapeyron equation to two sets of hydrogen adsorption data collected at different temperatures (typically 77 K and 87 K), the isosteric heat of adsorption (ΔH_{ads}) can be deduced; this is an important criterion in judging how strongly hydrogen binds the MOFs.[30-31] In order to guarantee the validity of these ΔH_{ads} values, data sets should be collected at more than two different temperatures.

There are two criteria for the sorbent's hydrogen storage capacity: excess adsorption and absolute adsorption. Simply speaking, excess adsorption is a measurement of the gas molecules stuck to the surface of the sorbent, which is given directly from experimental measurements; while absolute adsorption includes both excess adsorption and gas molecules occupying the voids inside the sorbent.[32] From a practical viewpoint, absolute adsorption is more relevant for hydrogen storage applications. However, due to the difficulty in obtaining absolute adsorption data, which is estimated theoretically, most of the hydrogen uptake data reported are based on excess adsorption. Furukawa *et al.* proposed a simple equation for the conversion of these two values:

$$N_{abs} = N_{ex} + \rho_{bulk} V_{pore} \qquad \text{Equation 1}$$

where N_{abs} is the absolute adsorption value, N_{ex} is the excess adsorption value, ρ_{bulk} is the bulk density of hydrogen and V_{pore} is the pore volume of the sorbent.[32]

There are several factors influencing the hydrogen uptake in MOFs. The first and probably the foremost factor is the surface area and pore volume. There is a well-established positive relationship between the surface area and the hydrogen uptake in carbon-based sorbents.[33-34] Note that the linker portion of most MOFs is composed of aromatic ring motifs, which give rigidity to the framework. Such chemical composition is very similar to that of carbon materials, which are largely composed of sp^2-hybridized carbon atoms. A positive, roughly linear relationship between specific surface area and hydrogen uptake in MOFs can be observed by plotting the surface areas versus the 77 K saturation hydrogen uptake data (Figure 2).[28,35] The slope of the linear relationship is 1.45×10^{-3} wt% $(m^2\ g^{-1})^{-1}$ for the Langmuir surface area and 1.92×10^{-3} wt% $(m^2\ g^{-1})^{-1}$ for the BET surface area, which is comparable to the theoretical value for carbon (2.28×10^{-3} wt% $(m^2\ g^{-1})^{-1}$).[36] Theoretically, a minimum surface area of ~1400 $m^2\ g^{-1}$ is needed for a material to reach an excess adsorption of 6 wt% (or ~2100 $m^2\ g^{-1}$ for 9 wt%).[37]

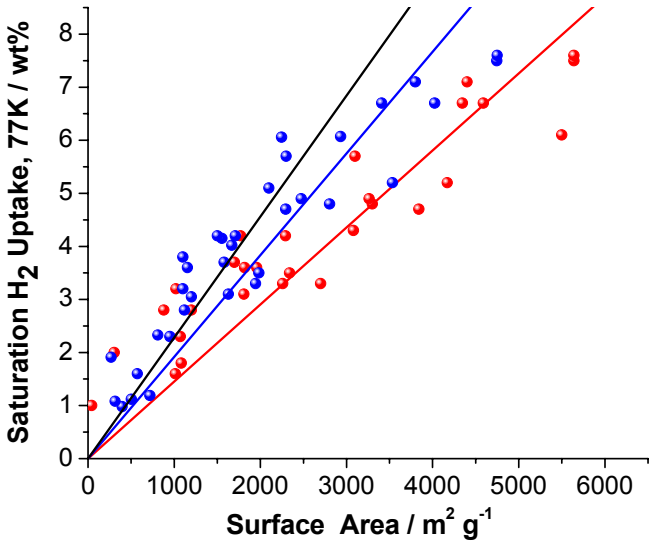

Figure 2. Correlation between surface area and saturation hydrogen uptake at 77 K (red: MOFs, Langmuir method; blue: MOFs, BET method; black: sp^2 carbon, theoretical).

The hydrogen uptake capacity of MOFs is not determined solely by the surface area. Small pores, which have stronger interaction with hydrogen due to the overlap of the potential fields from both sides of the pore walls, should have higher affinity towards hydrogen and thus higher hydrogen uptake capacity. One can deduce this conclusion from the hydrogen-binding energies in pure carbon materials, which range from 4 to 15 kJ mol^{-1}.[38] The lower value is common in flat carbon structures such as graphite, while the higher one is typical of internal and interstitial sites in carbon nanostructures, an indication that confined geometry can greatly enhance hydrogen-binding energy. Note that the kinetic diameter of hydrogen is 2.9 Å. Calculations based on carbon materials showed that a slit pore with a width of 6 Å has the highest hydrogen uptake at very low pressures because it exhibits the strongest interaction potential. A larger width of 9 Å was recommended for maximum hydrogen uptake capacity at high pressure.[39] In the

case of HKUST-1, both neutron powder diffraction and inelastic neutron scattering (INS) data support that hydrogen molecules are adsorbed into the smaller cage before the larger one, indicating a stronger interaction between hydrogen and the smaller pore.[40-41] This conclusion is confirmed indirectly by desorption studies of hydrogen in various MOFs (HKUST-1, MIL-53, MOF-5, and IRMOF-8), where the hydrogen desorbed first from the larger pore, then the smaller pore with increasing temperature.[42]

The influence of ligand structure on hydrogen uptake capacity of MOFs can be traced back to the first reported hydrogen uptake in MOFs, in which the authors proposed that using larger aromatic ligands would increase the hydrogen uptake capacity.[26] This idea is supported by other theoretical studies.[43-44] In some of these proposed MOFs, the organic linkers dominate the hydrogen adsorption while the metal clusters play only a lesser role,[43] in contrast to the initial INS study.[26] The same phenomenon is observed in zeolitic imidazolate frameworks, a kind of MOFs using imidazolate as the organic ligands. The neutron powder diffraction data on ZIF-8 indicated that the imidazolate organic linker was primarily responsible for hydrogen adsorption, suggesting a larger effect of linker modification on the hydrogen storage capacity.[45] In contrast to using a larger aromatic ring, the VASP *ab initio* computer calculations indicated that there is little effect on the hydrogen uptake capacity if the aromatic ring is substituted with halogen, and the added mass would be detrimental to the hydrogen uptake capacity.[46] This is confirmed experimentally. A systematic study by Chun *et al.* on the influence in hydrogen uptake capacity brought by the modulation of the organic ligands resulted in no direct relationship between the hydrogen uptake

capacity and the chemical composition of the organic ligands.[47] On the contrary, the authors suggested that the shape and size of channels instead of the ligands' chemical nature should be responsible for hydrogen uptake trend in their study. The same conclusion is drawn by Rowsell *et al.*, in which the low pressure hydrogen uptake measurements were done on a series of IRMOFs.[31]

In some MOFs, the solvent or guest molecules coordinatively bound to the metal node can be removed without the collapse of the framework by heating under vacuum. These MOFs, bearing coordinatively unsaturated metal sites, show higher hydrogen-binding energy. One example is the dicopper paddlewheel SBU, in which the removal of the axial ligands has been confirmed by single crystal X-ray diffraction.[48] The stronger interaction between hydrogen and the copper open sites has been demonstrated by IR spectroscopy.[49] Additionally, neutron powder diffraction revealed that the most favorable hydrogen binding sites are the unsaturated axial sites of the dicopper SBUs.[40] This is also consistent with an INS study.[41] The neutron powder diffraction study done on MOF-74 revealed the strong interaction between hydrogen and the exposed Zn^{2+} ions and indicated a strong correlation between the existence of unsaturated metal sites and the high hydrogen surface packing density.[37] Dincă *et al.* constructed a MOF with both exposed Mn^{2+} coordination sites and free Mn^{2+} within the channel.[30] Neutron powder diffraction data showed direct hydrogen binding at the unsaturated Mn^{2+} within the framework, with the maximum isosteric heat of adsorption 10.1 kJ mol^{-1}. The absolute hydrogen uptake is 6.9 wt% at 77 K and 90 bar with the density of the stored hydrogen 85% of that of liquid hydrogen. By replacing the coordinated Mn^{2+} with Cu^{2+}, a more

robust MOF is generated, which can be fully desolvated to expose a larger number of open metal sites.[50] A slightly decreased heat of adsorption of the generated copper MOF as compared to its manganese counterpart was explained by Jahn-Teller distortion of the coordination environment of the Cu^{2+} ions. Another explanation using spin state has been given by a computational study, which demonstrated that binding energy can be tuned in a range of about 10 to 50 kJ mol^{-1} using different transition metal ions.[51] Using the same MOF, Dincă *et al.* replaced the free Mn^{2+} cation with other cations to generate a series of isostructural MOFs.[52] There is an adsorption heat difference of 2 kJ mol^{-1} between the weakest and strongest hydrogen-binding MOFs; among them the Co^{2+}-exchanged MOF exhibites the highest heat of adsorption, 10.5 kJ mol^{-1}. A combined DFT and GCMC simulation study on MOF-505 showed that open metal sites have favorable impact on hydrogen adsorption in MOFs at low pressures, and the hydrogen molecule is inclined to expose the negative lobe of its quadrupole to the exposed copper atoms, which act as Lewis acids.[53] Although there are still some arguments about whether the unsaturated metal sites are the main reason for the increased interaction between hydrogen and the framework,[54] the combination of unsaturated metal sites with the appropriate pore size and geometry discussed above gives rise to some MOFs with strong hydrogen binding energies. In the case of $Mg_3(O_2C\text{-}C_{10}H_6\text{-}CO_2)_3$, where the Mg^{2+} centers are unsaturated and the pore dimensions are constricted, the hydrogen isosteric heat of adsorption reaches 9.5 kJ mol^{-1}.[55]

Another way to increase the binding energy between hydrogen and MOF is through chemical doping. Li^+ has been calculated to show a strong affinity for hydrogen

(~24 kJ mol^{-1}),[56] and *ab initio* calculations for Li-decorated MOF-5 indicated that a hydrogen uptake of 2.9 wt% at 200 K and 2.0 wt% at 300 K is achievable.[57] By direct reduction of the organic ligand with lithium metal, Mulfort *et al.* experimentally introduced lithium cations into MOFs.[58] Compared to the pristine MOF, the Li-doped MOF demonstrates a 75% increase in gravimetric hydrogen uptake, up to 1.63 wt% at 77 K and 1 atm. Furthermore, the isosteric heat of adsorption is greater in the Li-doped MOF over the entire loading range. In addition to cations, anions can also be helpful in hydrogen adsorption. For example, charge-separated ammonium fluorides are calculated to have enhanced binding energy towards molecular hydrogen.[59] Because it is well demonstrated that the hydrogen molecule can be dissociated into monoatomic hydrogen by certain heavy transition metals (e.g. Pt), making use of this "dissociation/spillover" in MOF-based hydrogen-storage system leads to a hydrogen uptake enhancement, increasing adsorbed hydrogen by a factor of 3.3 for MOF-5 and 3.1 for IRMOF-8.[60] In the latter exploration, by using a carbon bridge to facilitate the secondary spillover, the enhancement factor for IRMOF-8 has been increased to 8, resulting in a hydrogen uptake of 4 wt% at room temperature and 10 MPa, the highest among all the MOFs, with the entire process completely reversible.[61] The spillover effect has been reproduced by Liu *et al*.[62] Their results show the storage capacity of 1.14 and 0.63 wt% for MIL-101 and MIL-53 at 5.0 MPa and 293 K, which is greatly increased from that of pristine samples (0.37 wt% and none). In another approach, in which palladium was doped into MOF-5 via solution infiltration, the hydrogen adsorption capacity is increased by 62% to

1.86 wt% at 77 K and 1 atm.[63] However, according to the authors, the increase at low pressures does not necessarily imply a higher capacity at high pressures.

Sample preparation has been recognized in hydrogen uptake studies in MOFs as a key to obtaining repeatable and reliable data. For example, differences in the reported hydrogen uptake capacity in HKUST-1 are attributed to sample purity and activation.[64] During the degassing process, around 10 mPa is suggested as a satisfactory residual pressure.[65] The degassing temperature and time is also important. Navarro *et al.* demonstrated that activation at 105 °C gave almost neglectable hydrogen sorption in their sample, while 120 °C activation resulted in much better hydrogen uptake.[66] Generally speaking, the higher the temperature, the shorter the degassing time required. Within the temperature range in which the framework remains intact, the plot between the measured surface areas versus the degassing time gives the optimum degassing time where the plot reaches a plateau. In practice, a rough estimation about whether the degassing is complete can be made if the pressure keeps a stable value close to zero during degassing. Powder X-ray diffraction should be used to monitor the quality of the crystal before each hydrogen uptake measurement. Besides the sample quality and activation conditions, sample size can also potentially affect the accuracy of the measurement.[65] Too small a sample size would lead to larger uptake while too large a sample size may need more time for the sorption to reach equilibrium. For the volumetric method, an appropriate sample size is typically about 100 mg. In our own study, we have observed that a sample with small particle size has a larger hydrogen uptake than one with larger particle size. The possibility of the surface area difference

caused by the particle size has been ruled out because the increase of external surface area due to smaller particle size is neglectable compared to the much larger internal surface area. One possible explanation would be that in larger particles, the longer diffusion path limits access into the interior of the particle, either for the guest molecules coming out from the frameworks during activation or the hydrogen molecules going into the frameworks during adsorption. Besides, the chemical difference between the terminal and the inner parts of the particle should also be considered. It is possible that more unsaturated metal sites would be exposed at the surface of smaller particles than that of the larger one, leading to increased hydrogen uptake. Solvent exchange is also a crucial step in sample activation. By replacing the high-boiling-point and strongly-bound solvent or guest molecules (e.g. amide) with low-boiling-point and weakly-bound molecules (e.g. dichloromethane, chloroform, and methanol), the void inside the MOFs could be evacuated under moderate condition without framework collapse. Sample preparation is also important for material stability. For example, MOF-5, containing the Zn_4O motif, is proved to be unstable upon contact with moisture.[29,67-70] Kaye *et al.* modified the previously reported method to obtain a sample of MOF-5 with the highest surface area among the reported data, in which the exposure to water and air was minimized.[29] Their sample adsorbed 7.1 excess wt% hydrogen, and the absolute hydrogen uptake climbed to 11.5 wt% at 170 bar, with a volumetric storage density of 77 g L^{-1}, which is greater than the density of liquid hydrogen (70.8 g L^{-1}).

The MOFs-based hydrogen storage has been studied for more than seven years, and the future development direction should focus on (1) balancing between surface area

and pore size and (2) enhancing interaction between hydrogen and framework. GCMC simulations done on a series of isoreticular MOFs indicated three adsorption regimes.[71-72] At low pressure (less than 1 atm), the hydrogen uptake correlates with the heat of adsorption, while at high pressure the surface area and free volume become more important. Lin *et al.* constructed a series of MOFs with the same linkage but different length of ligands, leading to MOFs with the same topology but different pore sizes and surface areas. Hydrogen uptake measurements carried out at 77 K and under either 1 or 20 bar indicate that the MOF with the smallest pore size shows the strongest hydrogen-binding energy, while the highest gravimetric hydrogen uptake is achieved in the sample with the largest surface area.[73] A similar conclusion was drawn by Culp *et al*.[74] It follows that the ideal MOFs for hydrogen storage purpose should have high surface area for higher capacity and appropriate pore size for strong binding with hydrogen.[75] However, there is no simple relationship between these two factors. In the above two cases, these two factors are linked, with the smaller surface area MOF having smaller pores and the larger surface area MOF having larger pores. More work should be done to optimize the trade-off between surface area and pore size.

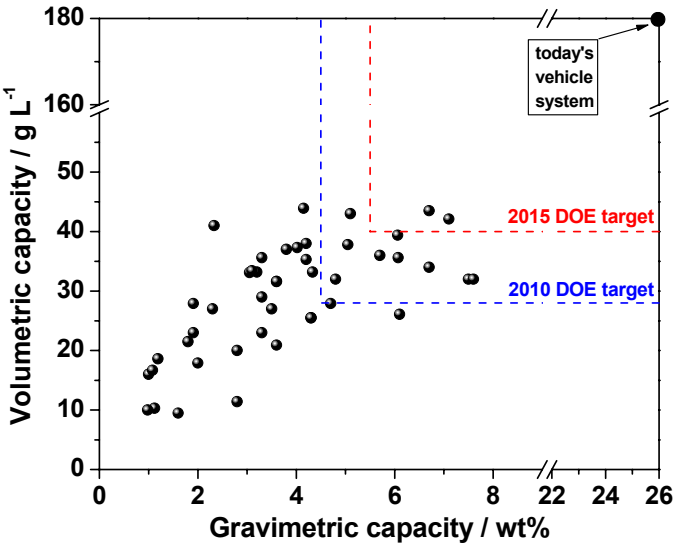

Figure 3. Current status of MOFs' hydrogen storage capacity at 77 K versus targets.

Up to now, the bottleneck for a MOF-based hydrogen storage system is the weak interaction between hydrogen and the framework. Figure 3 summarizes the current status of MOFs' hydrogen storage capacity at 77 K. Some of them have reached or even surpassed the DOE targets. However, the hydrogen uptake at ambient condition is almost neglectable. How strong an interaction between hydrogen and MOFs is needed to reach the DOE targets? Calculation done by Bhatia *et al.* indicated that an adsorption enthalpy of -15.1 kJ mol^{-1} is desired for optimum delivery of hydrogen between pressures of 1.5 and 30 bar at 298 K.[76] More importantly, this value of enthalpy should be kept consistently high throughout the hydrogen coverage range. The nature of the primary interaction between hydrogen and MOFs is also unclear. Theoretically, the interaction forces between molecular hydrogen with any system include weak van der Waals forces, electrostatic interactions, orbital interactions, and non-classical sigma

bonding (metal-dihydrogen complexes or the "Kubas complex").[56] In the case of MOFs, INS data indicated that there are two hydrogen-binding sites in MOF-5, with the stronger binding site associated with the metal-oxide cluster and the weaker one the organic linker.[26] These conclusions have been supported by both neutron powder diffraction and molecular dynamics simulation.[77-78] The IR spectroscopic study conducted by Bordiga *et al.* demonstrates that the interaction between hydrogen and MOF-5 is largely due to van der Waals interactions with the internal wall structure and to weak electrostatic forces associated with the metal-oxide cluster.[79] The isosteric heat of adsorption for hydrogen uptake in most MOFs lies in the range of 3.5 to 6.5 kJ mol^{-1}, and these values tend to decrease with increasing amount of hydrogen due to the formation of a hydrogen monolayer on available surfaces.[22] Clearly, the inherently weak interaction between hydrogen and MOFs would not meet the interaction requirement discussed above. Although the introduction of unsaturated metal sites into MOFs is an effective way to increase the hydrogen binding energy, the enhancement of hydrogen uptake in this way is limited due to the short-range nature of this interaction. In the case of HKUST-1, the enhancement is only around 1 wt% if each copper open site can bind one hydrogen molecule, and the enhanced uptake is limited to a very narrow pressure range (below 0.3 bar),[49] leading to poor delivery capacity.[32] Spillover might be a plausible method to strengthen the hydrogen binding were it not for the unpredictable hydrogen uptake enhancement factor. In contrast with the initial impressive report (enhancement factor of 8 for IRMOF-8),[61] other studies only show a moderate effect (enhancement factor of 2.08-3.2).[62,67,69] In addition, the usage of expensive and environmentally harmful heavy

transition metals would greatly limit large scale application of this method. Introducing charges into the MOFs would be a good method to increase the interaction. Since there is neither charge nor dipole moment in the dihydrogen molecule, the highest-energy interactions between a point charge and hydrogen are through the quadrupole moment, which is ~3.5 kJ mol^{-1} at 3 Å separation, and via charge-induced dipole interaction, with an energy ~6.8 kJ mol^{-1} at 3 Å separation.[56] Calculations done by Garberoglio *et al.* find that electrostatic charges on MOFs would substantially increase the hydrogen uptake at 77 K and low pressure, but the effect on high pressure uptake is only marginal, with minimal effect on room temperature hydrogen uptake.[80] Eddaoudi *et al.* have prepared ionic MOFs that show high hydrogen uptake and isosteric heat of adsorption, which, according to their explanation, is due to the narrow pore and highly localized charge density.[81-82] The corresponding calculation study confirmed the speculation that polarization interactions are significantly enhanced by the presence of a charged framework with confined pores, which makes these MOFs excellent hydrogen storage candidates.[83] The same conclusion has been drawn based on theoretical study of other charged carbon materials. GCMC simulation on charged single-walled carbon nanotubes demonstrates that a hydrogen uptake increase of ~10%-20% for 298 K and 15%-30% for 77 K is achievable in realistically charged (0.1 e per carbon atom) nanotubes compared to uncharged ones.[84] In order to achieve the DOE targets, however, the charges on the nanotubes need to be unrealistically large, which is both theoretically and experimentally impossible. A more optimistic conclusion is given by the first-principles calculations on charged fullerenes, in which the binding strength for hydrogen could be enhanced to a

desirable range for potential near ambient applications with a maximum storage capacity of up to ~8.0 wt%.[85]

The main hurdle to increase the hydrogen uptake in MOFs is the weak interaction between dihydrogen and the framework; this remains largely a challenge despite the recent surge in such studies. The DOE targets for on-board hydrogen storage pose a formidable challenge to those who are interested in solving such a fundamental but rewarding problem. The on-board hydrogen storage goal can only be achieved if theorists and experimentalists work together to find revolutionary systems based on basic studies including those reviewed above.

Natural gas (NG) is another good candidate for on-board fuel. The main component of NG is methane (>95%), while the rest is a mixture of ethane, other hydrocarbons, nitrogen, and carbon dioxide.[86] Methane has a comparable gravimetric heat of combustion with gasoline (50.0 MJ/kg *vs.* 44.5 MJ/kg),[22] but it also suffers from the lack of effective storage. The liquefied natural gas (LNG) can afford about 72% of the volumetric energy density of gasoline yet requires cryogenic conditions (112 K). The compressed natural gas (CNG) can offer about 26% of the volumetric energy density of gasoline but operates at pressures about 200 bar.[86] The adsorbed natural gas (ANG) provides another storage method in which NG is adsorbed on porous adsorbent, and an ANG (at 500 psig) volumetric storage energy density up to 80% of that of CNG (at 3000 psig) has been reported in the literature.[86]

Compared to CNG, ANG offers some advantages. Since it can operate under relatively low pressure, the expensive multi-stage gas compressor is not necessary. In

addition, conformable gas tanks can be used, which can maximize storage room and save the cargo space. The key factor that determines the effectiveness of ANG is the adsorbents used. Due to the easy availability and high surface area, carbonaceous materials (activated carbon) are mostly used as adsorbent materials. The theoretical maximum methane uptake capacity of activated carbon was calculated to be 200 v/v.[87] The methane uptake research in activated carbon is focused on improving the packing density while retain the high surface area and high micropore volume unchanged.

As a kind of newly emerged porous materials, MOFs are good substitutes for the traditional carbonaceous adsorbents for methane storage. In 1997, Kondo *et al.* reported the first methane sorption study using MOFs.[88] Unlike hydrogen, the heat of adsorption for methane (about 20 kJ/mol) is already within the ideal scope for practical usage. DOE has set a methane storage target: 180 v/v at ambient temperature and pressure no more than 35 bar.[89] Some of the carbon materials have already reached this target.[86] However, as carbon materials have a limited packing density, the key issue is increasing the surface area on the volumetric basis for the porous sorbent. The real breakthrough for MOF-based methane storage is achieved in PCN-14.[90] At 290 K and 35 bar, the absolute methane adsorption capacity in PCN-14 is 230 v/v, which is 28 % higher than the DOE target. The heat of adsorption at low loading is as high as 30 kJ/mol, indicating strong interactions between methane and the network. This incredibly high methane uptake capacity may come from (1) the ligand adip, which is derived from anthracene with an extended π system and stronger gas interaction; (2) the NbO type network constructed

from the squashed cuboctahedral cages that can trap gas; (3) the relatively high crystal density.

One point of concern is that uptake data calculations are based on the MOFs' crystallographic density, which is higher than the packing density due to the void generated by particle packing.[91] More methane uptake data needs to be calculated from the MOFs real packing density from MOFs in order to evaluate the potential of MOFs in methane storage.

The aggravated global warming, which is partially attributed to the increasing carbon dioxide concentration in the air, has aroused worldwide concerns. Carbon capture and sequestration (CCS), a process involving the capture of carbon dioxide from the air and sequestering it underground, has been proposed as a feasible way to control the atmospheric carbon dioxide concentration.[92] Using porous materials to capture carbon dioxide based on the sorption mechanism will be an energy-conserving alternative approach. The study of MOF-based carbon dioxide capture is growing dramatically.[93] A gravimetric capacity of 40 mmol g^{-1} has been obtained in NH_4F-treated MIL-101.[94] In another case, at 35 bar, a container filled with MOF-177 can store 9 times the amount of CO_2 in an empty container.[95] In addition, by functionalizing the unsaturated metal centers in MOFs with ethylenediamine, a much stronger CO_2 binding indicating chemisorption was achieved in a triazolate-bridged MOF.[96] The MOFs-based CCS is still in its infancy and we should be able to see its dramatic development in the near future.

2. RATIONAL DESIGN TOWARDS STABLE METAL-ORGANIC FRAMEWORKS WITH RECORD-HIGH SURFACE AREA AND EXCEPTIONALLY HIGH GAS UPTAKE CAPACITY[†‡]

2.1 Introduction

The efficacy of MOFs, especially for applications in gas storage, depends largely on the surface area. Up to now, finding high surface area materials still remains within the old "trial and error" mode, in which serendipity dominates. Compared to their porous counterparts, such as activated carton and zeolites, MOFs have atomic-scale tunable pore size and geometry, which makes the rational design towards record-high surface area materials possible.[3,97-102]

[†]Reproduced with permission from "Stabilization of Metal-Organic Frameworks with High Surface Areas by the Incorporation of Mesocavities with Microwindows" by Zhao, D.; Yuan, D. Q.; Sun, D. F.; Zhou, H. C., 2009. *J. Am. Chem. Soc.*, 131, 9186-9188, Copyright 2009 by American Chemical Society.
[‡]Reproduced with permission from "An Isoreticular Series of Metal-Organic Frameworks with Dendritic Hexacarboxylate Ligands and Exceptionally High Gas-Uptake Capacity" by Yuan, D. Q.; Zhao, D.; Sun, D. F.; Zhou, H. C., 2010. *Angew. Chem., Int. Ed.*, 49, 5357-5361, Copyright 2010 by Wiley-VCH.

Yaghi and coworkers indicated that exposing the latent edges of phenyl rings within MOFs can lead to significant enhancement of specific surface area, which may serve as a general strategy towards high surface area MOFs.[103] Ligand extension is a good way to realize this strategy, which has been proved by calculations on two series of isoreticular MOFs.[104-105] However, the discrepancy between the calculated surface areas and the experimental ones becomes larger as the ligand extension enhanced, which is attributed to the defects in the crystal structure or partial collapse of the framework.[104] In addition, due to the inherent weak coordination bond, when the length of the ligand increases, decreased stability of the generated framework and reduced porosity imposed by interpenetration are almost unavoidable.[106-107] The solution of this dilemma largely relays on whether the stability and porosity can be reconciled.

MOP are commonly found either as discrete nanoballs or as building blocks within MOFs.[6-11,19,108-118] The MOP based MOFs may have higher stability due to MOP's integrity and lower chance of forming interpenetrated structures owing to MOP's bulkiness. Among those MOP, cuboctahedron is very common, which is constructed with 12 dimetal paddlewheel secondly building units (SBUs) and 24 isophthalates or their derivatives.[6-10] This MOP can be integrated to form 3D MOF via either coordination bond or covalent bond.[112-113,115-118] Among those building approach, a (3-24)-connected network is reported recently, which is achieved by connecting the 24 edges of cuboctahedron with C_3 symmetric linker.[115-117] Based on this connection mode, a series of isoreticular MOFs is possible by changing the length of the C_3 symmetric linker while keeping the cuboctahedra building block unchanged. In this section, we

designed and synthesized four rigid nanosized hexatopic ligands, and compared the generated MOFs' stability and porosity (Figure 4). The key of this work is to find out whether 1) isoreticular MOFs based on (3,24)-connected network is achievable; 2) the stabilization of MOFs from the cuboctahedra will offset the destabilization of the MOFs by ligand extension; 3) surface area will increase along with the ligand extension; 4) surface area increase helps to boost the gas uptake capacity as well.

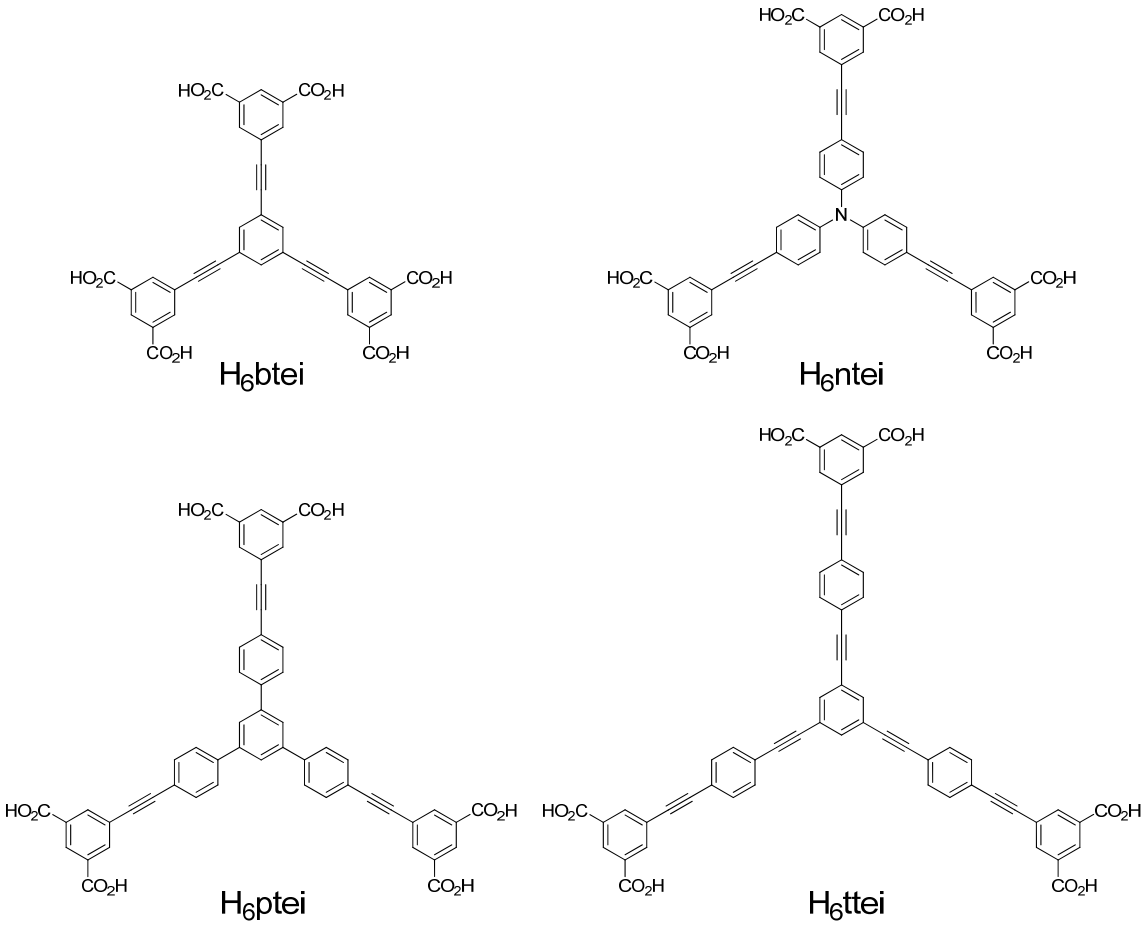

Figure 4. Nanoscopic ligand precursors.

2.2 Experimental Section

Materials and methods. Commercially available reagents were used as received without further purification. Nuclear magnetic resonance (NMR) data were collected on a Bruker Avance 200 MHz NMR spectrometer or on a Mercury 300 MHz NMR spectormeter. Elemental analyses (C, H, and N) were obtained from Canadian Microanalytical Service, Ltd. Thermogravimetry analyses (TGA) were performed under N_2 on a PerkinElmer TGA 7 or on a SHIMADZU TGA-50, with a heating rate of 5 °C min^{-1}. Powder X-ray diffraction (PXRD) patterns were obtained on a Scintag X1 powder diffractometer system using Cu-K_α radiation with a variable divergent slit, solid-state detector, and a routine power of 1400 W (40 kV, 35 mA) or on a BRUKER D8-Focus Bragg-Brentano X-ray Powder Diffractometer equipped with a Cu sealed tube (λ = 1.54178) at a scan rate of 0.2 s deg^{-1}, solid-state detector, and a routine power of 1400 W (40 kV, 35 mA). The simulation of the PXRD spectrum was carried out by the single-crystal data and diffraction-crystal module of the *Mercury* program available free of charge *via* internet at *http://www.ccdc.cam.ac.uk/products/mercury/.* Scanning electron microscopy (SEM) images were taken on a Zeiss Supra 35 VP FEG SEM or a JEOL JSM-840A SEM. The samples were coated with gold before observation.

Synthesis of 1,3,5-tris(2-diethyl isophthalate-1-ethynyl)benzene, 1. 1,3,5-tribromobenzene (2.00 g, 6.35 mmol), diethyl-5-(ethynyl)isophthalate (6.25 g, 25.4 mmol),[119] $Pd(PPh_3)_2Cl_2$ (442 mg, 0.63 mmol), PPh_3 (330 mg, 1.26 mmol), and CuI (240 mg, 1.26 mmol) were mixed in a 500 mL three neck Schlenk flask. The flask was pumped under vacuum and refilled with N_2 for three times, and then 200mL of freshly

distilled and degassed triethylamine was added. The mixture was heated to reflux under nitrogen atmosphere for 64 hours. After removal of organic solvent, the residue was dissolved in chloroform (150 mL) and washed with water (100 mL). The aqueous layer was back-extracted with chloroform (3 × 50 mL), and the combined organic layers were dried over $MgSO_4$ and filtered. The solvent was removed and the crude product was purified by column chromatography on silica gel with 40:1 chloroform/EtOAc to give compound **1** as a pale yellow solid. ^{1}H NMR (200 MHz, $CDCl_3$): δ = 8.69 (t, 3H, J = 1.6 Hz), 8.41 (d, 6H, J = 1.6 Hz), 7.78 (s, 3H), 4.47 (q, 12H, J = 7.1 Hz), 1.48 (t, 18H, J = 7.1 Hz).

Synthesis of 5,5',5''-benzene-1,3,5-triyltris(1-ethynyl-2-isophthalic acid), H_6btei. Compound **1** (5.00 g, 6.17 mmol) was suspended in 100 mL of THF, to which 150 mL of 1 M KOH aqueous solution was added. The mixture was stirred under reflux for 4 hours. THF was removed using a rotary evaporator, and diluted hydrochloric acid was added to the remaining aqueous solution until it became acidic. The precipitate was collected by filtration, washed with water and dried under vacuum to give H_6btei as a yellow solid. ^{1}H NMR (200 MHz, DMSO-d_6): δ = 13.63 (br, 6H), 8.50 (t, 3H, J = 1.6 Hz), 8.33 (d, 6H, J = 1.6 Hz), 8.01 (s, 3H).

Synthesis of hexaethyl 5,5',5''-(4,4',4''-nitrilotris(benzene-4,1-diyl)tris(ethyne-2,1-diyl)) -triisophthalate, 2. Tris(4-ethynylphenyl)amine (1.69 g, 5.0 mmol),[120] diethyl-5-(iodo)isophthalate (6.96 g, 20.0 mmol),[119] $Pd(PPh_3)_4$ (580 mg, 0.50 mmol), and CuI (95 mg, 0.50 mmol) were mixed in a 250 mL three neck Schlenk flask. The flask was pumped under vacuum and refilled with N_2 for three times, and then 100

mL of freshly distilled and degassed triethylamine was added. The mixture was heated to reflux under nitrogen atmosphere for 72 hours. After removal of organic solvent, the residue was dissolved in chloroform (200 mL) and washed with water (150 mL). The aqueous layer was back-extracted with chloroform (3 × 50 mL), and the combined organic layers were dried over $MgSO_4$ and filtered. The solvent was removed and the crude product was purified by column chromatography on silica gel with chloroform to give compound **2** as a green solid. ^{1}H NMR (200 MHz, $CDCl_3$): δ = 8.60 (s, 3H), 8.34 (s, 6H), 7.47 (d, 6H, J = 8.7 Hz), 7.12 (d, 6H, J = 8.7 Hz), 4.42 (q, 12H, J = 7.2 Hz), 1.43 (t, 18H, J = 7.2 Hz).

Synthesis of 5,5',5''-(4,4',4''-nitrilotris(benzene-4,1-diyl)tris(ethyne-2,1-diyl))triisophthalic acid, H_6ntei. Compound **2** (3.00 g, 6.13 mmol) was suspended in 50 mL of THF and 50 mL of methanol, to which 50 mL of 3 M KOH aqueous solution was added. The mixture was stirred under reflux for 4 hours. THF was removed using a rotary evaporator, and diluted hydrochloric acid was added to the remaining aqueous solution until it became acidic. The precipitate was collected by filtration, washed with water, and dried under vacuum to give H_6ntei as a yellow solid. ^{1}H NMR (200 MHz, DMSO-d_6): δ = 13.35 (br, 6H), 8.43 (s, 3H), 8.23 (s, 6H), 7.61 (d, 6H, J = 8.7 Hz), 7.13 (d, 6H, J = 8.7 Hz).

Synthesis of hexaethyl tetraethyl 5,5'-((5'-(4-((3,5-bis(ethoxycarbonyl)phenyl)ethynyl)phenyl)-[1,1':3',1''-terphenyl]-4,4''-diyl)bis(ethyne-2,1-diyl))diisophthalate, 3. 1,3,5-tris-(4-ethynylphenyl)benzene (1.00 g, 2.64 mmol),[121] diethyl-5-(iodo)isophthalate (4.60 g, 13.2 mmol),[119] $Pd(PPh_3)_4$ (460 mg),

and CuI (6 mg) were mixed in a 250 mL three neck Schlenk flask. The flask was pumped under vacuum and refilled with N_2 for three times, and then 150 mL of freshly distilled and degassed mixture solution of triethylamine and THF (1:1) was added. The mixture was heated to reflux under nitrogen atmosphere for 72 hours. After removal of organic solvent, the residue was dissolved in dichloromethane (200 mL) and washed with saturated aqueous solution of NH_4Cl (150 mL). The aqueous layer was back-extracted with chloroform (3 × 50 mL), and the combined organic layers washed with brine and were dried over $MgSO_4$ and filtered. The solvent was removed and the crude product was purified by column chromatography on silica gel with dichloromethane to give compound **3** as a yellow-green solid. ^{1}H NMR (300 MHz, $CDCl_3$): δ = 8.643 (t, 3H, J = 1.6 Hz), 8.396 (d, 6H, J = 1.6 Hz), 7.841 (s, 3H), 7.746 (d, 6H, J = 8.4 Hz), 7.691 (d, 6H, J = 8.4 Hz) 4.441 (q, 12H, J = 7.1 Hz), 1.443 (t, 18H, J = 7.1 Hz).

Synthesis of 5,5'-((5'-(4-((3,5-dicarboxyphenyl)ethynyl)phenyl)-[1,1':3',1''-terphenyl]-4,4''-diyl)-bis(ethyne-2,1-diyl))diisophthalic acid, H_6ptei. Compound **3** (1.04 g, 1.00 mmol) was suspended in 50 mL of THF and 50 mL of methanol, to which 50 mL of 5 M KOH aqueous solution was added. The mixture was stirred under reflux for 4 hours. Organic solvent was removed using a rotary evaporator, and diluted hydrochloric acid was added to the remaining aqueous solution until it became acidic (pH = 2 ~ 3). The precipitate was collected by filtration, washed with water, and dried under vacuum to give H_6ptei as a yellow-green solid. Yeild: 85%. ^{1}H NMR (300 MHz, DMSO-d_6): δ = 13.501 (br, 6H), 8.459 (t, 3H, J = 1.6 Hz), 8.292 (d, 6H, J = 1.6 Hz), 8.076 (s, 3H), 8.056 (d, 6H, J = 8.3 Hz) 7.781 (d, 6H, J = 8.3 Hz). ^{13}C NMR (300 MHz,

DMSO-d_6): δ = 165.90, 140.62, 140.27, 135.50, 132.15, 132.09, 129.76, 127.44, 123.28, 121.08, 90.85, 88.39.

Synthesis of hexaethyl 5,5',5''-(((benzene-1,3,5-triyltris-(ethyne-2,1-diyl))tris(benzene-4,1-diyl))-tris(ethyne-2,1-diyl))triisophthalate, 4. 1,3,5-tribromobenzene (240 mg, 0.77 mmol), diethyl-5-[(4-ethynylphenyl)ethynyl]isophthaloate (1.07 g, 3.1 mmol),[119] $Pd(PPh_3)_4$ (360 mg, 0.31 mmol), and CuI (31 mg, 0.16 mmol) were mixed in a 100 mL three neck Schlenk flask. The flask was pumped under vacuum and refilled with N_2 for three times, and then 50 mL of freshly distilled and degassed mixture solution of triethylamine and THF (4:1) was added. The mixture was heated to reflux under nitrogen atmosphere for 48 hours. After removal of organic solvent, the residue was dissolved in dichloromethane (100 mL) and washed with water (100 mL). The aqueous layer was back-extracted with dichloromethane (3 × 30 mL), and the combined organic layers were dried over $MgSO_4$ and filtered. The solvent was removed and the crude product was purified by column chromatography on silica gel with dichloromethane / ethyl acetate (9:1) to give compound **4** as a pale yellow solid. Yield: 42% ^{1}H NMR (300 MHz, $CDCl_3$): δ = 8.636 (s, 3H), 8.364 (s, 6H), 7.675 (s, 3H) 7.652 (d, 6H), 7.554 (br, 12H), 4.437 (q, 12H, J = 7.2 hz) 1.437 (t, 18H, J = 7.2 Hz).

Synthesis of 5,5',5''-(((benzene-1,3,5-triyltris(ethyne-2,1-diyl))tris(benzene-4,1-diyl))tris-(ethyne-2,1-diyl))triisophthalic acid, H_6ttei. Compound **4** (0.55 g, 0.50 mmol) was suspended in 50 mL of THF and 50 mL of methanol, to which 30 mL of 5 M KOH aqueous solution was added. The mixture was stirred under reflux for overnight.

Organic solvent was removed using a rotary evaporator, and diluted hydrochloric acid was added to the remaining aqueous solution until it became acidic (pH = 2 ~ 3). The precipitate was collected by filtration, washed with water and dried under vacuum to give H_6bttei as a yellow solid. Yield: 80%. ^{1}H NMR (300 MHz, DMSO-d_6): δ = 13.62 (br, 6H), 8.454 (s, 3H) 8.278 (s, 6H), 7.841 (s, 3H), 7.722 (d, 6H, J = 8.6), 7.672 (d, 6H, J = 8.6). ^{13}C NMR (300 MHz, DMSO-d_6): δ = 166.22, 136.06, 134.52, 132.36, 132.26, 130.37, 127.11, 123.88, 123.55, 122.75, 122.71, 90.91, 90.81, 90.02, 89.94. MS (ESI): m/z: 941.5 $[M]^-$.

Synthesis of PCN-60. H_6btei (100 mg, 1.6×10^{-4} mol) and $ZnBr_2$ (300 mg, 1.3×10^{-3} mol) were dissolved in 15 mL of DMF in a vial. The vial was tightly capped and placed in a 75 °C oven for 72 h to yield 86 mg of amber block crystals (yield: 34% based on H_6btei). The crystal has a formula of $[Zn(H_2O)]_3$(btei)·9DMF·$5H_2O$, which was derived from crystallographic, elemental analysis (% calc/found: C 46.29/46.32, H 5.61/5.02, N 7.71/7.76), and TGA.

Synthesis of PCN-61. H_6btei (100 mg, 1.6×10^{-4} mol) and $Cu(NO_3)_2 \cdot 2.5H_2O$ (300 mg, 1.3×10^{-3} mol) were dissolved in 15 mL of DMF with 9 drops of HBF_4 in a vial. The vial was tightly capped and placed in a 75 °C oven for 72 h to yield 218 mg of turquoise block crystals (yield: 94% based on H_6btei). The crystal has a formula of $[Cu(H_2O)]_3$(btei)·5DMF·$4H_2O$, which was derived from crystallographic data, elemental analysis (% calc/found: C 46.45/46.97, H 4.66/4.88, N 5.31/5.21), and TGA.

Synthesis of PCN-66. H_6ntei (50 mg, 6.2×10^{-5} mol) and $CuCl_2 \cdot 2H_2O$ (150 mg, 8.8×10^{-4} mol) were dissolved in 15 mL of DMA with 20 drops of HBF_4 in a vial. The

vial was tightly capped and placed in a 85 °C oven for 72 h to yield 80 mg of turquoise block crystals (yield: 42% based on H_6ntei). The crystal has a formula of $[Cu(H_2O)]_3$(ntei)·21DMA·10H_2O, which was derived from crystallographic data, elemental analysis (% calc/found: C 51.84/51.82, H 7.78/7.56, N 10.08/10.05), and TGA.

Synthesis of PCN-68. H_6ptei (50 mg, 5.74×10^{-5} mol) and $Cu(NO_3)_2$·2.5H_2O (150 mg, 6.45×10^{-4} mol) were dissolved in 15 mL of *N*,*N*-dimethylformamide (DMF) in a vial, to which 10 drops of HBF_4 were added. The vial was tightly capped and placed in a 75 °C oven for 12 h to yield 136 mg of green block crystals (yield: 63% based on H_6ptei). The crystal has a formula of $[Cu(H_2O)]_3$(ptei)·13H_2O·33DMF, which was derived from crystallography data, elemental analysis (% calc/found: C 48.93/48.89, H 7.70/7.64, N 12.31/12.53), and TGA.

Synthesis of PCN-610. H_6ttei (50 mg, 5.30×10^{-5} mol) and $Cu(NO_3)_2$·2.5H_2O (150 mg, 6.45×10^{-4} mol) were dissolved in 15 mL of *N*,*N*-dimethylformamide (DMF) in a vial, to which 10 drops of HBF_4 were added. The vial was tightly capped and placed in a 75 °C oven for 36 h to yield 72 mg of green block crystals (yield: 47% based on H_6ttei). The crystal has a formula of $[Cu(H_2O)_3]$(ttei)·19H_2O·22DMF, which was derived from crystallography data, elemental analysis (% calc/found: C 48.27/48.40, H 7.02/6.98, N 9.38/9.68), and TGA.

X-ray crystallography. Single crystal X-ray data of PCN-60 and PCN-61 were collected on a Bruker AXS Proteum-R 6000 X-ray diffractometer outfitted with a Cu rotating-anode X-ray source (FR-591) (Cu K_α radiation, $\lambda = 1.54178$ Å) and a Smart6000 CCD detector equipped with an Oxford Cryostream low temperature device.

The *Proteum II* software suite was used for data collection, cell refinement, reduction, and absorption correction. Single crystal X-ray data of PCN-66, PCN-68, and PCN-610 were collected on beamline 15ID-B at the Advanced Photon source in Argonne National Laboratory. Structures were solved by direct method and refined by full-matrix least-squares on F^2 using *SHELXTL*.[122] Non-hydrogen atoms were refined with anisotropic displacement parameters during the final cycles. Organic hydrogen atoms were placed in calculated positions with isotropic displacement parameters set to 1.2 × U_{eq} of the attached atom. The solvent molecules are highly disordered, and attempts to locate and refine the solvent peaks were unsuccessful. Contributions to scattering due to these solvent molecules were removed using the *SQUEEZE* routine of *PLATON*;[123] structures were then refined again using the data generated.

Crystal data for PCN-60: $C_{12}H_6O_5Zn$, M = 295.54, colorless block, 0.15 * 0.13 * 0.12 mm^3, cubic, space group *Fm*-3*m* (No. 225), a = 42.8434(3), V = 78641.5(10) Å^3, Z = 96, D_c = 0.599 g/cm^3, F_{000} = 14208, Bruker three circle diffractometer, CuK$_\alpha$ radiation, λ = 1.54178 Å, T = 173(2)K, $2\theta_{max}$ = 83.9º, 44736 reflections collected, 1381 unique (R_{int} = 0.0377). Final *GooF* = 1.115, *R1* = 0.0501, *wR2* = 0.1588, *R* indices based on 1325 reflections with I >2sigma(I) (refinement on F^2), 98 parameters, 9 restraints. μ = 1.086 mm^{-1}.

Crystal data for PCN-61: $C_{12}H_6CuO_5$, M = 293.71, blue block, 0.08 * 0.07 * 0.03 mm^3, cubic, space group *Fm*-3*m* (No. 225), a = 42.7958(6), V = 78379.7(19) Å^3, Z = 96, D_c = 0.597 g/cm^3, F_{000} = 14112, Bruker three circle diffractometer, CuK$_\alpha$ radiation, λ = 1.54178 Å, T = 173(2)K, $2\theta_{max}$ = 65.1º, 33881 reflections collected, 740 unique (R_{int} =

0.0560). Final *GooF* = 1.122, *R1* = 0.0423, *wR2* = 0.1176, *R* indices based on 702 reflections with I >2sigma(I) (refinement on F^2), 98 parameters, 9 restraints. μ = 0.989 mm^{-1}.

Crystal data for PCN-66: $C_{48}H_{27}Cu_3NO_{15}$, *M* = 1048.33, green prism, 0.08 * 0.06 * 0.05 mm^3, cubic, space group *Fm*-3*m* (No. 225), *a* = 49.112(4), *V* = 118458(18) $Å^3$, *Z* = 32, D_c = 0.470 g/cm^3, F_{000} = 16928, synchrotron radiation, λ = 0.44280 Å, *T* = 100(2)K, $2\theta_{max}$ = 25.7º, 118332 reflections collected, 2903 unique (R_{int} = 0.1743). Final *GooF* = 1.104, *R1* = 0.1204, *wR2* = 0.3423, *R* indices based on 1259 reflections with I >2sigma(I) (refinement on F^2), 127 parameters, 63 restraints. μ = 0.237 mm^{-1}.

Crystal data for PCN-68: $C_{60}H_{30}Cu_3O_{15}$, *M* = 1181.46, green prism, 0.03 * 0.02 * 0.02 mm^3, cubic, space group *Fm*-3*m* (No. 225), *a* = 59.153(6), *V* = 206977(39) $Å^3$, *Z* = 32, D_c = 0.303 g/cm^3, F_{000} = 19104, synchrotron radiation, λ = 0.41328 Å, *T* = 150(2)K, $2\theta_{max}$ = 15.8º, 189298 reflections collected, 1650 unique (R_{int} = 0.2187). Final *GooF* = 1.210, *R1* = 0.1227, *wR2* = 0.3300, *R* indices based on 1395 reflections with I >2sigma(I) (refinement on F^2), 137 parameters, 146 restraints. μ = 0.137 mm^{-1}.

Crystal data for PCN-610: $C_{54}H_{30}Cu_3O_{15}$, *M* = 1109.40, green prism, 0.03 * 0.02 * 0.02 mm^3, cubic, space group *Fm*-3*m* (No. 225), *a* = 52.738(5), *V* = 146679(24) $Å^3$, *Z* = 32, D_c = 0.402 g/cm^3, F_{000} = 17952, synchrotron radiation, λ = 0.41328 Å, *T* = 173(2)K, $2\theta_{max}$ = 23.9º, 389054 reflections collected, 3753 unique (R_{int} = 0.2923). Final *GooF* = 1.429, *R1* = 0.1556, *wR2* = 0.3923, *R* indices based on 2340 reflections with I >2sigma(I) (refinement on F^2), 146 parameters, 61 restraints. μ = 0.193 mm^{-1}.

Low-pressure gas sorption measurements. N_2 and H_2 sorption isotherms were measured up to 1 bar using a Micrometrics ASAP 2020 surface area and pore size analyzer. Pore size distribution data were calculated from the N_2 sorption isotherms based on DFT model in the Micromeritics ASAP2020 software package (assuming slit pore geometry). An as-isolated sample was immersed in methanol for 24 h, and the extract was decanted. Fresh methanol was subsequently added, and the crystals were allowed to stay for an additional 24 h to remove the nonvolatile solvates (DMF and water). The samples were collected by decanting and treated with dichloromethane similarly to remove methanol solvates. After the removal of dichloromethane by decanting, the sample was activated by drying under a dynamic vacuum at room temperature overnight. Before the measurement, the sample was dried again by using the "outgas" function of the surface area analyzer for 12 h at 100 °C. Oil-free vacuum pumps and oil-free pressure regulators were used for all measurements to prevent contamination of the samples during the degassing process and isotherm measurement.

High-pressure gas sorption measurements. High pressure excess adsorption of H_2, CH_4 and CO_2 of PCN-61, PCN-66 and PCN-68 were measured using an automated controlled Sieverts' apparatus (PCT-Pro 2000 from Setaram) at 77 K (liquid nitrogen bath) or 298 K (room temperature). About 600 mg of activated sample were loaded into sample holder under an argon atmosphere. Before measurements, sample was degassed at 100 °C overnight. The free volume was determined by the expansion of low-pressure He (<5 bar) at room temperature. The temperature gradient between gas reservoir and sample holder was corrected by applying a correction factor to the raw data, which was

obtained by replacing the sample with polished stainless-steel rod and measuring the adsorption isotherm at the same temperature over the requisite pressure regime. The total gas uptake was calculated by: $N_{total} = N_{excess} + \rho_{bulk} V_{pore}$, where ρ_{bulk} equals to the density of compressed gases at the measured temperature and V_{pore} was obtained from the N_2 isotherm at 77 K.

2.3 Results and Discussion

The solvothermal reactions between these ligands and copper salts yield four MOFs, PCN-61, PCN-66, PCN-68, and PCN-610, separately (PCN stands for Porous Coordination Network). As has been anticipated, these MOFs are isostructural (space group: *Fm-3m*), and the following crystal structure discussion will focus on PCN-61. The three isophthalate moieties in btei are linked through the copper paddlewheel SBUs to form the cuboctahedra building blocks, which are covalently linked through the 5 position of the isophthalate moieties to form a (3,24)-connected network (Figure 5). The 3D framework can be viewed as the packing of three polyhedra: cuboctahedron (CO), truncated tetrahedron (TT), and truncated octahedron (TO) (Figure 6). Each truncated triangle face of the TT and TO is fully occupied by one ligand. Every CO shares 8 triangular faces with 8 TT, and the remaining 6 square faces with 6 TO. The diameters of spheres representing the void inside these polyhedra are listed in Table 1. As expected, the ligand extension has enlarged the size of the TO, which is accompanied by a mild increase in the size of the TT and no change in the size of the CO. It is evident that the pore size of TO has reached the meso-range in PCN-66, PCN-68, and PCN-610. It is critical that in order to form the aforementioned (3-24)-connected net, the 6 carboxylate

groups in the ligand of C_3 symmetry must be coplanar although the horizontal mirror plane is not a prerequisite.

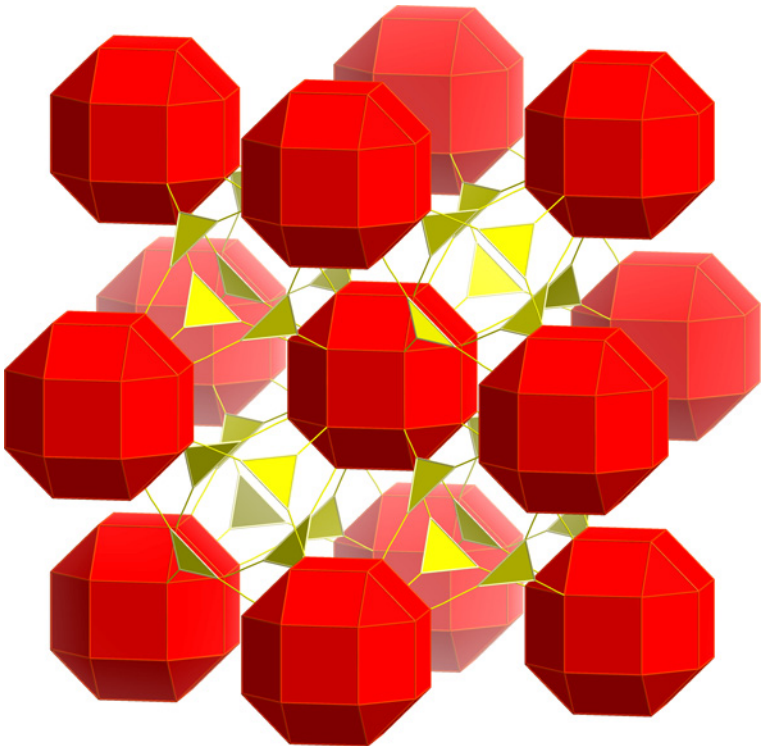

Figure 5. The (3,24)-connected network.

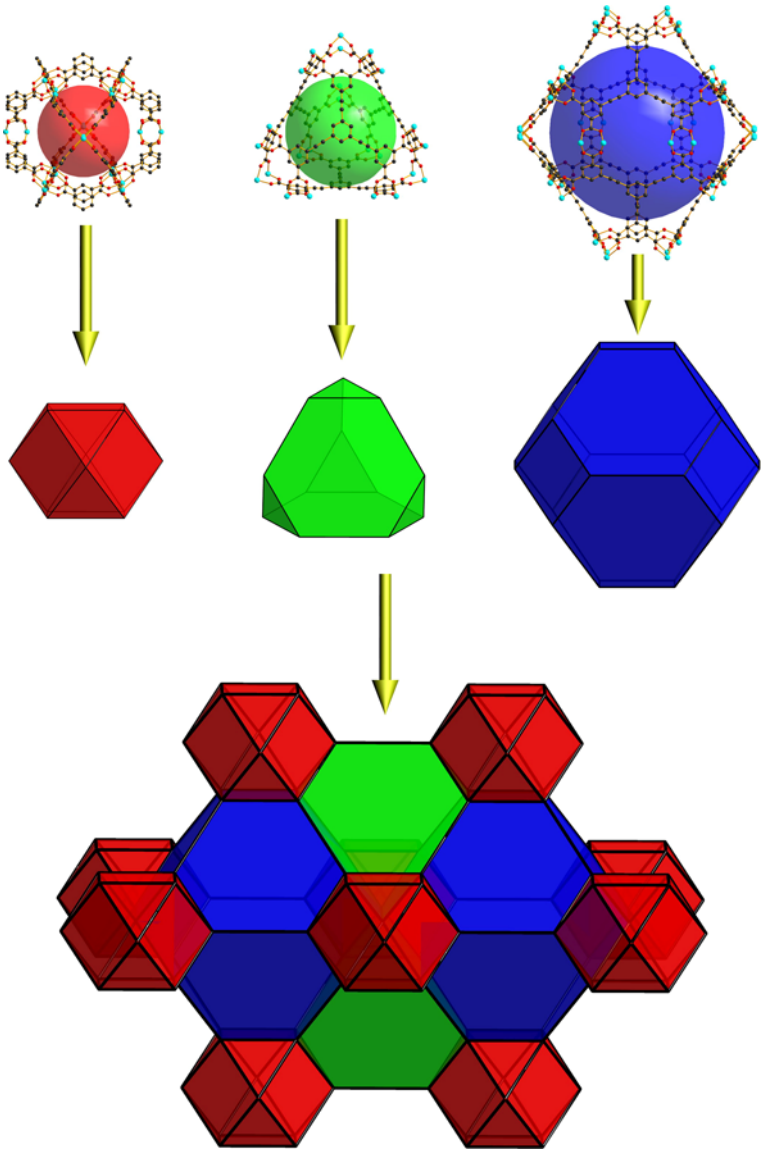

Figure 6. Polyhedra and their 3D packing in PCN-61.

Table 1. Unit cell parameter (*Fm*-3*m*), ligand size (L size), and polyhedron size of the isoreticular PCN-6X MOF series.

Materials	Unit cell / Å	L size / Å[a]	CO size / Å	TT size / Å	TO size / Å
PCN-61	42.796	6.906	12.0	11.8	18.8
PCN-66	49.112	9.758	12.0	12.0	20.6
PCN-68	52.738	11.243	12.0	14.8	23.2
PCN-610	59.153	13.815	12.0	18.6	26.0

[a] Ligand size is defined as the distance between the centre of the ligand and the centre of terminal benzene ring.

In PCN-61, PCN-66, and PCN-68, crystallinity retains after the removal of guest molecules, as indicated by the powder X-ray diffraction patterns (PXRD) (Figure 7). Such robustness is very rare in MOFs constructed with nanoscopic ligand, and confirms our hypothesis that the adoption of cuboctahedron as building units indeed limits the open window size and increases framework stability.

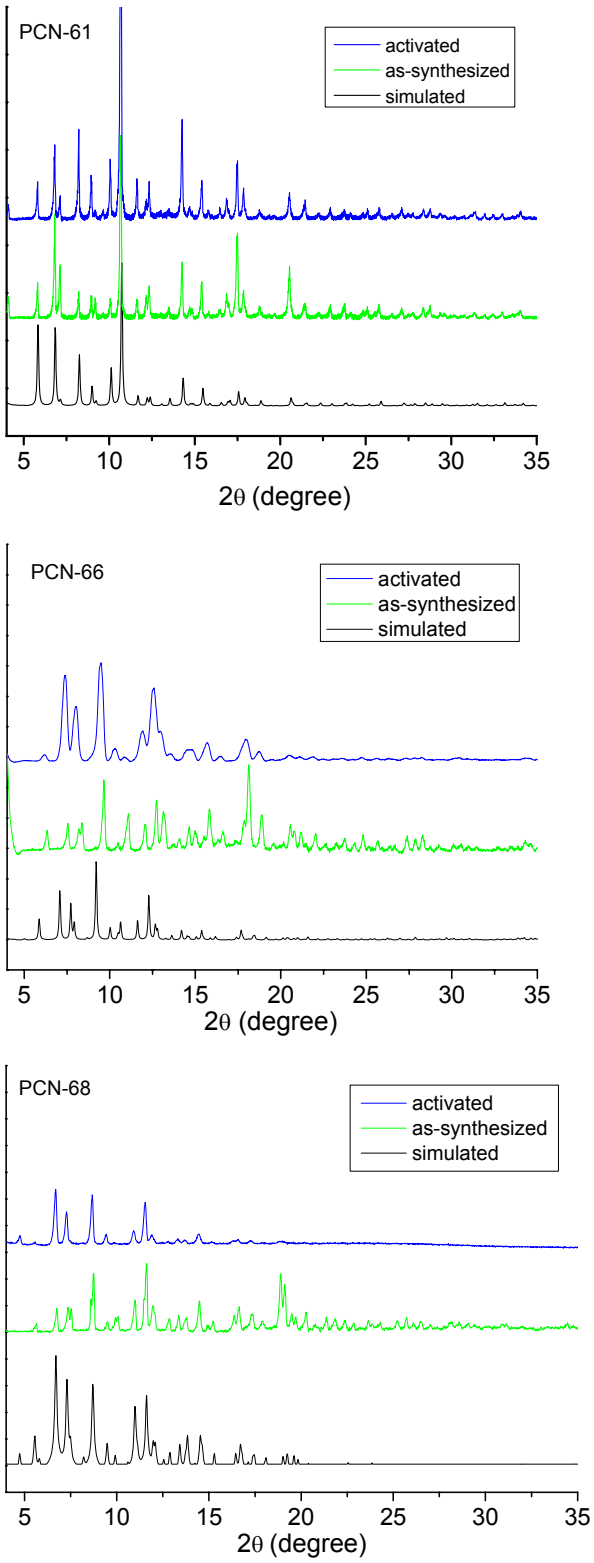

Figure 7. PXRD patterns of PCN-61, PCN-66, and PCN-68.

Lah and coworkers reported a similar (3,24)-connected MOF based on zinc paddlewheel SBU.[117] However, their MOF is not stable upon the removal of guest molecules, which is probably due to 1) the flexible ligand they used and 2) the unstable zinc paddlewheel SBU after activation. Compared to rigid ligand, thermal vibration and bond rotation in flexible ligand may lead to distortion of the topology and instability of the framework. On the other hand, the tetrahedral coordination geometry preference of Zn^{2+} may rationalize its instability after the removal of the axially coordinated solvent molecules during activation. PCN-60, the zinc paddlewheel counterpart of PCN-61, has been synthesized and fully characterized, and it also suffers from the instability after activation. As can be seen from the scanning electron microscopy (SEM) images (Figure 8), in PCN-61, the crystals remained the same ordered shape in both the as-synthesized and the activated one. In PCN-60, however, the crystals shrank upon the removal of guest molecules, which indicates the framework disintegration. The framework's instability was also confirmed by PXRD patterns (Figure 9). Thus, it is tempting to suggest that in order to get stable (3,24)-connected MOFs, rigid ligands and stable paddlewheel SBUs (such as dicopper) should be used.

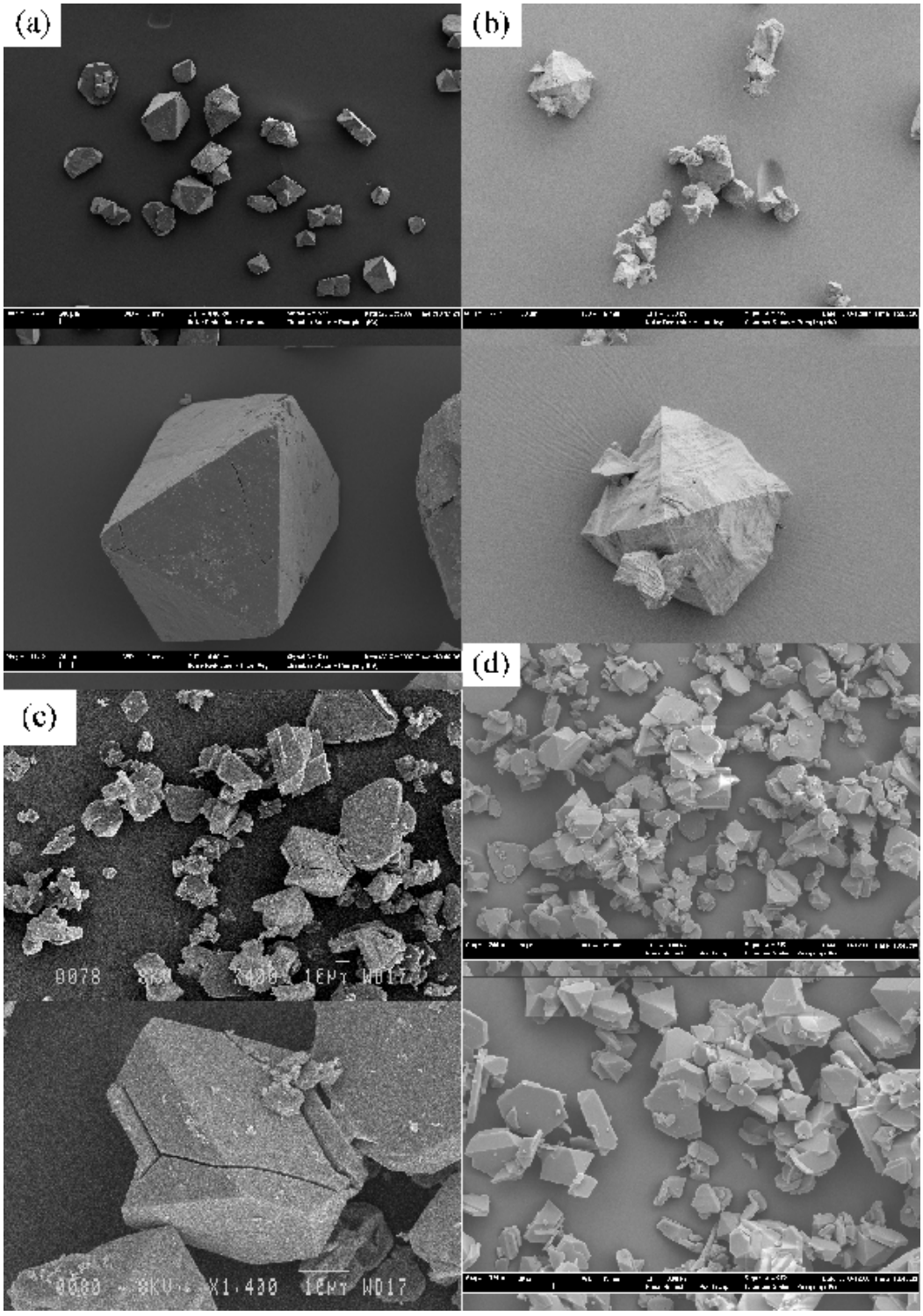

Figure 8. SEM images of PCN-60 and PCN-61 (a: as-synthesized PCN-60; b: activated PCN-60; c: as-synthesized PCN-61; d: activated PCN-61).

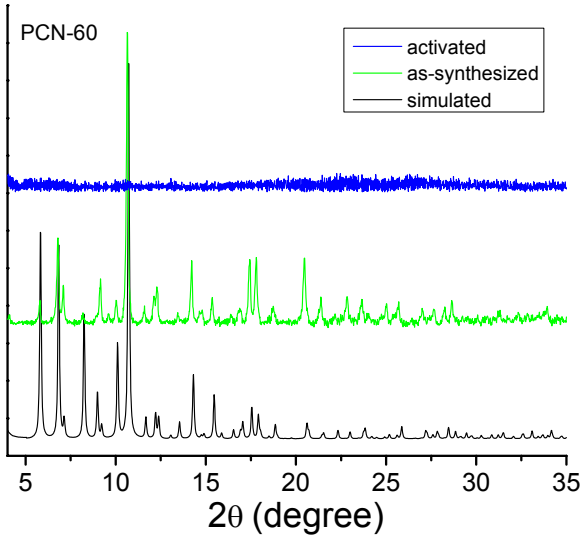

Figure 9. PXRD pattern of PCN-60.

In the foregoing discussion of the crystal structure, it has been indicated that the sizes of the cavities within these MOFs range from microporous (CO & TT) to mesoporous (TO). This hierarchic porous structure is reflected in the N_2 sorption isotherms collected at 77 K (Figure 10). The hybrid porous structures exhibit reversible pseudo-type-I isotherms with a small step before the plateau appears, and this is typical in other (3,24)-connected MOFs and MOFs with both micro- and mesopores.[115-116,124-129] We believe it is due to the multi-layer sorption happening in larger cavities after the formation of a single layer at low pressure. The pore size data calculated based on nitrogen sorption isotherms are consistent with the crystal data as well (Figure 11).

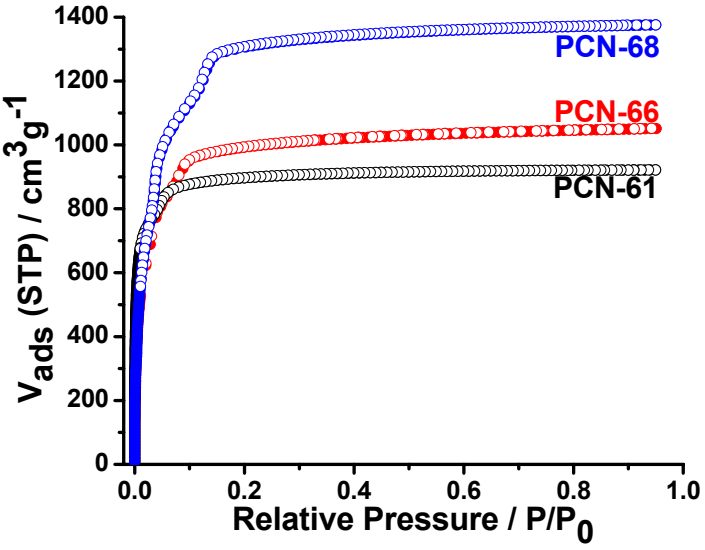

Figure 10. N_2 sorption isotherms of PCN-61, PCN-66, and PCN-68 at 77 K.

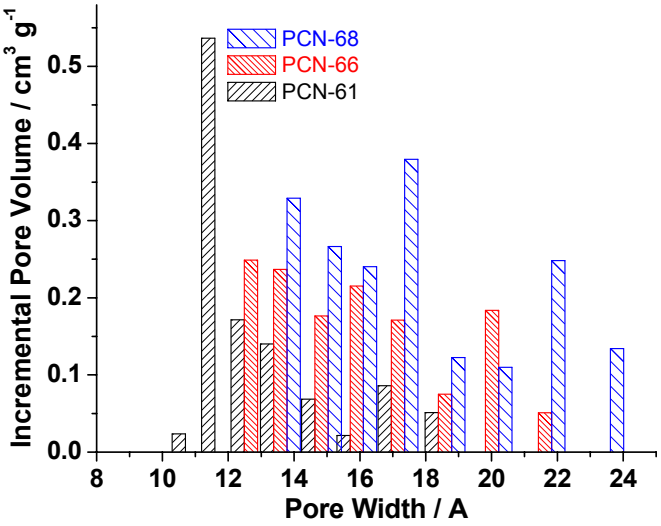

Figure 11. Pore size distribution of PCN-61, PCN-66, and PCN-68.

Albeit been questioned by its validity in microporous materials, BET model is still widely used to estimate the surface area of MOFs.[130] Two criteria discussed in the literature have been strictly followed to decide the pressure range for applying the BET analysis.[104] By using BET model, activated PCN-61 has a specific surface area of 3000 $m^2 g^{-1}$. Assuming monolayer coverage, the Langmuir surface area is 3500 $m^2 g^{-1}$. In PCN-66, where a longer ligand is used, there is a dramatic increase in surface area (BET surface area: 4000 $m^2 g^{-1}$; Langmuir surface area: 4600 $m^2 g^{-1}$). In PCN-68, where an even longer ligand is used, the BET surface area can reach as high as 5109 $m^2 g^{-1}$, with a Langmuir surface area of 6033 $m^2 g^{-1}$. To the best of our knowledge, PCN-68 possesses the highest surface area reported to date for MOFs based on paddlewheel clusters, and it is also among the highest reported (Table 2).[103,125,131] The above data confirm our initial thought that elongating ligand will give rise to increased surface area. For PCN-610, in which the longest ligand was used, there is barely any nitrogen sorption observed, implying a complete collapse of the framework. The same conclusion is also drawn from the powder X-ray diffraction (PXRD) data, which reveals that PCN-610 lost its crystallinity completely upon activation (Figure 12).

Table 2. Surface areas, pore volumes, and porosities of isoreticular PCN-6X MOFs

Materials	Surface Area ($m^2 g^{-1}$) (Langmuir/BET/cal.[a])	Pore Volume ($cm^3 g^{-1}$) (exp./cal.[a])	Porosity[a]
PCN-61	3500/3000/3455	1.36/1.37	77.0%
PCN-66	4600/4000/3746	1.63/1.75	80.0%
PCN-68	6033/5109/3871	2.13/2.17	82.9%
PCN-610	NA/NA/4160	NA/3.00	86.8%

[a] Calculated using Material Studio 4.4.

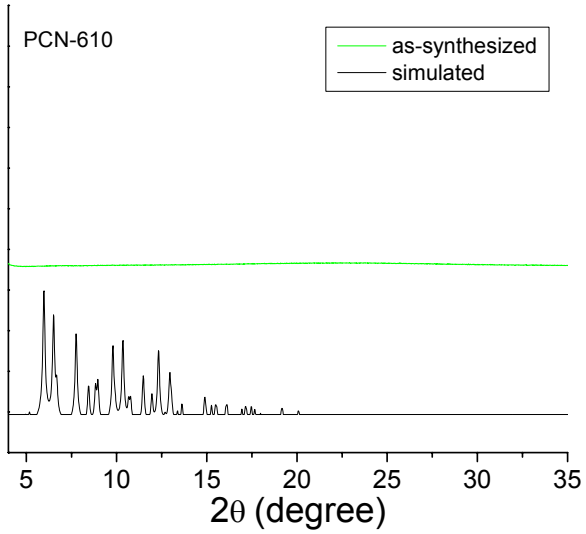

Figure 12. PXRD pattern of PCN-610.

From the foregoing discussion, it is evident that by using the dendritic hexa-carboxylate ligands, isoreticular MOFs with higher surface area can be obtained by ligand extension. However, this approach, which is based on the formation of cuboctahedra and (3,24)-connected framework, has its limitations. The ligand size that may lead to a stable MOF with the highest surface areas in this series falls between ptei (11.2 Å) in PCN-68 and ttei (13.8 Å) in PCN-610. In addition, the (3,24)-connected network can incorporate ligands as large as 11.2 Å without framework decomposition, whereas in the twisted boracite network, which is composed of tri-carboxylate ligands (less dendritic) and dimetal paddlewheels,[106-107,132-133] even a ligand as small as 4.179 Å (tatb) would lead to the disintegration of the PCN-6′ framework.[107] It is our belief that dendritic ligands with more branches will lead to stable MOFs that can tolerate more extended ligands leading to even higher surface areas.[134]

The high surface areas of the isoreticular PCN-6X series of PCN-61, PCN-66, and PCN-68 prompted us to study their gas uptake capacity, especially that of hydrogen, methane, and carbon dioxide.[93] Hydrogen is an ideal energy carrier. However, the lack of an effective storage method hinders its application. The U.S. Department of Energy (DOE) has recently reset the gravimetric and volumetric storage targets for on-board hydrogen storage for the year 2010 (4.5 wt %, 28 g L^{-1}) and 2015 (5.5 wt%, 40 g L^{-1}). Due to its fast kinetics and favorable thermodynamics in hydrogen adsorption and release, MOF-based hydrogen storage has attracted remarkable attention recently.[26-27,131,135-136] The low pressure hydrogen uptake capacities of PCN-6X series are shown in Figure 13. At a low pressure region (< 1 bar), the hydrogen uptake capacity is mainly

controlled by the hydrogen affinity towards the framework, which can be quantified by the isosteric heat of adsorption (Figure 14). PCN-61, which has the smallest pore size, also has the highest heat of adsorption and highest capacity (2.25 wt % at 77 K, 1 bar). PCN-66 and PCN-68 have heats of adsorption and adsorption capacities similar to each other (1.79 wt % in PCN-66 *vs.* 1.87 wt % in PCN-68). This trend is consistent with the nature of physisorption, in which narrower pores would have stronger interactions with the guest gas molecules due to the increased interaction between the guests and the opposite potential walls within small pores.[38]

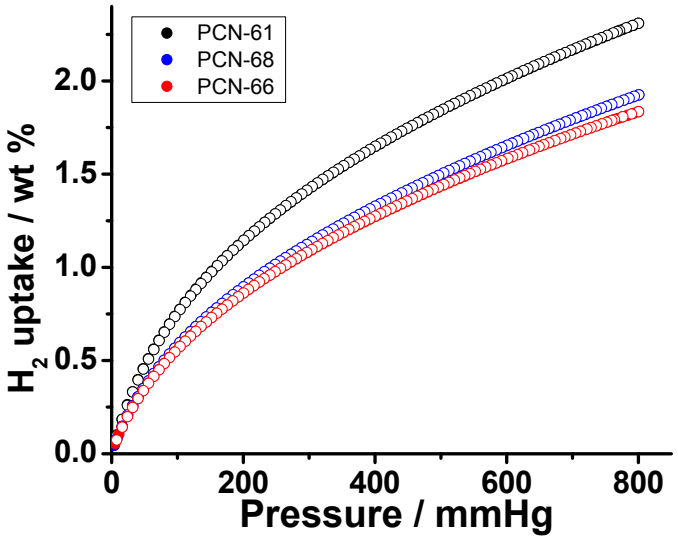

Figure 13. Low pressure H_2 uptake in PCN-61, PCN-66, and PCN-68.

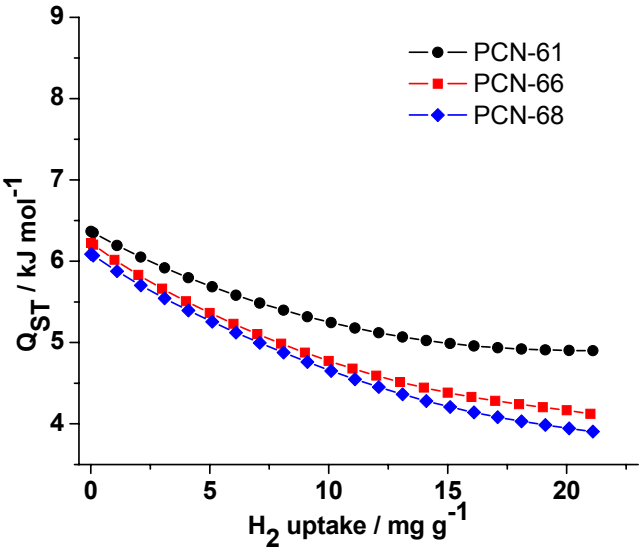

Figure 14. H_2 isosteric heat of adsorption in PCN-6X series.

Unlike the low pressure hydrogen sorption capacity, which is dominated by the hydrogen affinity, the maximum excess hydrogen uptake capacity in MOFs, which typically can only be reached at high pressure range, is controlled mainly by the surface area and pore volume.[27,72] This is consistent with what has been observed in the PCN-6X series. As can be seen from Figure 15, PCN-68, which has the highest surface area, also has the highest maximum excess hydrogen uptake capacity (73.2 mg g^{-1}, Table 3). Taking into consideration the gaseous hydrogen compressed within the framework void, its total hydrogen uptake capacity would reach 130 mg g^{-1} (100 bar) (Figure 16), which makes it one of the best adsorbents with the highest gravimetric hydrogen uptake capacity.[93] It is worth noting that the maximum adsorption pressure increases from PCN-61 (33 bar) to PCN-66 (45 bar) and PCN-68 (50 bar), indicating higher pressure is needed to reach maximum adsorption in sorbents with higher pore volumes.

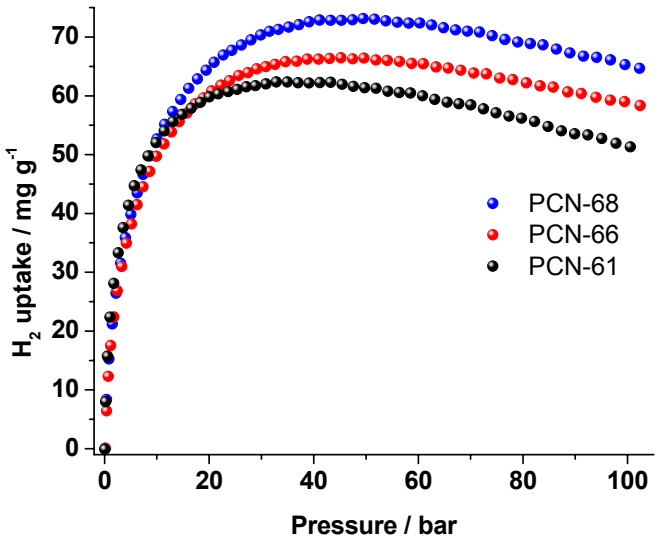

Figure 15. Excess gravimetric H_2 uptake in PCN-61, PCN-66, and PCN-68 at 77 K.

Table 3. Hydrogen uptake capacities and isosteric heats of adsorption in PCN-6X series.

Materials	H_2 uptake at 77K, 1 atm / wt% (g L^{-1})	Maximum excess H_2 uptake / mg g^{-1} (g L^{-1})	Q_{ST} / kJ mol^{-1}
PCN-61	2.25 (12.6)	62.4 (35.0) 33 bar 77K 6.67 (3.74) 90 bar 298K	6.36
PCN-66	1.79 (7.98)	66.5 (29.6) 45 bar 77K 7.85 (3.50) 90 bar 298K	6.22
PCN-68	1.87 (7.20)	73.2 (28.0) 50 bar 77K 10.1 (4.10) 90 bar 298K	6.09

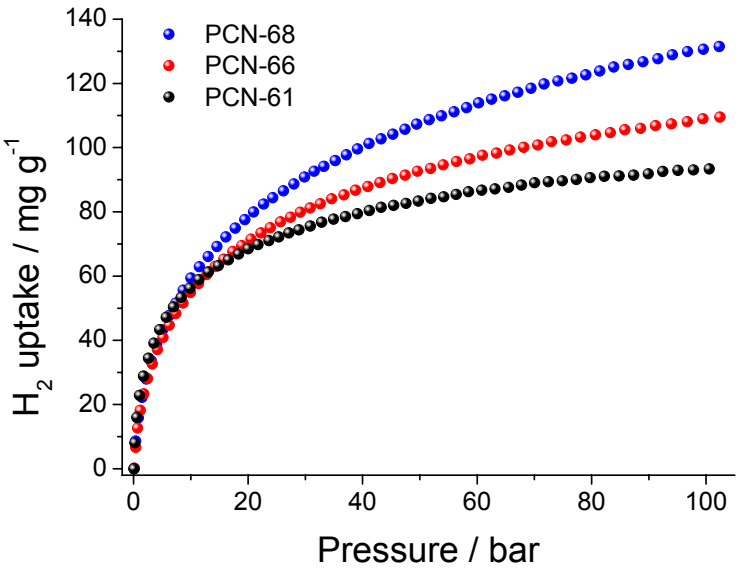

Figure 16. Total gravimetric H_2 uptake in PCN-61, PCN-66, and PCN-68 at 77 K.

Using the crystal density data, the volumetric hydrogen uptake capacities were also calculated (Figure 17). Unlike the trend in gravimetric capacity, where the material with the highest surface area has the highest capacity, the volumetric capacity follows the opposite trend, which is dominated by the densities of the sorbents. The gravimetric capacity has been emphasized in the past hydrogen storage research, and rightfully so. However, the volumetric capacity is particularly relevant in volume-limited fuel-cell applications.[137] Both of these criteria should be emphasized equally in the search for ideal hydrogen storage materials.

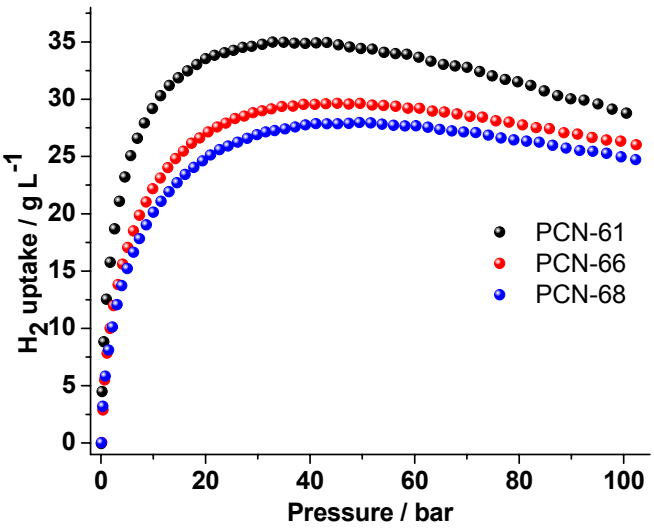

Figure 17. Excess volumetric H_2 uptake in PCN-61, PCN-66, and PCN-68 at 77 K.

Natural gas (methane being the main component) is another alternative on-board fuel that has aroused much interest. Like hydrogen, however, it also lacks an effective storage method. The DOE target for on-board methane storage is based on volumetric capacity (180 v(STP)/v(STP) under 35 bar and near ambient temperature), which requires the adsorbents to have not only high porosity, but also high packing density and good thermal conductivity.[89] PCN-6X series MOFs have been tested for their methane uptake capacities at 298 K. As can be seen from Figure 18, the gravimetric methane uptake capacities in these MOFs are also proportional to their surface areas. At medium pressure range (<20 bar), PCN-61 has the highest capacity, possibly due to the stronger methane affinity of the framework, which can be ascribed to the small pore size. When the pressure goes to high range (>60 bar), the effect of surface area and pore volume starts to dominate, making PCN-68 the one with the highest uptake. By assuming the

crystal density as the packing density, the volumetric methane uptake capacities were also calculated (Figure 19). PCN-61 has the highest capacity at 35 bar (145 v/v), followed by PCN-66 (110 v/v) and PCN-68 (99 v/v) (Table 4). This trend can be ascribed to the crystal density difference among the three (0.56 g cm^{-3} in PCN-61 *vs.* 0.45 g cm^{-3} in PCN-66 and 0.38 g cm^{-3} in PCN-68). From this study, it can be concluded that high surface area should not be the sole emphasis if the aim is to achieve high volumetric methane uptake capacity. Instead, a balance should be maintained among porosity, density, pore size, and other factors.

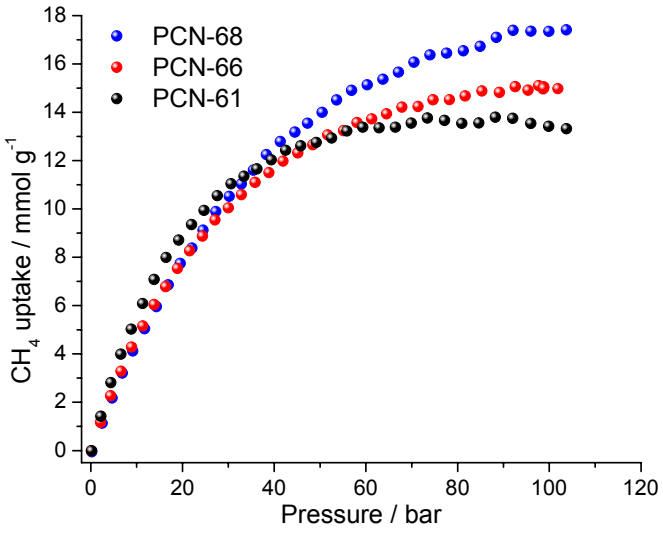

Figure 18. Excess gravimetric capacities of CH_4 adsorption in PCN-61, PCN-66, and PCN-68 at 298 K.

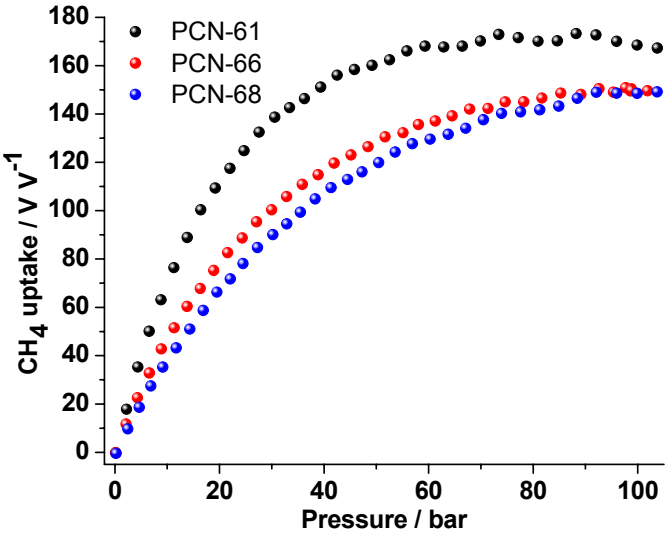

Figure 19. Excess volumetric capacities of CH_4 adsorption in PCN-61, PCN-66, and PCN-68 at 298 K

Table 4. CH_4 and CO_2 excess uptake capacities in PCN-6X series at 35 bar and 298 K.

Materials	CH_4 / mmol g^{-1}	CH_4 / V V^{-1}	CO_2 / mmol g^{-1}
PCN-61	11.6	145	23.5
PCN-66	11.1	110	26.3
PCN-68	11.6	99	30.4

The aggravated global warming, which is partially attributed to the increasing carbon dioxide concentration in the air, has aroused worldwide concerns. Carbon capture and sequestration (CCS), a process involving the capture of carbon dioxide from the air and sequestering it underground, has been proposed as a feasible way to control the atmospheric carbon dioxide concentration.[92] Using porous materials to capture carbon dioxide based on the sorption mechanism will be an energy-conserving alternative approach. The study of MOF-based carbon dioxide capture is growing dramatically.[93] The 298 K high pressure gravimetric carbon dioxide adsorption capacities of PCN-6X series are shown in Figure 20. Once again, their storage capacities still follow the trend similar to those found in the aforementioned hydrogen and methane adsorption studies. PCN-68 has the highest gravimetric carbon dioxide storage capacity among the three, and is also among the highest reported (Table 4). Based on the amount of gas adsorbed and the pore volume of the frameworks, the density of the carbon dioxide captured can be calculated (Figure 21). The density of adsorbed carbon dioxide is the highest in PCN-61. Based on the total capacity, at 35 bar and room temperature, a container filled with PCN-61 can store 8.2 times the amount of CO_2 in an empty container, and this volumetric capacity is 7.3 for PCN-66 and 7.4 for PCN-68, which make PCN-6X series compound good adsorbents for carbon dioxide capture.

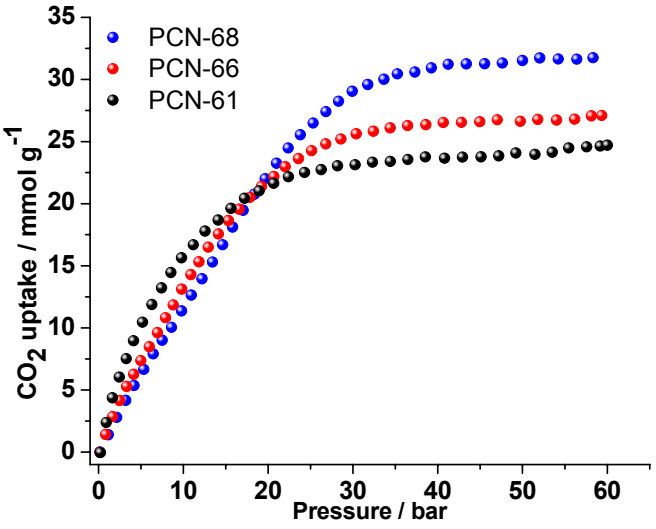

Figure 20. Excess gravimetric CO_2 uptake in PCN-61, PCN-66, and PCN-68 at 298 K.

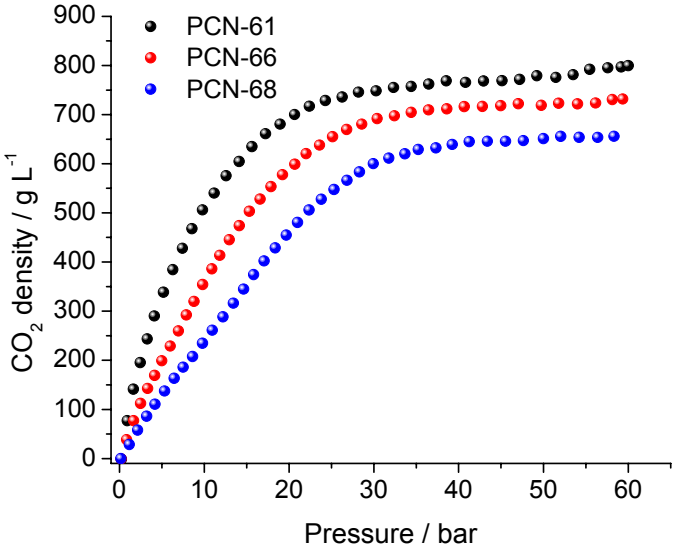

Figure 21. Excess CO_2 density in PCN-61, PCN-66, and PCN-68 at 298 K.

2.4 Conclusions

In summary, an isoreticular MOF series with the (3,24)-connected network topology has been synthesized by using a series of dendritic hexa-carboxylate ligands. The framework is stabilized by incorporating microwindows, whose size is fixed by the formation of cuboctahedra supported by the isophthalate moieties throughout the framework. The mesocavities, which are connected by the microwindows, however, are sustained by these nanoscopic ligands and responsible for the porosity improvement with ligand extension. In addition, the formation of isophthalate-sustained cuboctahedra in the (3,24)-connected network prohibits framework interpenetration, leading to MOFs with close to record-high surface areas. Hydrogen, methane, and carbon dioxide adsorption studies of MOFs in this series have also revealed close to record-high gas adsorption capacities. However, this approach has its limitations. The ligand size that may lead to a stable MOF with the highest surface areas in this isoreticular series falls between 11.2 and 13.8 Å. We propose that dendritic ligands with even more branches should lead to stable MOFs that can tolerate more extended ligands leading to even higher surface areas. It is interesting to see whether MOFs based on other polyhedra as building blocks will also demonstrate the same high stability, permanent porosity and high surface area.

3. A NBO-TYPE METAL-ORGANIC FRAMEWORK DERIVED FROM A POLYYNE-COUPLED DI-ISOPHTHALATE LINKER FORMED IN SITU[†]

3.1 Introduction

Metal-organic frameworks (MOFs) have emerged as a new type of porous materials.[3-5,138-139] Their large surface area, high pore volume, uniform yet controllable pore size, and pore geometry make them good adsorbents for gases, such as H_2, CH_4, and CO_2.[26-27,90,93-95,135,140-143] Their gravimetric gas adsorption capacity, especially at high pressure range, is directly related to the specific surface area and pore volume.[27,72] The NbO-type MOFs, which consist of 4-connected di-isophthalate ligands and 4-connected secondary building units (SBU) (typically dicopper paddlewheel), have shown excellent framework stability, porosity, and gas adsorption capacity.[73,90,142,144-149] On the other hand, their hydrogen adsorption capacity at room temperature is relatively low because of weak framework-hydrogen interactions.

[†]Reproduced with permission from "A NbO-Type Metal-Organic Framework Derived from a Polyyne-Coupled Di-Isophthalate Linker Formed in Situ" by Zhao, D.; Yuan, D. Q.; Yakovenko, A.; Zhou, H. C., 2010. *Chem. Commun.*, 46, 4196-4198, Copyright 2010 by Royal Society of Chemistry.

In our group's continuing exploration of MOFs as a hydrogen storage medium, aligned open metal sites have been shown to have an impact on the heat of hydrogen adsorption.[118] In addition, double bonds[142] and aromatic rings[150] were also studied as possible hydrogen-framework interacting sites. However, prior to this work, carbon-carbon triple bonds, especially polyyne chains, have not been systematically studied for gas adsorption purposes in MOFs. In this section, we report an NbO-type MOF that is constructed based on a polyyne-coupled di-isophthalate ligand formed *in situ*. The ensuing MOF has permanent porosity after the removal of guest molecules, and exhibits excellent H_2, CH_4 and CO_2 adsorption capacity.

3.2 Experimental Section

Materials and methods. Commercially available reagents were used as received without further purification. Nuclear magnetic resonance (NMR) data were collected on a Mercury 300 MHz NMR spectrometer. Fourier transform infrared spectroscopy (FTIR) data were collected on a SHIMADZU IRAffinity-1 FTIR Spectrophotometer. Elemental analyses (C, H, and N) were obtained from Canadian Microanalytical Service, Ltd. Thermogravimetry analyses (TGA) were performed under N_2 on a SHIMADZU TGA-50 TGA, with a heating rate of 5 °C min^{-1}.

Synthesis of 5-ethynylisophthalic acid, H_2ei. Diethyl-5-(trimethylsilylethynyl)isophthalate[119] (6.363 g, 20 mmol) was suspended in 150 mL of THF/methanol (1/1) mixed solvent, to which 100 mL of 1 M KOH aqueous solution was added. The mixture was stirred at room temperature for 3 hours. Organic solvent was removed under vacuum, and diluted hydrochloric acid was added to the remaining

aqueous solution until it became acidic (pH = 2). The precipitate was collected by filtration, washed with water, and dried under vacuum at 80 °C to give H_2ei as a white solid. ν_{max}(neat)/cm^{-1} 3545, 3076, 1712, 1450, 1205 and 916; δ_H(300 MHz; DMSO-d_6; Me_4Si) 13.27 (2 H, br), 8.42 (1 H, t, *J* 3), 8.12 (2 H, d, *J* 3) and 4.37 (1 H, s); δ_C(300 MHz; DMSO-d_6; Me_4Si) 165.80, 135.93, 132.01, 130.09, 122.71, 82.63 and 81.60; *m/z* (ESI) 188.9861 (M^-, 34%), 224.9597 (27), 378.9674 (100) and 535.0992 (7).

Synthesis of PCN-46. H_2ei (50 mg, 2.63×10^{-4} mol) and cupric acetate (125 mg, 6.26×10^{-4} mol) were dissolved in 20 mL of dimethylacetamide (DMA) in a vial, to which 10 drops of HBF_4 were added. The vial was tightly capped and placed in a 85 °C oven for 72 h to yield 102 mg of green block crystals (yield: 77% based on H_2ei). ν_{max}(neat)/cm^{-1} 3414, 2933, 1620, 1371 and 1014. The crystal has a formula of $[Cu(H_2O)]_2$(bdi)·5DMA·$2H_2O$, which was derived from crystallography data, elemental analysis (% calc/found: C 47.61/47.41, H 5.89/5.98, N 6.94/7.25), and TGA.

X-ray crystallography. Single crystal X-ray structure determination of PCN-46 was performed at 173(2) K on the Advanced Photon Source on beamline 15ID-B in Argonne National Laboratory. Raw data for the structure were processed using SAINT and absorption corrections were applied using SADABS.[151] Structures were solved by direct method and refined by full-matrix least-squares on F^2 using *SHELXTL*.[122] Non-hydrogen atoms were refined with anisotropic displacement parameters during the final cycles. Organic hydrogen atoms were placed in calculated positions with isotropic displacement parameters set to 1.2 × U_{eq} of the attached atom. The solvent molecules are highly disordered, and attempts to locate and refine the solvent peaks were unsuccessful.

Contributions to scattering due to these solvent molecules were removed using the *SQUEEZE* routine of *PLATON*;[123] structures were then refined again using the data generated.

Crystal data for PCN-46: $C_{10}H_5CuO_5$, M = 268.68, trigonal, space group R-3m, a = b = 18.2386(8), c = 42.049(2) Å, V = 12113.4(9) Å^3, Z = 18, D_c = 0.663 g cm^{-3}, F_{000} = 2412, synchrotron radiation, λ = 0.41328 Å, T = 173(2)K, $2\theta_{max}$ = 30.0º, 68838 reflections collected, 3022 unique (R_{int} = 0.1069). Final *GooF* = 1.055, *R1* = 0.0747, *wR2* = 0.2042, 82 parameters. CCDC-747535.

Sample activation. As-synthesized PCN-46 crystals were immersed in methanol for 3 days to remove the nonvolatile solvates (DMA and water), and the extract was decanted every day and fresh methanol was replaced. The sample was collected by decanting and treated with dichloromethane for 3 days similarly to remove methanol. After the removal of dichloromethane by decanting, the sample was activated by drying under a dynamic vacuum at room temperature overnight.

Powder X-ray diffraction. Powder X-ray diffraction (PXRD) pattern of as-synthesized PCN-46 was obtained on a Bruker-AXS D8 Advanced Bragg-Brentano X-ray Powder Diffractometer using Cu-K_α radiation. Due to the instability of activated PCN-46 in the air, its PXRD pattern was obtained by sealing the sample in 0.6 mm standard Lindeman capillary under an argon atmosphere and collecting the data on a Bruker GADDS three-circle X-ray Diffractometer (Cu-K_α radiation).

Low-pressure gas sorption measurements. The low-pressure gas sorption isotherm measurements were performed at 77 K (liquid nitrogen bath) or 87 K (liquid

argon bath) on a Micromeritics ASAP 2020 surface area and pore size analyzer. Before measurements, the activated sample was degassed for 10 h at 100 °C. UHP grade (99.999%) N_2, He, H_2, and Ar were used for all measurements. Oil-free vacuum pumps and oil-free pressure regulators were used for all measurements to prevent contamination of the samples during the degassing process and isotherm measurement.

High-pressure gas sorption measurements. High pressure excess adsorption of H_2, CH_4 and CO_2 were measured using an automated controlled Sieverts' apparatus (PCT-Pro 2000 from Setaram) at 77 K (liquid nitrogen bath) or 298 K (room temperature). About 600 mg of activated sample were loaded into sample holder under an argon atmosphere. Before measurements, the sample was degassed at 100 °C overnight. The free volume was determined by the expansion of low-pressure He (<5 bar) at room temperature. The temperature gradient between the gas reservoir and sample holder was corrected by applying a correction factor to the raw data, which was obtained by replacing the sample with a polished stainless-steel rod and measuring the adsorption isotherm at the same temperature over the requisite pressure regime. The total gas uptake was calculated by: $N_{total} = N_{excess} + \rho_{bulk} V_{pore}$, where ρ_{bulk} equals to the density of compressed gases at the measured temperature and pressure, and V_{pore} was obtained from the N_2 sorption isotherm at 77 K.

3.3 Results and Discussion

The *in-situ* ligand reactions under solvothermal conditions are well documented in the literature.[152-153] Herein our goal is to apply this versatile method to simplify the MOF synthesis by combining the ligand preparation, purification, and MOF synthesis

into one simple step. It is hoped that the formation of the MOF will drive the ligand formation to completion; therefore, the purification of the ligand becomes unnecessary.

Copper(I)-catalyzed oxidative coupling of terminal acetylenes was found as early as 1869 and has been developed into a versatile synthetic tool for 1,3-diyne compounds.[154] We reason that by combining isophthalate ligand bearing terminal acetylene with a slight excess of copper(II) salt, which can be readily reduced to copper(I) under solvothermal reaction conditions, a homocoupling product di-isophthalate can be generated. Subsequently, the di-isophthalate linker reacts with the Cu (II) salts giving rise to a NbO MOF.

The ligand precursor used herein is 5-ethynylisophthalic acid (H_2ei), which contains both isophthalic moieties and terminal acetylene suitable for the coupling reaction. As expected, every two of the H_2ei were coupled into one 5,5'-(buta-1,3-diyne-1,4-diyl)diisophthalic acid (H_4bdi) under the catalysis of Cu(I), which came from the reduction of cupric acetate. In addition, the *in-situ* formed 4-connected ligand bdi^{4-} was linked via the 4-connected dicopper paddlewheel SBU to form a NbO-type MOF, PCN-46 (PCN stands for porous coordination network) (Figure 22) in 77% of yield (based on H_2ei).

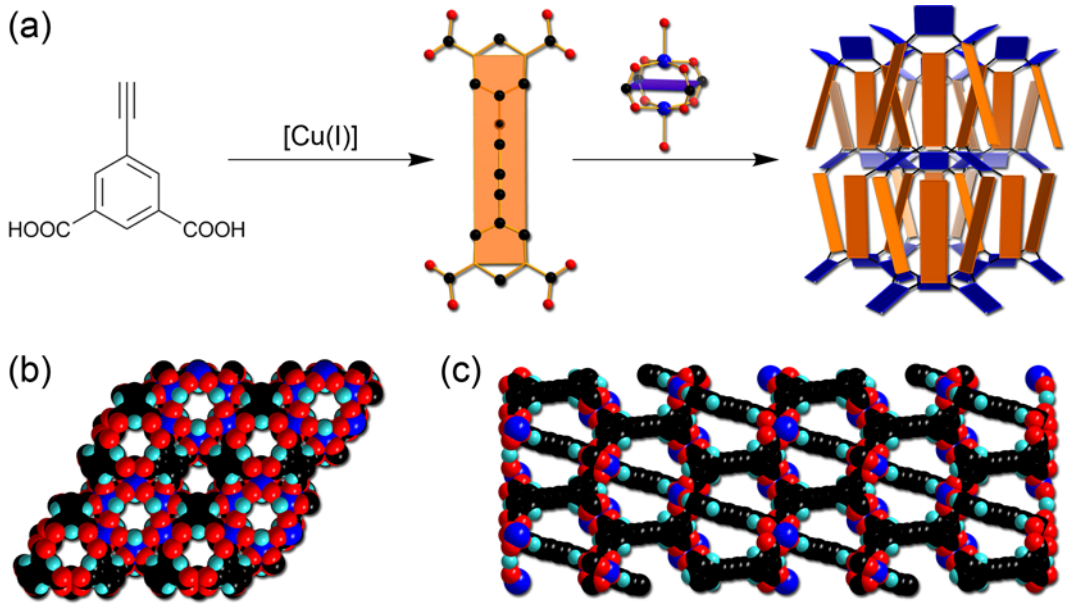

Figure 22. (a) *In-situ* formed ligand bdi^{4-} and the formation of NbO-type framework; (b) atomic packing of PCN-46, viewed through [0 0 1] direction; (c) atomic packing of PCN-46, viewed through [1 0 0] direction.

It must be pointed out that the exact chronological sequence of events such as the coupling of the precursor molecules, the deprotonation of the di-isophthalic acid, and the formation of the MOF has not been deciphered. However, the high overall yield of the procedure implies that the coupling reaction benefits from the consumption of the tetracarboxylic acid by MOF formation.

Calculated using the PLATON routine, PCN-46 has a solvent accessible volume of 73.8%. This high porosity prompts us to examine its gas adsorption property. The phase purity of the bulk sample was confirmed by powder X-ray diffraction (PXRD), and the framework retains its crystallinity after the removal of guest molecules (Figure 23). Its permanent porosity was confirmed by both N_2 (77 K) (Figure 24) and Ar (77 and

87 K) (Figure 25) sorption isotherms. The isotherms show type-I sorption behaviour, which is typical for microporous materials. Based on the N_2 sorption isotherm, PCN-46 has a BET surface area of 2500 $m^2 g^{-1}$ (Langmuir surface area: 2800 $m^2 g^{-1}$) and a total pore volume of 1.012 $cm^3 g^{-1}$. It has a uniform pore size around 6.8 Å based on the Horvath-Kawazoe model in the Micromeritics ASAP2020 software package (assuming cylinder pore geometry).[155]

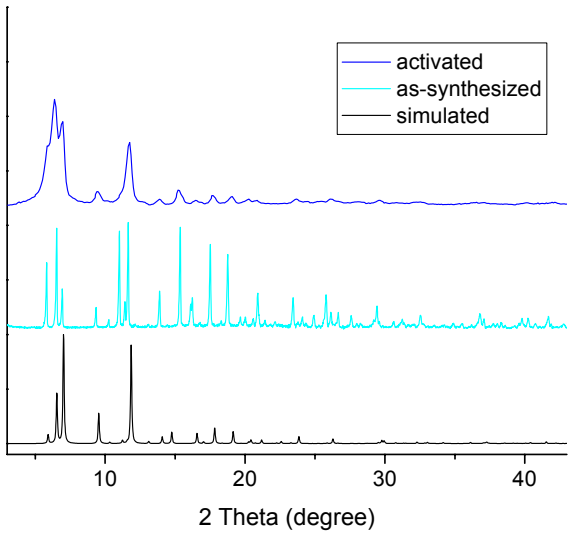

Figure 23. PXRD patterns of PCN-46.

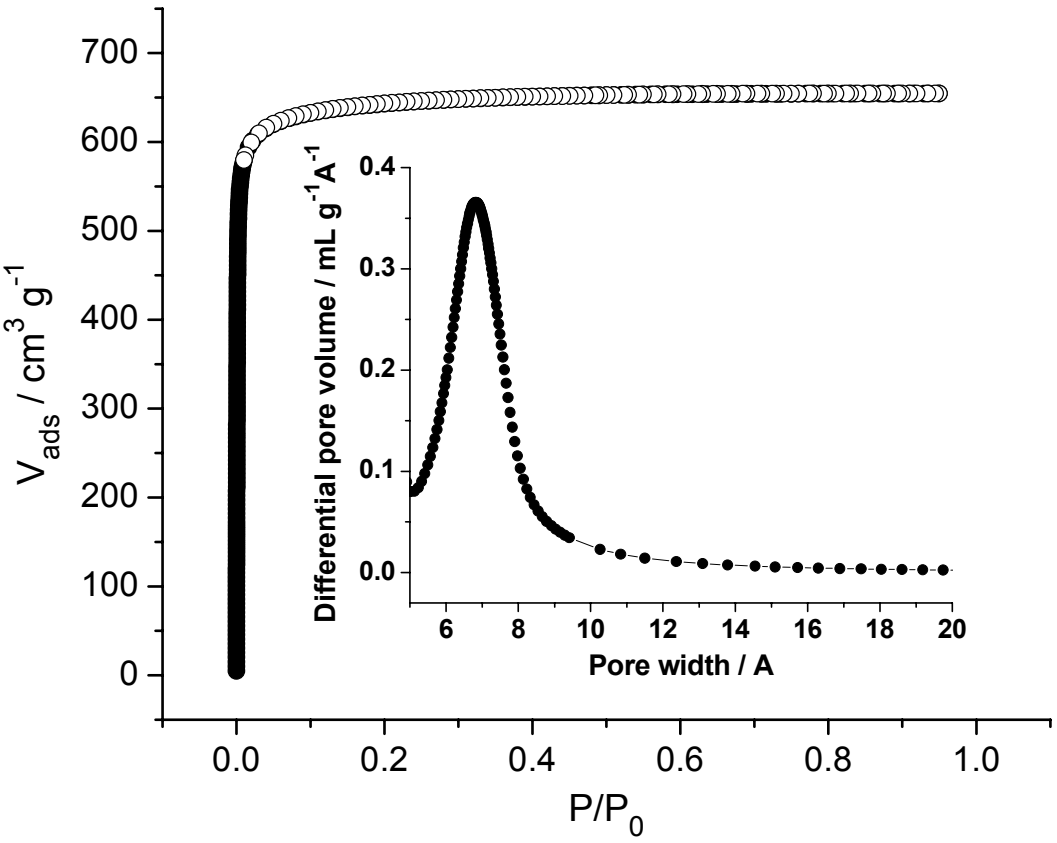

Figure 24. The N_2 sorption isotherm at 77 K (solid symbols, adsorption; open symbols, desorption) and pore size distribution of PCN-46.

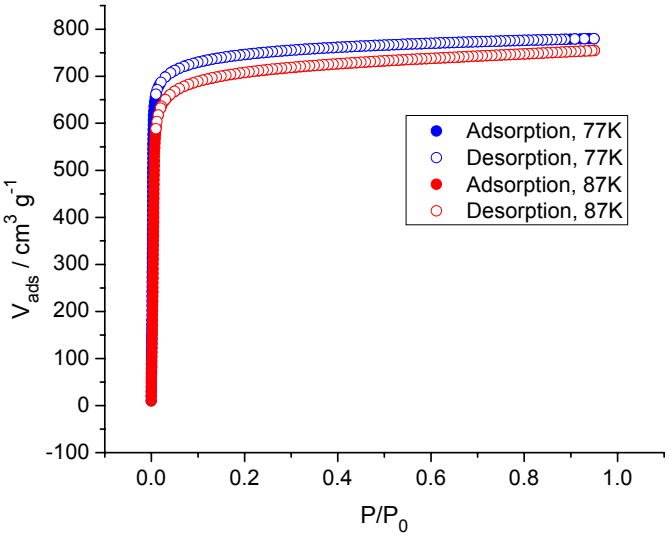

Figure 25. The Ar sorption isotherms of PCN-46 (solid symbols: adsorption; open symbols: desorption; 77 K isotherms: blue; 87 K isotherms: red).

The high porosity and stable framework make PCN-46 a good candidate for gas storage. In 2009, the U.S. Department of Energy (DOE) reset the gravimetric and volumetric storage targets for on-board hydrogen storage for years 2010 (4.5 wt %, 28 g L^{-1}) and 2015 (5.5 wt %, 40 g L^{-1}). At 77 K and 760 Torr, PCN-46 can reversibly adsorb 1.95 wt % of H_2 (Figure 26). Under high pressure range, the saturated excess gravimetric H_2 uptake is 5.31 wt % (56.1 mg g^{-1}) at 32 bar. Taking the gaseous H_2 compressed within the void pore at 77 K into consideration, the total gravimetric H_2 uptake can reach as high as 6.88 wt % (73.9 mg g^{-1}) at 97 bar. Calculated from the crystal density of the activated form (0.6185 g cm^{-3}), PCN-46 has an excess volumetric H_2 uptake of 34.7 g L^{-1} (32 bar) and a total volumetric uptake of 45.7 g L^{-1} (97 bar).

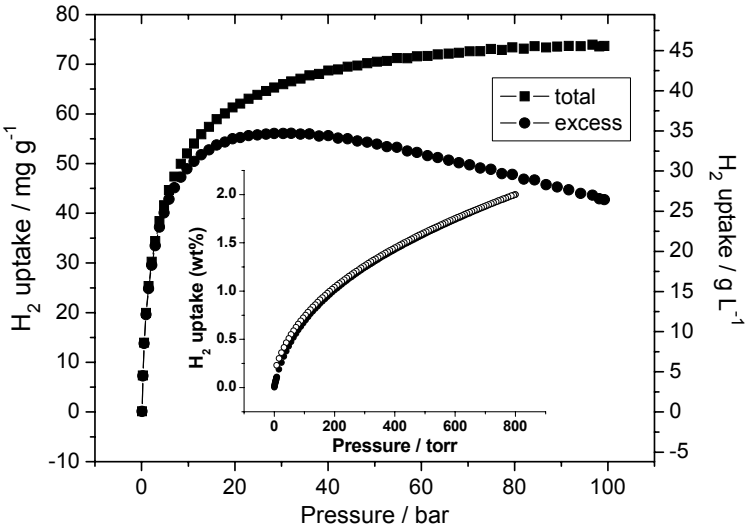

Figure 26. Gravimetric and volumetric H_2 uptake in PCN-46 at 77 K (solid symbols, adsorption; open symbols, desorption).

Theoretical studies reveal that given the same MOF structural type, the longer the ligand, the higher the specific surface area, and accordingly the higher the gravimetric H_2 uptake would be.[104-105] This is further confirmed by the comparison of PCN-46 and the NOTT series NbO-type MOFs.[144] As can be seen from Table 5, when the length of ligands increases, the surface area, pore volume, and high pressure hydrogen uptake of the MOFs also increase, but not the heat of adsorption.

Table 5. Ligands, porosity and H_2 uptake of selected NbO-type MOFs.

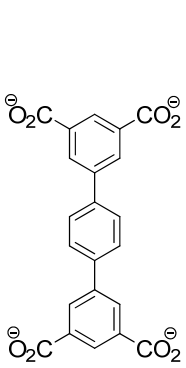

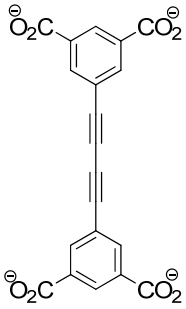

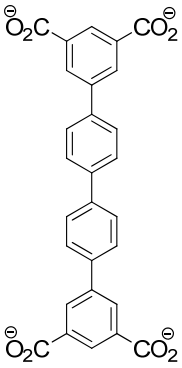

MOFs	Ligand length (Å)[a]	BET surface area (m^2 g^{-1})	Pore volume (cm^3 g^{-1})[b]	H_2 uptake (mg/g)[c] 60bar	Q_{st} at low coverage (kJ mol^{-1})
NOTT-101	5.773	2316	0.886	66.0	<5.5
PCN-46	6.484	2500	1.012	71.6	7.20
NOTT-102	10.098	2942	1.138	72.0	<5.5

[a] Distance between 5-position of two isophthalate moieties. [b] Calculated from N_2 isotherms at 77 K. [c] Total uptake at 77 K.

Based on a variant of the Clausium-Clapeyron equation, the H_2 isosteric adsorption enthalpy of PCN-46 reaches 7.20 kJ mol^{-1} at low coverage, and decreased to 4.06 kJ mol^{-1} at medium coverage (Figure 27).[31] The increased heat of hydrogen adsorption in PCN-46, compared to those of other NbO type MOFs shown in Table 5, can be attributed to the interaction between dihydrogen molecules and the exposed and delocalized π electrons in the polyyne unit in bdi^{4-}, which is evidently stronger than that for the phenyl rings in $tpta^{4-}$ and $qpta^{4-}$. A strong interaction between acetylene and a NbO-type MOF containing alkyne unit was also discovered, in which the high acetylene affinity towards the framework was partially attributed to the π-π interaction.[148] In addition, the replacement of phenyl rings by polyyne chain leads to a boost of pore volume and hydrogen uptake. As Table 5 shows, the bdi^{4-} ligand is much shorter than $qpta^{4-}$, but the pore volumes and hydrogen uptakes of PCN-46 and NOTT-102 are very close. Furthermore, in the absence of a catalyst, the hydrogen addition reaction on the polyyne unit has not been observed even at high pressure as shown by the reversible hydrogen sorption isotherms of PCN-46, validating the stability of the MOF under hydrogen storage conditions.

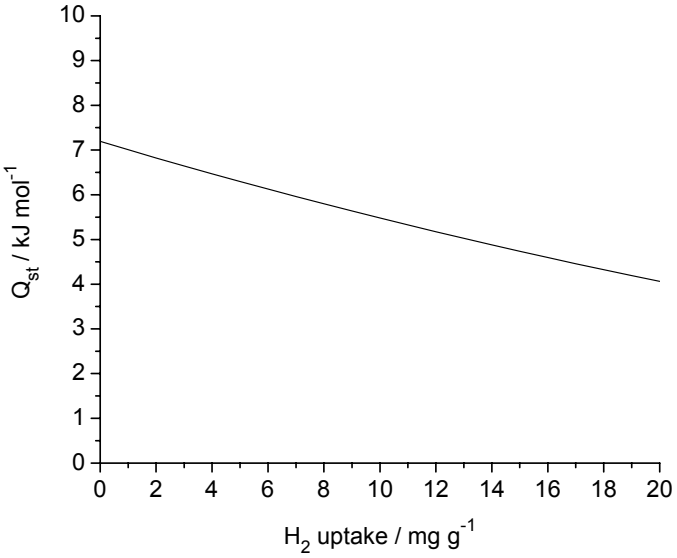

Figure 27. H_2 isosteric adsorption enthalpy of PCN-46.

Methane is another candidate as an on-board fuel. However, it also suffers from a lack of reliable storage. The DOE methane storage target has a volumetric basis: 180 v(STP) v^{-1} at 35 bar.[156] With high surface area and high pore volume, MOFs have been proved reliable due to their high methane uptake capacity.[90,141-142] The high pressure methane adsorption in PCN-46 at 298 K was also examined. As can be seen from Figure 28, the gravimetric excess CH_4 uptake in PCN-46 reaches saturation at 12 mmol g^{-1} (60 bar) (total: 17.2 mmol g^{-1}, 110 bar). At 35 bar, the volumetric excess CH_4 uptake in PCN-46 is 150 v v^{-1} (total: 172 v v^{-1}). Compare with another NbO-type MOF PCN-14, which has a record high CH_4 uptake capacity (230 v v^{-1} at 35 bar), the relatively lower capacity in PCN-46 may come from the fewer gas adsorption sites and lower material density (0.6185 g cm^{-3} in PCN-46 *vs.* 0.871 g cm^{-3} in PCN-14).

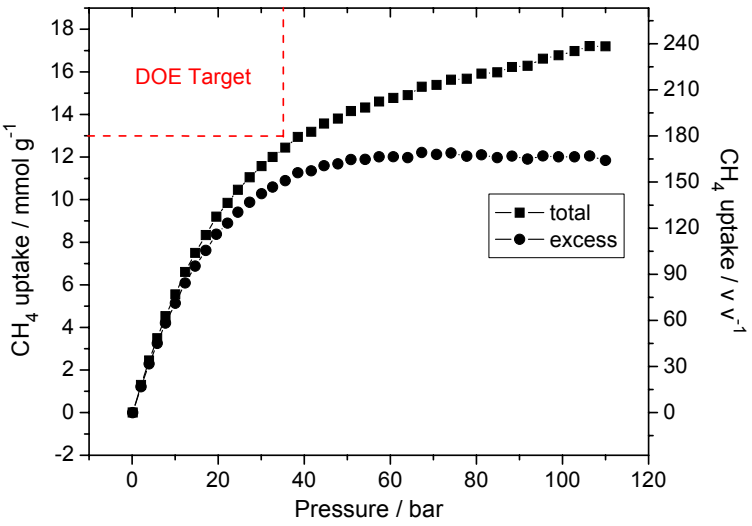

Figure 28. Gravimetric and volumetric CH_4 uptake in PCN-46 at 298 K.

The capture and sequestration of CO_2 is considered to be an effective way for the control of greenhouse gas emissions. Most of the capture processes in large scale operation nowadays are based on amine-based wet scrubbing systems, which have high energy and resource consumption.[157] MOFs have been proven to be good adsorbents for CO_2 at ambient temperature.[94-95] As can be seen in Figure 29, the saturation excess CO_2 uptake in PCN-46 is 21.0 mmol g^{-1} (30 bar). Although this value is lower than MOF-177 and NH_4F-treated MIL-101(Cr) (33.5 and 40 mmol g^{-1}, respectively), the density of CO_2 adsorbed within PCN-46 could reach that of liquid CO_2 at much lower pressure. This indicates that the CO_2 stored within MOFs are highly compressed and MOFs-based CO_2 sequestration is an efficient and energy-reserving approach.

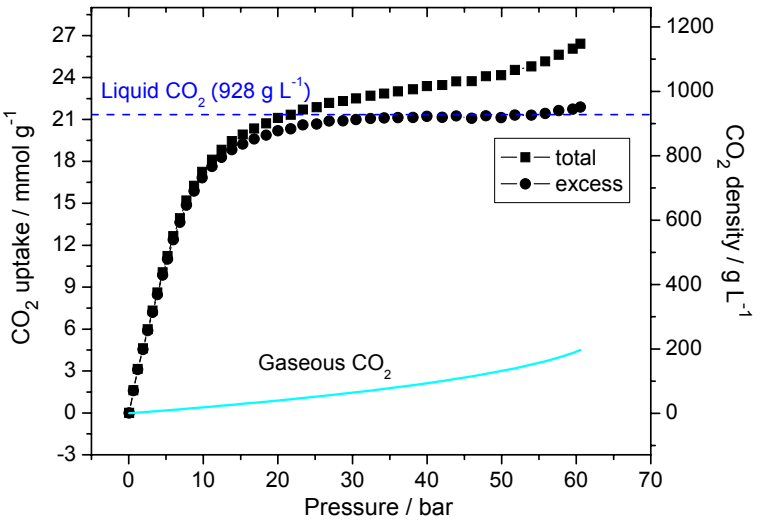

Figure 29. Gravimetric CO_2 uptake and density in PCN-46 at 298 K. Solid line, density of compressed CO_2 at 298 K; dashed line, density of liquid CO_2 at 273 K (928 g L^{-1})[158].

3.4 Conclusions

In summary, a NbO-type MOF, PCN-46, was synthesized based on an *in-situ* formed polyyne-coupled di-isophthalate ligand by the copper(I)-catalyzed oxidative coupling of terminal acetylenes. The polyyne units in the MOF exhibit high heat of hydrogen adsorption, high pore volume, and excellent stability under high pressure hydrogen. The hydrogen, methane, and carbon dioxide adsorption uptakes of the MOF are also impressive.

4. THERMOSENSITIVE GATE OPENING AND SELECTIVE GAS ADSORPTION IN A METAL-ORGANIC POLYHEDRON[†]

4.1 Introduction

Adsorption-based gas separation plays an important role in industry.[159] By judiciously choosing adsorbents with appropriate surface property and pore size, gas separation can be achieved in an energy-conserving and environmentally friendly approach. Three mechanisms have been proposed for this process: steric, kinetic, and equilibrium effect.[159] The steric separation, in which only small adsorbates can diffuse into the adsorbents, is widely encountered in zeolites and molecular sieves due to their uniform aperture size in the crystalline structure.[159] During this process, a size match between the adsorbent' aperture and the adsorbate is required. However, such optimized aperture size is not always readily available when the size difference between the adsorbates being separated is small. In this case, a molecule sieve with adjustable mesh size is required.[160] Our group has reported the mesh-adjustable molecular sieves (MAMSs), which are based on metal-organic frameworks (MOFs) and have tunable mesh size directly proportional to temperature.[161-163] It is proposed that the escalating thermal vibration of the bulky groups in the amphiphilic ligands at higher temperature accounts for such thermosensitive gate opening.

[†]Reproduced with permission from "Thermosensitive Gating Effect and Selective Gas Adsorption in a Porous Coordination Nanocage" by Zhao, D.; Yuan, D. Q.; Krishna, R.; van Baten, J. M.; Zhou, H. C., 2010. *Chem. Commun.*, Advance Article, DOI:10.1039/C0CC02771E, Copyright 2010 by Royal Society of Chemistry.

Metal-organic polyhedra (MOP) are newly emerging porous materials and have found applications as plasticizer, gas sponge, ion channel, coatings, and building units.[11-16] Their porosity comes from the inner void of these discrete nanocages, although it is possible that the spacing between these nanocages contributes to their porosity as well.[13,18-20] We hypothesize that by covering the nanocage with bulky group outside, the opening towards the inner void can be reduced. As a result, these bulky groups may function as gates and give the nanocage thermosensitive gate opening property as well.

4.2 Experimental Section

Materials and methods. Commercially available reagents were used as received without further purification. Nuclear magnetic resonance (NMR) data were collected on a Mercury 300 MHz NMR spectrometer. Fourier transform infrared spectroscopy (FTIR) data were collected on a SHIMADZU IRAffinity-1 FTIR Spectrophotometer. Thermogravimetry analyses (TGA) were performed under N_2 on a SHIMADZU TGA-50 Thermogravimetric Analyzer, with a heating rate of 5 °C min^{-1}. Elemental analyses (C, H, and N) were obtained from Canadian Microanalytical Service, Ltd. Powder X-ray diffraction (PXRD) patterns were obtained on a BRUKER D8-Focus Bragg-Brentano X-ray Powder Diffractometer equipped with a Cu sealed tube (λ = 1.54178) at a scan rate of 0.2 s deg^{-1}, solid-state detector, and a routine power of 1400 W (40 kV, 35 mA).

Synthesis of diethyl 5-((triisopropylsilyl)ethynyl)isophthalate, 1. Diethyl 5-iodoisophthalate[119] (6.67 g, 19.16 mmol), $Pd(PPh_3)_4$ (555 mg, 0.48 mmol) and CuI (37 mg, 0.19 mmol) were mixed in a 500 mL three neck Schlenk flask. The flask was pumped under vacuum and refilled with N_2 for three times, and then 200 mL of freshly

distilled and degassed triethylamine was added. The mixture was cooled to 0 °C in an ice water bath and ethynyltriisopropylsilane (5.24 g, 28.73 mmol) dissolved in 50 mL of THF was added via syringe dropwise. The mixture was stirred at room temperature for 1 hour, and then heated to reflux under nitrogen atmosphere overnight. After removal of organic solvent, the residue was dissolved in chloroform (150 mL) and washed with water (100 mL). The aqueous layer was back-extracted with chloroform (3 × 50 mL), and the combined organic layers were dried over $MgSO_4$ and filtered. The solvent was removed and the crude product was purified by column chromatography on silica gel with dichloromethane to give compound **1** as red oil (7.27 g, yield: 94 %). δ_H(300 MHz; $CDCl_3$; Me_4Si) 8.59 (1 H, t, *J* 3), 8.26 (2 H, d, *J* 3), 4.41 (4 H, q, *J* 6), 1.41 (6 H, t, *J* 6), 1.14 (18 H, m) and 1.08 (3 H, m); δ_C(300 MHz; $CDCl_3$; Me_4Si) 165.17, 136.75, 131.06, 130.00, 124.36, 104.73, 93.06, 61.55, 18.61, 14.29 and 11.21; *m/z* (ESI) 121.071 (92 %), 263.113 (91 %), 293.131 (100 %) and 403.259 ($[M+H^+]$, 43 %).

Synthesis of 5-((triisopropylsilyl)ethynyl)isophthalic acid, H_2tei. Compound 1 (7.649 g, 19 mmol) was suspended in 150 mL of THF/methanol (1/1) mixed solvent, to which 100 mL of 1 M NaOH aqueous solution was added. The mixture was stirred at room temperature for 1 hour. Organic solvent was removed under vacuum, and diluted hydrochloric acid was added to the remaining aqueous solution until it became acidic (pH = 2). The precipitate was collected by filtration, washed with water and dried under vacuum at 80 °C to give H_2tei as white solid (5.261 g, yield: 84 %). ν_{max}(neat)/cm^{-1} 2941, 2864, 2152, 1693, 1442, 1249, 952, 918, 881, 746 and 667; δ_H(300 MHz; DMSO-d_6; Me_4Si) 8.43 (1 H, d, *J* 3), 8.10 (2 H, t, *J* 3), 1.11 (18 H, m) and 1.10 (3 H, m); δ_C(300

MHz; DMSO-d_6; Me_4Si) 165.70, 135.66, 132.04, 129.93, 123.13, 104.92, 92.13, 18.39 and 10.59; *m/z* (ESI) 345.127 (M^-, 100 %) and 691.276 (37 %).

Synthesis of Cu(tei). H_2tei (100 mg, 0.289 mmol) was dissolved in 200 mL of benzene/methanol (19/1) mixed solvent, to which 2,6-lutidine (62 mg, 0.579 mmol) dissolved in 5 mL of methanol was added. The solution was sonicated for 10 min to insure complete deprotonation. $Cu(NO_3)_2 \cdot 2.5H_2O$ (67 mg, 0.288 mmol) dissolved in 5 mL of methanol was added into the previous solution. The solution turned into homogeneous deep blue. After precipitating and washing with methanol three times and drying under vacuum overnight, the final product was isolated as deep blue powder, which is readily soluble in several organic solvents, such as ether, benzene, chloroform, etc. Recrystallization from chloroform/DMF afforded single crystal suitable for X-ray crystallography study. The product has a formula of $[Cu(tei)(CH_3OH)(H_2O)]_{24}$, which is derived from crystallographic data, elemental analysis (% calc/found: C 52.44/52.47, H 6.60/6.46), and TGA. ν_{max}(neat)/cm^{-1} 2943, 2864, 2154, 1635, 1585, 1421, 1375, 881, 810, 771, 734 and 671.

X-ray crystallography. Single crystal X-ray structure determination of Cu(tei) was performed at 173(2) K on the Advanced Photon Source on beamline 15ID-B in Argonne National Laboratory. Raw data for the structure were processed using APEX-II and absorption corrections were applied using SADABS.[151] Structures were solved by direct method and refined by full-matrix least-squares on F^2 using *SHELXTL*.[122] Non-hydrogen atoms were refined with anisotropic displacement parameters during the final cycles. Organic hydrogen atoms were placed in calculated positions with isotropic

displacement parameters set to 1.2 × U_{eq} of the attached atom. The solvent molecules are highly disordered, and attempts to locate and refine the solvent peaks were unsuccessful. Contributions to scattering due to these solvent molecules were removed using the *SQUEEZE* routine of *PLATON*;[123] structures were then refined again using the data generated. Due to the small crystal size, the diffraction remained weak even under synchrotron radiation, and it is not possible to obtain a significantly better crystallographic model using methods currently available. Although the data in hand are poor, we still believe they support our interpretation.

Crystal data for Cu(tei): $C_{76}H_{104}Cu_4O_{20}Si_4$, M = 1704.11, trigonal, space group *R*-3*m* $a = b$ = 51.642(5), c = 33.245(4) Å, V = 76783(14) Å^3, Z = 18, D_c = 0.663 g/cm^3, F_{000} = 16056, synchrotron radiation, λ = 0.42318 Å, T = 173(2)K, $2\theta_{max}$ = 24.6º, 381539 reflections collected, 9447 unique (R_{int} = 0.3749). Final *GooF* = 3.422, *R1* = 0.4492, *wR2* = 0.7748. CCDC-779616.

Low-pressure gas sorption measurements. The low-pressure gas sorption isotherm measurements were performed on a Micromeritics ASAP 2020 surface area and pore size analyzer. Before measurements, the sample was degassed at 120 °C overnight to remove the coordinated ligands. UHP grade N_2, He, H_2, Ar, O_2, CH_4 and CO_2 were used for all measurements. Oil-free vacuum pumps and oil-free pressure regulators were used for all measurements to prevent contamination of the samples during the degassing process and isotherm measurement. The temperatures at 77 K, 87 K, 113 K, 142 K, 179 K, 195 K, and 273 K were maintained with a liquid nitrogen bath,

liquid argon bath, *iso*-pentane-liquid nitrogen bath, pentane-liquid nitrogen bath, hexane-liquid nitrogen bath, acetone-dry ice bath, and ice water bath, respectively.[164]

High-pressure gas adsorption and kinetics measurements. High pressure excess adsorption of H_2, CH_4 and CO_2 and H_2 sorption kinetics were measured using an automated controlled Sieverts' apparatus (PCT-Pro 2000 from Setaram) at 77 K (liquid nitrogen bath), 87 K (liquid argon bath) or 298 K (room temperature). About 1.7 g of activated sample was loaded into sample holder under an argon atmosphere. Before measurements, sample was degassed at 120 °C overnight. The free volume was determined by the expansion of low-pressure He (<5 bar) at room temperature. The temperature gradient between gas reservoir and sample holder was corrected by applying to the raw data a correction factor, which was obtained by replacing the sample with polished stainless-steel rod and measuring the adsorption isotherm at the same temperature over the requisite pressure regime. The sorption kinetics data were obtained via monitoring the pressure change in the sample holder once being connected to the gas reservoir. 80 bar of H_2 was used in the reservoir for adsorption kinetics study, and 70 bar of H_2 was used in the sample holder for desorption kinetics study.

Force fields, simulation methodology, and structural information. The Cu(tei) structure was considered to be rigid in the simulations. For the atoms in the host, the generic UFF[165] and DREIDING[166] force fields were used. The adsorption isotherms for CH_4 and Ar were computed using Monte Carlo (MC) simulations in the grand canonical (GC) ensemble. CH_4 molecules are described with a united atom model, in which each molecule is treated as a single interaction centre.[167] The parameters for CH_4 are taken

from Dubbeldam *et al*.[168] The force field for Ar corresponds to that given by Skoulidas and Sholl.[169] Additionally, Molecular Dynamics simulations were also carried out to determine the self-diffusivity of CH_4 within Cu(tei) for a variety of loadings. The Lorentz-Berthelot mixing rules were applied for calculating σ and ε/k_B for guest-host interactions. The Lennard-Jones potentials are shifted and cut at 12 Å. The number of unit cells in the simulation box was chosen such that the minimum length in each of the coordinate directions was larger than 24 Å, 2 unit cells in each direction. Periodic boundary conditions were employed. Further GCMC simulation details are available in earlier publications.[168,170-171] The GCMC simulations were performed using the BIGMAC code developed by T.J.H. Vlugt as basis.

CO_2/CH_4 selectivity prediction *via* IAST. The experimental isotherm data for pure CO_2 and CH_4 obtained using PCT-Pro 2000 for the high-pressure range (measured at 298 K) were fitted using a dual-Langmuir-Freundlich model:

$$q_i = q_{i,A,sat}\frac{b_{i,A}p_i^{v_{i,A}}}{1+b_{i,A}p_i^{v_{i,A}}} + q_{i,B,sat}\frac{b_{i,B}p_i^{v_{i,B}}}{1+b_{i,B}p_i^{v_{i,B}}} \qquad \text{Equation 2}$$

The adsorption selectivities, S_{ads}, for binary mixtures of $CO_2(1)/CH_4(2)$, defined by

$$S_{ads} = \frac{q_1/q_2}{p_1/p_2} \qquad \text{Equation 3}$$

were calculated using the Ideal Adsorption Solution Theory (IAST) of Myers and Prausnitz.[172] The calculations for binary mixtures with equal partial pressures in the bulk gas phase, i.e. $p_1 = p_2$.

where

b_i	dual-Langmuir-Freundlich constant for species *i*, $Pa^{-\gamma i}$
p_i	bulk gas phase pressure of species *i*, Pa
p_t	total bulk gas phase pressure of mixture, Pa
q_i	molar loading of species *i*, mol kg^{-1}
$q_{i,sat}$	saturation capacity of species *i*, mol kg^{-1}
S_{ads}	adsorption selectivity, dimensionless
$_i$	exponent in the dual-Langmuir-Freundlich isotherm fits, dimensionless
A, B	referring to adsorption sites A, and B
sat	referring to saturation conditions

4.3 Results and Discussion

The ligand precursor for preparing such MOP is 5-((triisopropylsilyl)ethynyl)isophthalic acid (H_2tei) (Figure 30). It has the isophthalate moiety that can readily participate in the formation of MOP,[6,8] leaving the bulky triisopropylsilyl (TIPS) groups covering the outside.

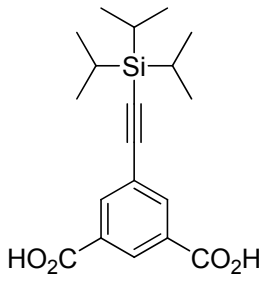

Figure 30. The chemical structure of H_2tei.

The initial solvothermal reactions between H_2tei and copper salts yielded amorphous precipitate that denied any further characterization. Inspired by the fast formation kinetics of these MOP,[173] we adopted an alternative approach, in which H_2tei was first deprotonated by a sterically hindered base (2,6-lutidine) and then reacted with $Cu(NO_3)_2 \cdot 2.5H_2O$ (see supporting information for details). Recrystallization from chloroform/DMF afforded single crystal suitable for X-ray crystallography study. As has been anticipated, the crystal of Cu(tei) is composed of large discrete porous coordination nanocages constructed from the paddlewheel clusters bridged by the isophthalate moieties (Figure 31, Figure 32).[6,8] Like its Cu(*m*-BDC) analogue,[6,8] Cu(tei) has 8 triangular and 6 square windows. The yellow ball in the middle of this nanocage representing its void has a diameter of around 11 Å.

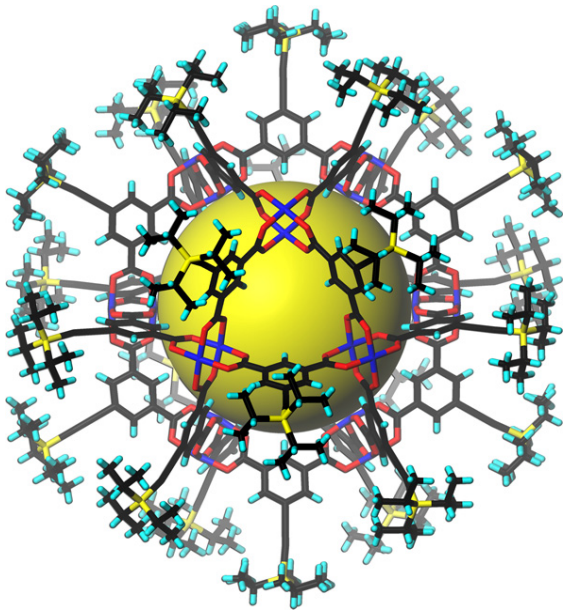

Figure 31. The porous coordination nanocage Cu(tei).

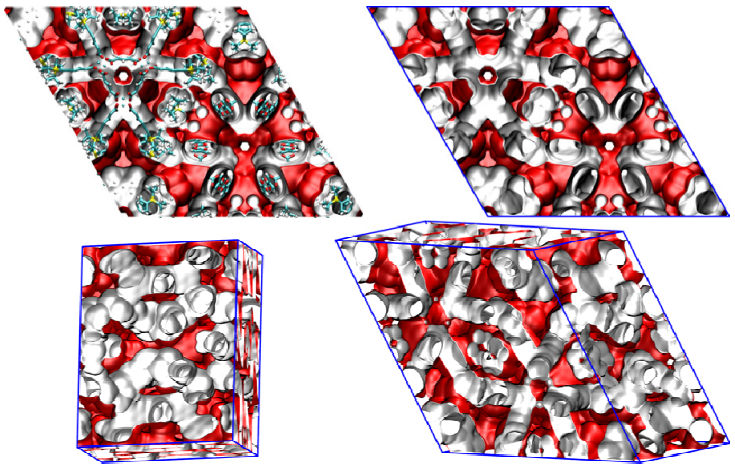

Figure 32. Pore landscapes of Cu(tei) (the red areas are accessible to guest molecules).

Gas sorption measurements were carried out to check Cu(tei)'s porosity. Before these measurements, Cu(tei) was heated at 120 °C under dynamic vacuum overnight, an activation condition that is vigorous enough to remove any residual solvents. As shown in Figure 33, N_2 has barely any sorption at all at 77 K, and is accompanied by a huge hysteresis between adsorption and desorption isotherm branch. Compared to N_2, H_2 has a much higher uptake at 77 K, with a strong hysteresis too. When the temperature is raised up by 10 °C to 87 K, however, the overall H_2 uptake increases as well, a phenomenon that is very rare in exothermic physisorption process. In addition, the huge hysteresis observed at 77 K is greatly diminished. Raising the temperature further to 113 K leads to the lowest H_2 uptake, with barely any hysteresis at all. The same trend is observed in methane sorption isotherms. Lower temperature (113 K) gives lower gas uptake and larger hysteresis. Raising temperature (142 K) yields huge jump in the gas uptake. With increasing temperatures (179 K, 195 K and 273 K) the gas uptake is

impaired and the hysteresis phenomenon is less prominent. Apparently there is a thermosensitive gate opening property within Cu(tei): at certain temperature range, increasing temperature will lead to larger pores to accommodate more adsorbates.

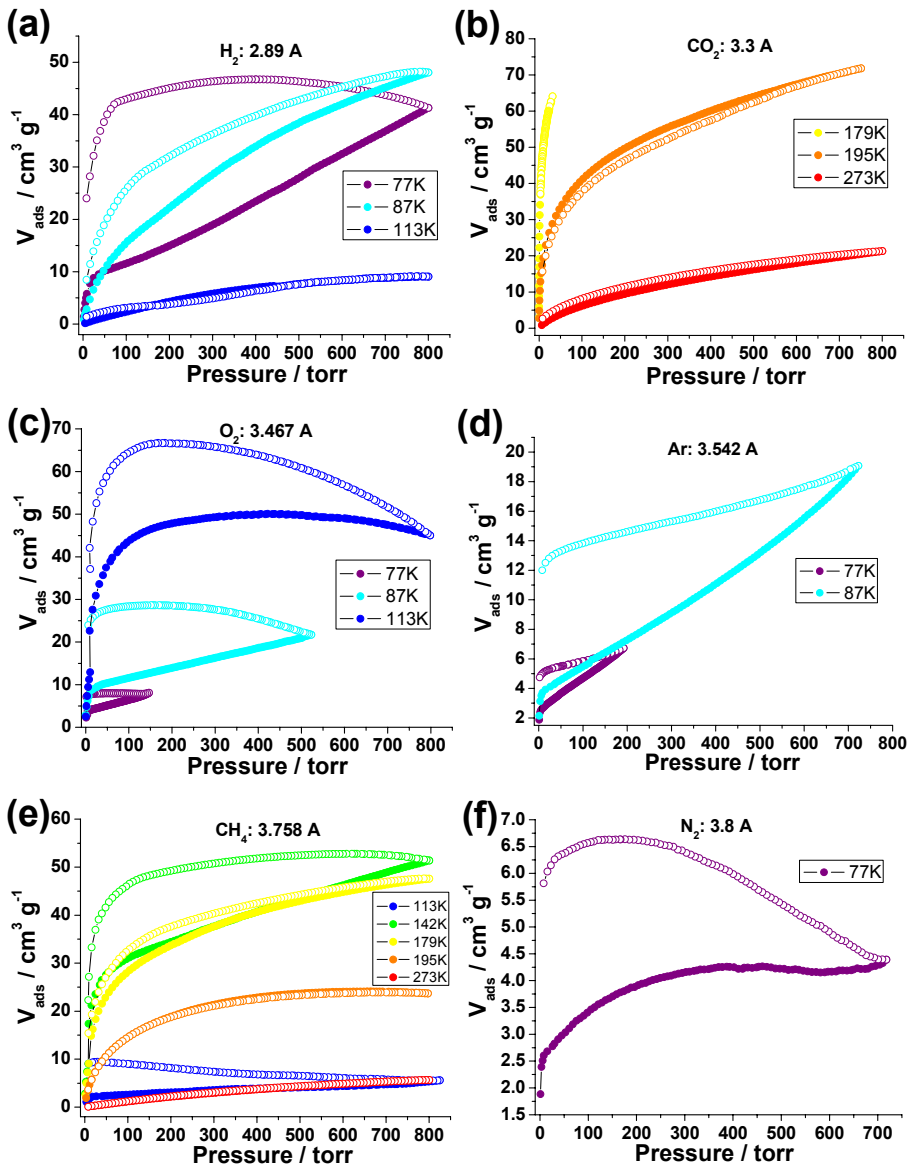

Figure 33. Gas sorption isotherms of Cu(tei) under various temperatures.

In order to understand the above experimental data, molecular simulations were performed using perfect Cu(tei) crystal as the model. The GCMC simulations were carried out to determine the CH_4 and Ar adsorption isotherms at different temperature. We note that the experimental data are consistently about an order of magnitude lower than the simulated results (Figure 34).

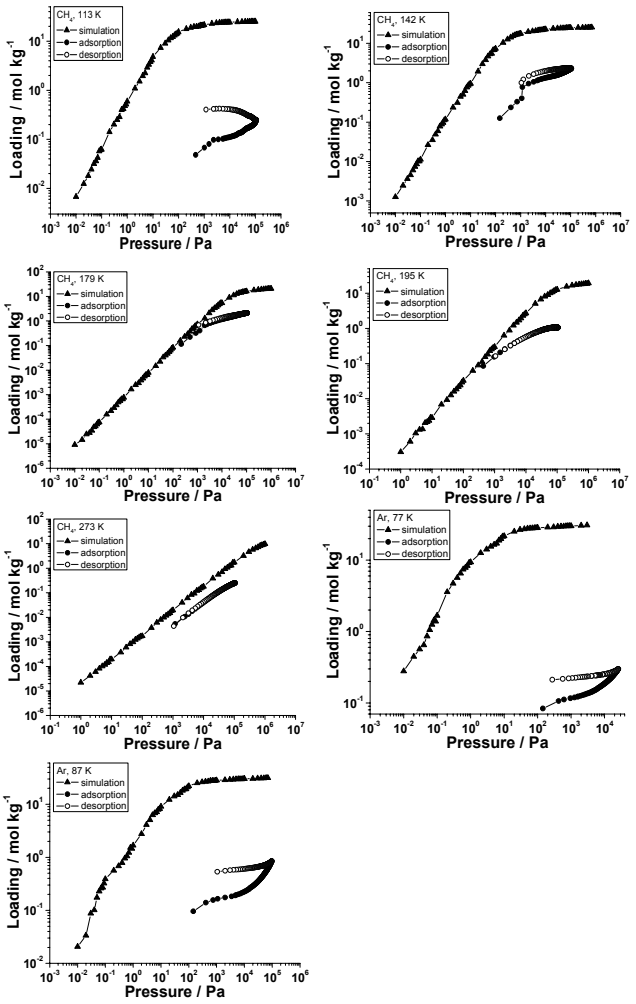

Figure 34. Comparison of GCMC simulations of CH_4 and Ar isotherms for CuTEI with experimental adsorption-desorption data.

Such apparently lower experimental data indicate either a structural change in the Cu(tei) crystal during the activation process, or a substantially low diffusivity of adsorbates within Cu(tei) under the testing temperature. In order to verify the second possibility, Molecular Dynamics (MD) simulations were carried out to determine the self-diffusivity of CH_4 at different temperature for a variety of loadings (Figure 35). The self-diffusivities decrease slightly with increasing loading, which is consistent with other porous materials.[174] Comparison of the self-diffusivities of CH_4 in Cu(tei) at 300 K with the MD simulation data for MOFs (MOF-5, CuBTC), and zeolites (FAU, MFI) available in the published literature indicates that the self-diffusivity of CH_4 in Cu(tei) is slightly lower than that in the open structures such as MOF-5, CuBTC and FAU, but is significantly higher than that in MFI zeolite that has a medium-pore size of 5.6 Å (Figure 36).[174-176] Based on the simulation data, we can conclude that the diffusion of CH_4 in Cu(tei) is comparable to that in large-pore zeolites and MOFs.

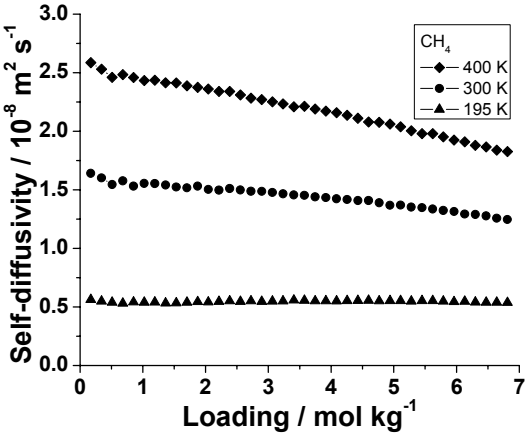

Figure 35. MD simulations for the self-diffusivity of CH_4 in Cu(tei) at 195 K, 300 K and 400 K.

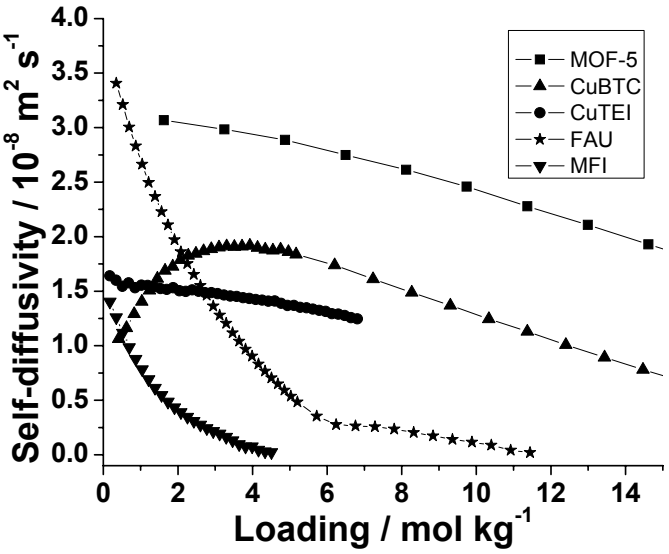

Figure 36. Comparison of MD simulations for the self-diffusivity of CH_4 in Cu(tei) at 300 K with corresponding data for MOFs (MOF-5, CuBTC), and zeolites (FAU, MFI).

The above simulations, however, overlook two factors that are of paramount importance in interpreting the above-mentioned anomalous gas sorption behavior. The first one is the thermal vibration of TIPS group. The Cu(tei) structure was considered to be rigid in the simulations. However, TIPS groups are highly likely to function as gates by undergoing thermal vibration within Cu(tei), giving this material the thermosensitive gate opening property that is identical with the MAMSs. The second one is the structural change. All the simulations were based on perfect Cu(tei) crystal structure. During the activation process, nevertheless, the discrete Cu(tei) molecule tends to move around due to the lack of a strong holding force. Such movement leads to an amorphous structure (Figure 37). As a result, the channels and openings toward the inner void in the perfect crystal model are partially reduced and blocked by the close packing of adjacent

nanocages and extruded TIPS groups in the activated sample, yielding abundant "kinetically closed pores".[177] In these pores, the pore space becomes inaccessible by adsorbate at low temperature. This is due to the lower kinetic energy of the adsorbate molecule at low temperature, which cannot overcome the potential barriers at the aperture of pores that can otherwise accommodate them.[177] Apparently, increasing temperature will have two effects in Cu(tei)'s gas sorption. First, it increases the adsorbate' diffusivity due to increased kinetic energy, which we attribute to as kinetic effect. Second, it weakens the adsorbate/adsorbent affinity and decreases P/P_0 at a certain pressure, which we attribute to as thermodynamic effect. The kinetic effect will boost the gas uptake while the thermodynamic effect will lower it. The overall gas uptake is the balance between these two effects. At low temperature range, the kinetic effect outperforms the thermodynamic one, and that's why the uptake of H_2, O_2 and Ar in Cu(tei) is higher at 87 K than at 77 K. At higher temperature range, the thermodynamic effect becomes dominant, which leads to lower gas uptake observed for H_2 at 113 K and CH_4 at 179 K and above. The CO_2 sorption is a special case. Under these testing temperatures (179 K, 195 K, and 273 K), CO_2 molecules have sufficient kinetic energy to diffuse within Cu(tei) freely, and the kinetic effect becomes trivial. As a result, no hysteresis is observed and the overall sorption behavior is controlled by the thermodynamic effect solely.

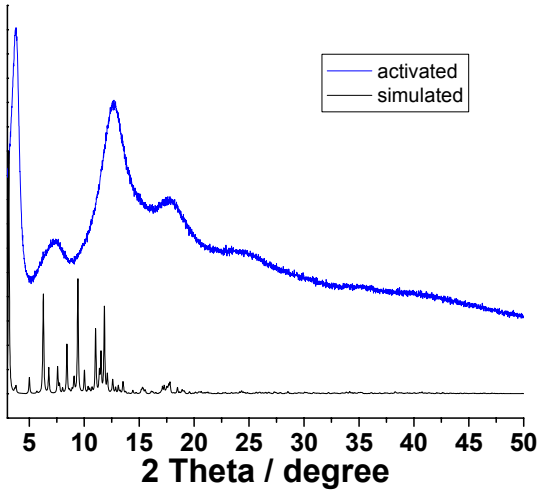

Figure 37. PXRD patterns of Cu(tei).

This abnormal gas sorption behavior (at certain temperature range, higher temperature gives higher gas adsorption) was reported in MAMSs and other MOFs with flexible motif and was attributed to the thermal vibration of these flexible motifs functioning as gates.[161-162,178] However, the same behavior was observed in coal, zeolite, and rigid MOFs as well.[179-184] Under these circumstances, it is more appropriate to attribute this phenomenon to the increased kinetic energy of adsorbates at higher temperature. It is hard to determine which factor dominates the gas sorption behavior in Cu(tei), and both seem feasible. Theoretical study indicates that longer equilibrium time would be needed for the adsorbate to diffuse into the kinetically closed pore.[177,185] Accordingly, by extending the equilibrium time, the gas uptake should increase as well. To confirm that, N_2 sorption isotherms at 77 K was recollected at an eightfold longer equilibrium time (65 hours vs. 8 hours), and there is indeed a dramatic increase of N_2

uptake, especially at the lower pressure range (< 10 Torr) (Figure 38). Apparently, the kinetically closed pores play an important role in the gas sorption behavior of Cu(tei).

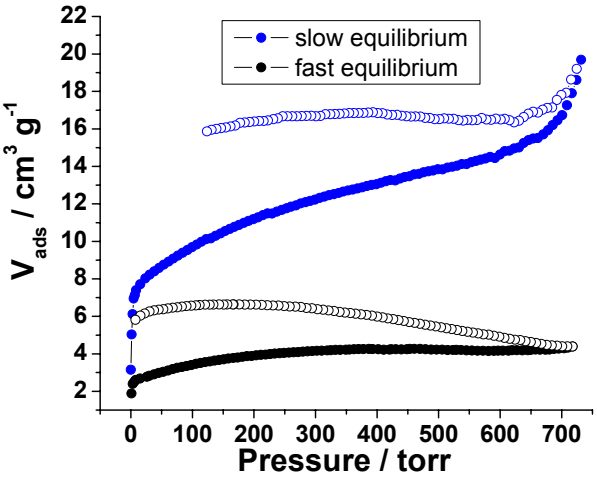

Figure 38. N_2 sorption isotherms for Cu(tei) at 77 K under different equilibrium time.

We propose that since the energy barrier of the aperture's potential can be overcome by the adsorbate's higher chemical potential at high pressure, the kinetic effect can be suppressed under high pressure, leaving only the thermodynamic effect. This is proved by high pressure H_2 adsorption in Cu(tei) at 77 K and 87 K (Figure 39), where the maximal H_2 uptake is higher at 77 K than at 87 K. This is opposite to the low pressure data and confirms our speculation. Besides, the high pressure H_2 sorption kinetic study indicates that it takes much longer time to reach equilibrium for both adsorption and desorption at 77 K than at 87 K, indicating the small aperture's strong retarding effect on hydrogen's self-diffusivity in Cu(tei) at low temperature (Figure 40).

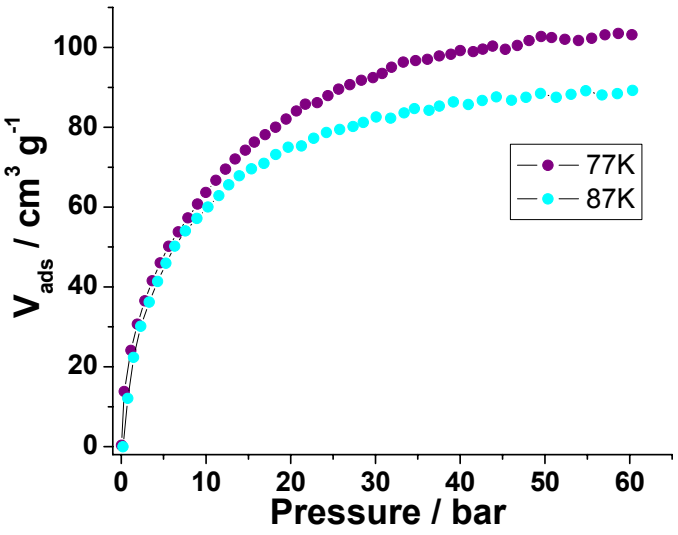

Figure 39. High pressure H_2 adsorption isotherms for Cu(tei).

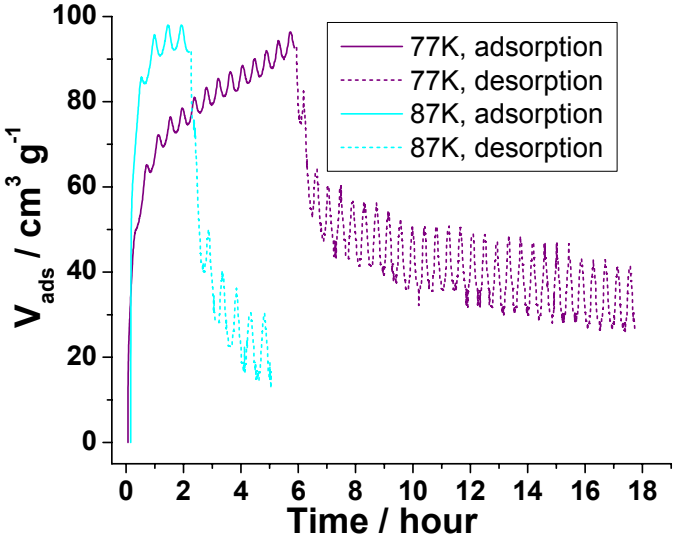

Figure 40. H_2 sorption kinetics for Cu(tei) (the zigzag noise comes from the temperature fluctuation of the gas reservoir).

By plotting different gas uptake data at the same temperature together, one can see a distinct molecular sieving effect, especially at 77 K and 87 K, where the gas being mostly adsorbed is the smallest one, while the larger gas exhibits less sorption (Figure 41).

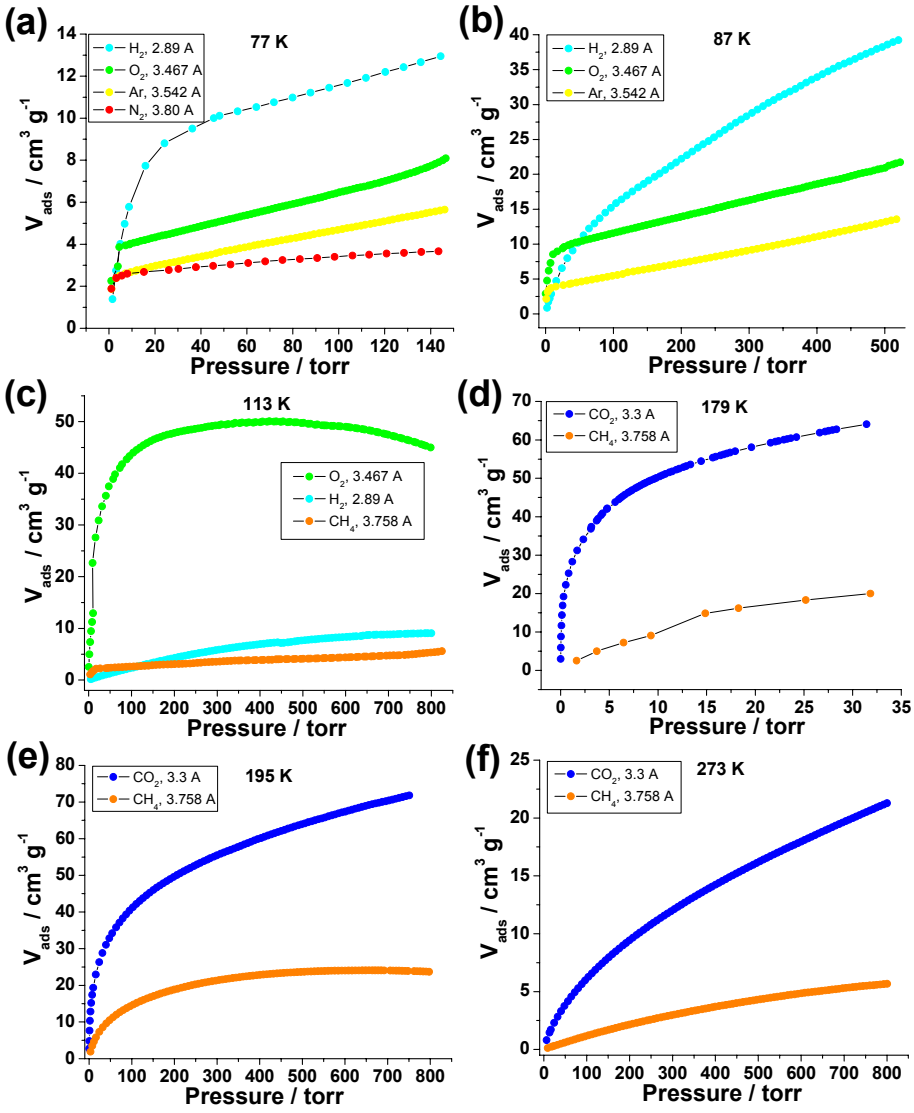

Figure 41. Thermosensitive molecular sieving effect in Cu(tei).

It is worth noting that Cu(tei) exhibits preferential sorption of CO_2 over CH_4 persistently under all the testing temperatures (179 K, 195 K, 273 K and 298 K). The CO_2/CH_4 adsorption selectivity in Cu(tei) was estimated via the ideal adsorbed solution theory (IAST) using the adsorption data at 298 K (Figure 42), which is found to be comparable with the CO_2/CH_4 selectivity in MOFs (MOF-5, CuBTC) and zeolites (FAU, MFI) based on GCMC simulation results (Figure 43).[186] This selective gas adsorption property makes Cu(tei) an appealing candidate in the gas separation purpose.

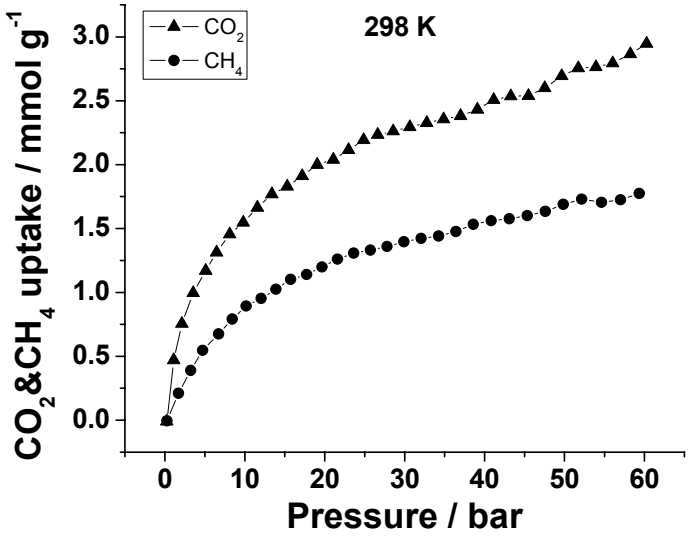

Figure 42. High pressure CO_2 and CH_4 adsorption isotherms for Cu(tei) at 298 K.

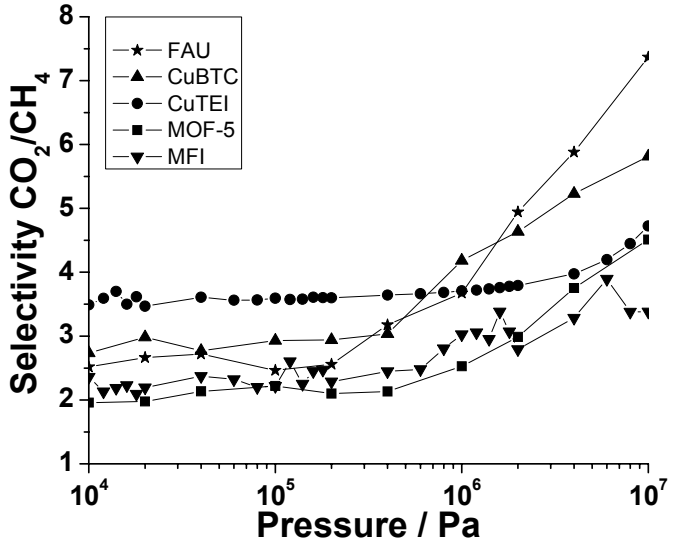

Figure 43. IAST calculations of the adsorption selectivity for CO_2/CH_4 mixtures at 298 K in Cu(tei) as a function of the total gas pressure for an equimolar mixture, $p_1=p_2$.

4.4 Conclusions

MOP covered with bulky triisopropylsilyl group exhibits a thermosensitive gate opening property. This material demonstrates a molecular sieving effect at a certain temperature range, which could be used for gas separation purpose.

5. A CLICKABLE METAL-ORGANIC CUBOCTAHEDRON FOR ANTICANCER DRUG DELIVERY

5.1 Introduction

The discrete coordination-driven self assemblies have received continuous attention due to their molecular architecture esthetics and potential applications in recognition, catalysis, storage, etc.[187-189] Among these self assemblies, one species that has emerged recently is the metal-organic polyhedra (MOP), which are porous coordination nanocages and are represented by the cuboctahedron nanoball formed between 12 dimetal paddlewheel clusters and 24 isophthalate structural moieties.[6-11] Due to their robust porous structure and versatile functionality, they have found applications as plasticizer, gas sponge, ion channel, coatings, and building units.[12-17] Presumably, the porous structure and hollow void make them a good candidate as drug carriers. However, almost all the MOP reported so far are hydrophobic, which greatly limits their applications in aqueous condition. The postsynthetic modification has been proved as an effective way to alter the property of metal-organic frameworks (MOFs).[190] Accordingly, by postsynthetic modifying MOP with hydrophilic moieties, their water solubility should be greatly enhanced. In this section, we report a metal-organic cuboctahedron and its postsynthetic modification by grafting with hydrophilic polymer polyethylene glycol (PEG) through “click chemistry” (Figure 44). In addition, its drug load and release capacity has been evaluated using an anticancer drug 5-fluorouracil as a model.

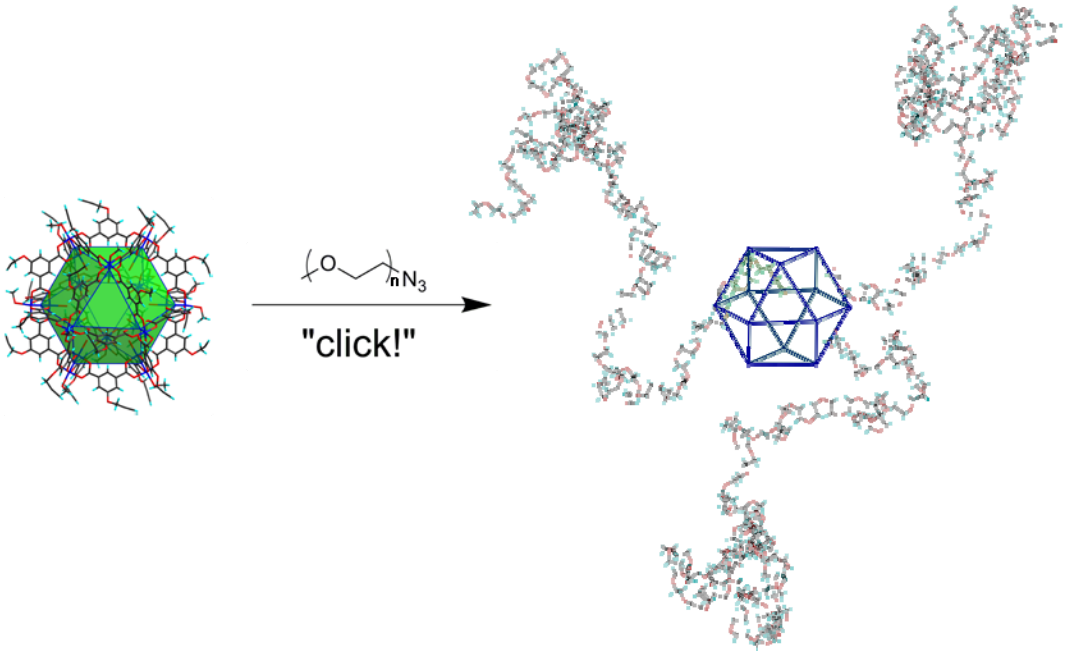

Figure 44. Surface functionalization of a MOP with click chemistry.

5.2 Experimental Section

Materials and methods. Commercially available reagents were used as received without further purification. Nuclear magnetic resonance (NMR) data were collected on a Mercury 300 MHz NMR spectrometer. Fourier transform infrared spectroscopy (FTIR) data were collected on a SHIMADZU IRAffinity-1 FTIR Spectrophotometer. Ultraviolet/Visible (UV-Vis) absorption spectra were recorded on a SHIMADZU UV-2450 UV-Vis Spectrophotometer. Thermogravimetry analyses (TGA) were performed under N_2 on a SHIMADZU TGA-50 Thermogravimetric Analyzer, with a heating rate of 5 °C min^{-1}. Elemental analyses (C, H, and N) were obtained from Canadian Microanalytical Service, Ltd. Elemental analyses (Cu and F) were obtained via thermal

instrumental neutron activation method (INAA) from Elemental Analysis Laboratory at Texas A&M University. Powder X-ray diffraction (PXRD) patterns were obtained on a BRUKER D8-Focus Bragg-Brentano X-ray Powder Diffractometer equipped with a Cu sealed tube (λ = 1.54178) at a scan rate of 0.2 s deg^{-1}, solid-state detector, and a routine power of 1400 W (40 kV, 35 mA). Transmission electron microscopy (TEM) images were obtained on a FEI Tecnai G2 F20 FE-TEM. Dynamic light scattering (DLS) data were obtained on a Brookhaven ZetaPALS. High performance liquid chromatography (HPLC) analysis was carried out on a SHIMADZU Prominence UFLC.

Synthesis of 5-(prop-2-ynyloxy)isophthalic acid, H_2pi. Dimethyl-5-(propargyloxy)isophthalate[191] (4.96 g, 20 mmol) was suspended in 150 mL of THF/methanol (1/1) mixed solvent, to which 100 mL of 1 M NaOH aqueous solution was added. The mixture was refluxed overnight. Organic solvent was removed under vacuum, and diluted hydrochloric acid was added to the remaining aqueous solution until it became acidic (pH = 2). The precipitate was collected by filtration, washed with water and dried under vacuum at 80 °C to give 4.4 g H_2pi as a white solid (yield: 95%). ν_{max}(neat)/cm^{-1} 3084, 2133, 1710, 1595, 1209, 1049, 902 and 758; δ_H(300 MHz; DMSO-d_6; Me_4Si) 8.11 (1 H, t, *J* 3), 7.72 (2 H, d, *J* 3), 4.95 (2 H, d, *J* 3) and 3.62 (1 H, t, *J* 3); δ_C(300 MHz; DMSO-d_6; Me_4Si) 166.31, 157.30, 132.61, 122.91, 119.60, 78.95, 78.67 and 55.93; *m/z* (ESI) 136.02 (74%), 175.038 (41%) and 219.029 (M^-, 100%).

Synthesis of Cu(pi). H_2pi (110.1 mg, 0.5 mmol) was dissolved in 200 mL of benzene/methanol (19/1) mixed solvent, to which 2,6-lutidine (107.1 mg, 1 mmol) dissolved in 5 mL of methanol was added. The solution was sonicated for 10 min to

insure complete deprotonation. $Cu(NO_3)_2 \cdot 2.5H_2O$ (116.3 mg, 0.5 mmol) dissolved in 5 mL of methanol was added into the previous solution. The solution turned into homogeneous deep blue. Single crystal suitable for X-ray diffraction experiment can be collected as precipitate by repeating the above procedure with double reagent concentration. The final product was isolated as deep blue powder (124.4 mg, yield: 83%) by removing the organic solvent, washing with methanol three times and drying under vacuum overnight. The product has a formula of $[Cu(pi)(H_2O)]_{24}$, which was derived from crystallographic data, elemental analysis (% calc/found: C 44.08/44.25, H 2.69/2.97), and TGA. ν_{max}(neat)/cm^{-1} 2121, 1631, 1585, 1377, 1047, 773 and 732. The dried product is insoluble in 20 different solvents we tested (such as hexane, dichloromethane, chloroform, THF, methanol, DMF, DMSO, etc.).

Synthesis of Cu(pi)-PEG5k. H_2pi (44 mg, 0.2 mmol) was dissolved in 150 mL of benzene/methanol (19/1) mixed solvent, to which 2,6-lutidine (43 mg, 0.4 mmol) dissolved in 5 mL of methanol was added. The solution was sonicated for 10 min to insure complete deprotonation. $Cu(NO_3)_2 \cdot 2.5H_2O$ (47 mg, 0.2 mmol) dissolved in 5 mL of methanol was added into the previous solution. The solution turned into homogeneous deep blue, which underwent freeze-pump-thaw cycle three times to eliminate oxygen. 0.5 mL of trimethyl orthoformate in 10 mL of dry DMF was added and the solution was refluxed for two hours to eliminate residual water. PEG5k-N_3[192] (1 g, 0.2 mmol, molecular weight = 5000) in 50 mL of dry dichloromethane, $Cu(CH_3CN)_4PF_6$ (75 mg, 0.2 mmol) in 10 mL of dry dichloromethane, and 2,6-lutidine (2 mg, 0.02 mmol) were added sequentially. The solution was stirred at room temperature under N_2 atmosphere

for 24 hours, during which time the color turned from blue to green. After the reaction, the organic solvent was removed under vacuum and the residue was redissolved in dichloromethane and forced through a short silicone gel column to eliminate polar impurity. The final product (523.9 mg) was isolated as azure plastic solid after being dried under vacuum, which can be readily dissolved in ordinary organic solvents, such as chloroform, THF, methanol, etc. ν_{max}(neat)/cm^{-1} 2881, 1466, 1341, 1279, 1097, 962 and 840. Elemental analyses: C, 53.87; H, 8.66; N, 0.69; Cu, 1.75.

X-ray crystallography. Single crystal X-ray structure determination of Cu(pi) was performed at 173(2) K on the Advanced Photon Source on beamline 15ID-B in Argonne National Laboratory. Raw data for the structure were processed using APEX-II and absorption corrections were applied using SADABS. Structures were solved by direct method and refined by full-matrix least-squares on F^2 using *SHELXTL*.[122] Non-hydrogen atoms were refined with anisotropic displacement parameters during the final cycles. Organic hydrogen atoms were placed in calculated positions with isotropic displacement parameters set to 1.2 × U_{eq} of the attached atom. The solvent molecules are highly disordered, and attempts to locate and refine the solvent peaks were unsuccessful. Contributions to scattering due to these solvent molecules were removed using the *SQUEEZE* routine of *PLATON*;[123] structures were then refined again using the data generated. Due to the small crystal size, the diffraction remained weak even under synchrotron radiation, and it is not possible to obtain a significantly better crystallographic model using methods currently available. Although the data in hand are poor, we still believe they support our interpretation.

Crystal data for Cu(pi): $C_{46}H_{36}Cu_4O_{24}$, M = 1226.91, blue prism, 0.03 * 0.02 * 0.02 mm^3, cubic, space group *Pa*-3 (No. 205), a = 34.4828(16), V = 41002(3) $Å^3$, Z = 24, D_c = 1.193 g/cm^3, F_{000} = 14880, synchrotron radiation, λ = 0.41328 Å, T = 173(2)K, $2\theta_{max}$ = 23.9º, 528271 reflections collected, 7192 unique. Final *GooF* = 2.713, *R1* = 0.2499, *wR2* = 0.5803, *R* indices based on 6588 reflections with I >2sigma(I) (refinement on F^2), 315 parameters, 63 restraints. μ = 0.681 mm^{-1}.

Low-pressure gas sorption measurements. The low-pressure gas sorption isotherm measurements were performed at 77 K (liquid nitrogen bath) on a Micromeritics ASAP 2020 surface area and pore size analyzer. Before measurements, the sample was degassed for 10 hours at 30 °C. UHP grade (99.999%) N_2, He, and H_2 were used for all measurements. Oil-free vacuum pumps and oil-free pressure regulators were used for all measurements to prevent contamination of the samples during the degassing process and isotherm measurement. Pore size distribution analysis was carried out using DFT model in the Micromeritics ASAP 2020 software package.

Gel permeation chromatography. The molecular weight and molecular weight distribution of Cu(pi)-PEG5k were determined by gel permeation chromatography (GPC) on a Waters GPC system consisting of a Waters 1515 isocratic HPLC pump, Waters Styrage® columns (HR3, HR4, and HR5; 7.8×300 mm) and a Waters 2414 refractive index detector. The whole system was maintained at room temperature. THF was used as the mobile phase (1 mL/min), and the system was calibrated with narrow-disperse polystyrene standards. The sample was prepared by dissolving in THF at a concentration of 0.3 wt%.

Mass spectrometry. Matrix assisted laser desorption ionization (MALDI) experiments were performed on a Voyager DE-STR mass spectrometer (Applied Biosystems, Foster City, CA) under optimized conditions in positive linear mode. Ions were generated by a pulsed nitrogen laser at 337 nm and accelerated through 25 kV. About 100 laser shots were used per spectrum. 3-Indoleacrylic acid was used as a matrix. The sample was dissolved in dichloromethane and matrix in tetrahydrofuran at concentrations of 10 and 38 mg/ml respectively. The sample solution was mixed with the matrix at a volume ratio of 1:6. About 0.5 μl of this mixture was deposited on a stainless steel sample holder. After air-dried, the sample was analyzed using MALDI MS.

Drug loading. Since 5-fluorouracil (5-FU) is soluble in methanol while insoluble in chloroform, loading 5-FU into Cu(pi)-PEG5k is based on this solubility difference. Dissolving 20 mg of 5-FU and 20 mg of Cu(pi)-PEG5k in 20 mL of methanol overnight yielded homogenous light blue solution. Methanol was removed under vacuum and the residua were extracted with chloroform. The unloaded 5-FU was discarded as precipitate and the loaded 5-FU was readily soluble in chloroform. 5-FU loaded Cu(pi)-PEG5k was obtained after the removal of chloroform. The 5-FU content was calculated by determining the fluorine content in 5-FU loaded Cu(pi)-PEG5k using thermal instrumental neutron activation method (INAA). To test the drug embedded within the polymeric corona, pure PEG5k-N_3 was also subjected to the same drug loading process.

Drug release. 15 mg of 5-FU@Cu(pi)-PEG5k was loaded into a dialysis bag (MWCO = 1000), which was dialyzed against 500 mL of PBS buffer solution (pH 7.4) at

room temperature. During each time interval, 1 mL of solution was taken out, and 1 mL of fresh PBS buffer was added. The content of 5-FU in the samples taken out was determined by HPLC, in which methanol/50mM acetic acid (6/4, V/V) mixed solvent was used as a mobile phase and the detection wavelength was 268 nm.

5.3 Results and Discussion

The Cu(I)-catalyzed Huisgen cycloaddition between azide and alkyne, a so-called "click reaction", has received a lot of attention recently due to its high yield, mild condition, and easy operation.[193] It has been successfully adopted in several MOFs-based postsynthetic modifications, and is therefore chosen as the synthetic tool in this study.[194-196] Based on the retrosynthetic analysis and implementation convenience, alkyne-covered MOP and azide-terminated PEG are two prerequisites. We chose 5-(prop-2-ynyloxy)isophthalic acid (H_2pi) (Figure 45) as the ligand precursor to prepare alkyne-covered MOP for two reasons: (1) The isophthalate moiety can readily participate in the formation of metal-organic cuboctahedron, with the alkyne group covered outside; (2) The extra ether and methylene linkage at the 5 position of isophthalate moiety helps to increase the solubility of the MOP product, facilitating the crystallization and succedent click reaction.

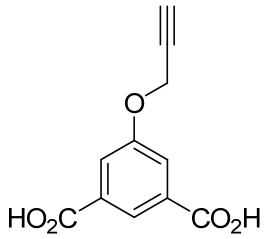

Figure 45. The chemical structure of H_2pi.

The initial solvothermal reactions between H_2pi and copper salts yielded amorphous precipitate that denied any further characterization. Inspired by the fast formation kinetics of MOP,[173] we adopted an alternative approach, in which the H_2pi was first deprotonated by a sterically hindered base (2,6-lutidine) and then reacted with copper salt. Based on the reagent concentration, the final product solution could be either homogenous clear or have some crystals precipitated after being placed still overnight. The single crystal X-ray diffraction reveals that these crystals are indeed the target MOP (Figure 46).

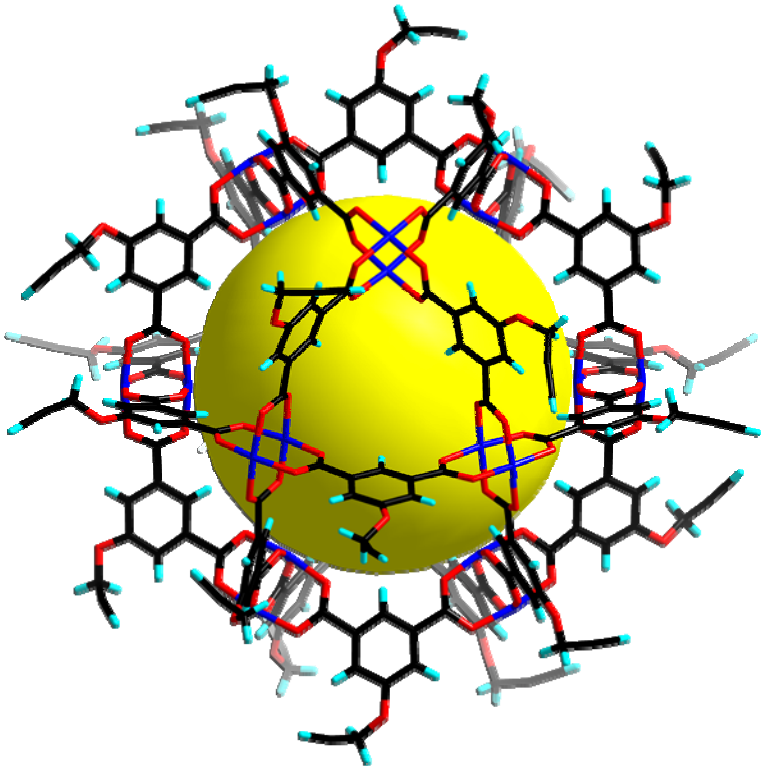

Figure 46. The clickable metal-organic cuboctahedron Cu(pi).

The N_2 sorption at 77 K of dry MOP sample (referred to as Cu(pi) hereafter) shows a Type IV isotherm, with a BET surface area of 29 m^2/g (Langmuir surface area: 40 m^2/g) (Figure 47). The pore size distribution analysis reveals a smallest pore at 11.79 Å, which fits well with the inner void size of the cuboctahedron read from the crystal data (diameter 15.868 Å, measured Cu···Cu) (Figure 48). The wide pore size distribution (ranging from microporous to macroporous) may come from the spacing between Cu(pi) agglomerates, and that explains the hysteresis in the N_2 isotherms. Although there are wide openings in Cu(pi) based on the crystal model, the discrete MOP molecule tends to move around during the drying process due to the lack of strong holding force, leading

to amorphous structure and partially reduced and blocked opening in the final dry Cu(pi) sample (Figure 49). That may be the reason why the quantity of N_2 being adsorbed within Cu(pi) is substantially smaller than that in other MOP.[13,18-20] In order to verify this hypothesis, H_2 was chosen as a smaller gas probe and its uptake in Cu(pi) was also tested. As has been speculated, given the same temperature and pressure, the quantity of H_2 being adsorbed within Cu(pi) is much higher than that of N_2, a clear evidence for the proposed molecular sieve effect (Figure 47). In addition, a noticeable hysteresis was also observed in the H_2 isotherms, indicating a strong retard on the gas diffusion.[197] The above preferential adsorption of H_2 over N_2 in Cu(pi) at 77 K is reminiscent of that in Cu(tei) discussed above, and it is probably due to the kinetic energy of the adsorbates to overcome a diffusion barrier above a critical temperature.

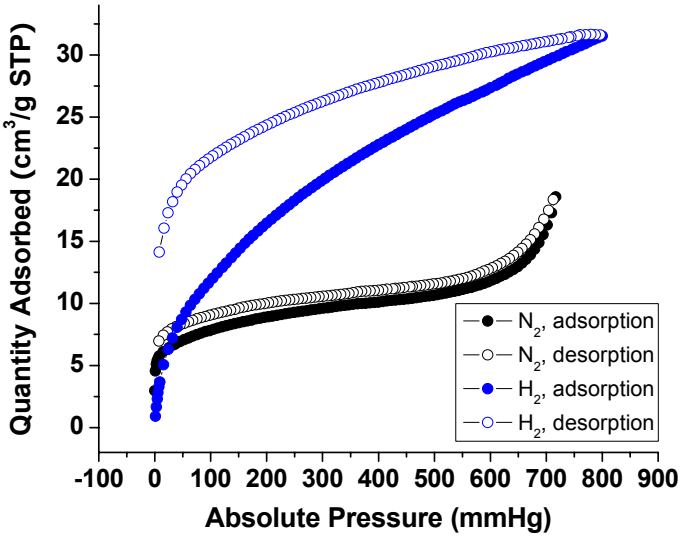

Figure 47. N_2 (black) and H_2 (blue) sorption isotherms of Cu(pi) at 77 K.

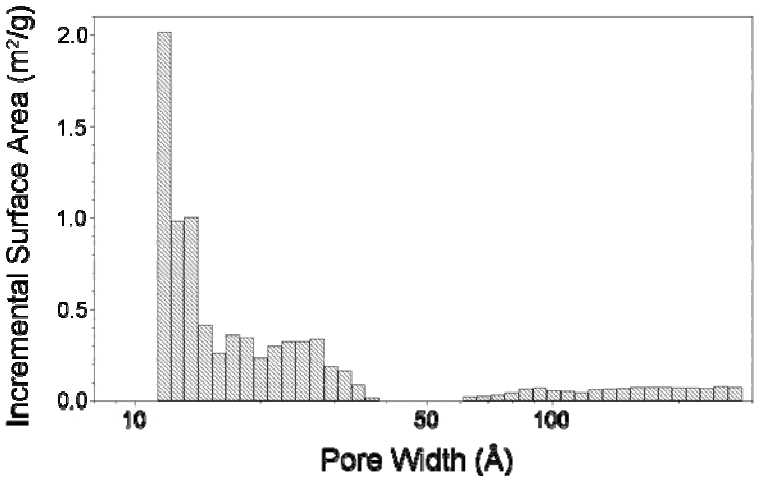

Figure 48. Pore size distribution of Cu(pi).

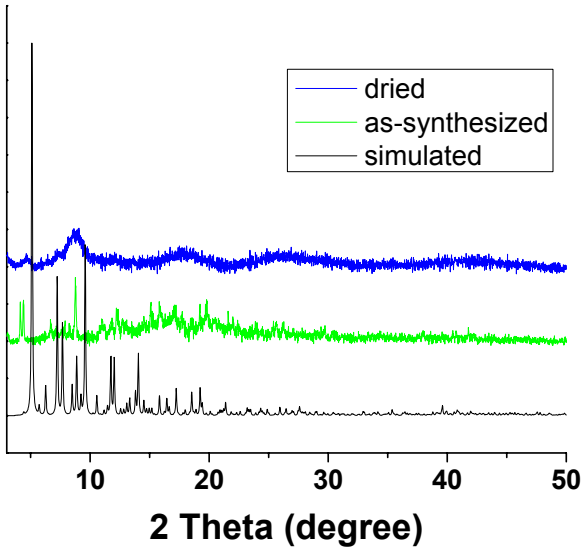

Figure 49. PXRD patterns of Cu(pi).

Once the Cu(pi) sample was isolated from the solution, it became insoluble in all the organic solvents we tried (methanol, THF, DMF, etc.), which may be due to the extremely high solvation energy needed for the MOP molecule. In addition, the possible

hydrogen bonding interaction between terminal alkyne groups in adjacent MOP magnifies this solvation energy needed.[198] In order to reach a smooth reaction and high yield, the click reaction modification was carried out using the *in situ* generated Cu(pi) solution. UV-Vis absorption spectra demonstrate an absorption band shifting of copper nitrate (starting material) from ~790 nm to ~700 nm of the *in situ* generated Cu(pi) solution (Figure 50). The 700 nm absorption band, a so-called Band (I) in binuclear copper(II) acetate, is due to the orbitally forbidden Cu d-d transitions or possibly metal-ligand charge-transfer interactions and is a strong indication of the dicopper paddlewheel cluster.[199-200] After the click reaction, the 700 nm absorption band of the product (referred to as Cu(pi)-PEG5k hereafter) barely changes, indicating the intactness of dicopper paddlewheel cluster during the click reaction modification.

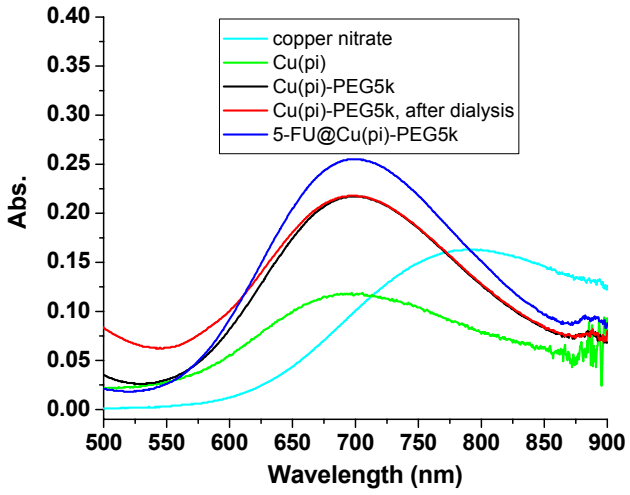

Figure 50. UV-Vis spectra of copper nitrate (azure), Cu(pi) (green), Cu(pi)-PEG5k (black), Cu(pi)-PEG5k after dialysis (red), and 5-FU@Cu(pi)-PEG5k (blue, *vide infra*).

It is also possible that the MOP decompose into fragments during the click reaction without the dicopper paddle cluster being altered. The facile solubility of Cu(pi)-PEG5k (in methanol, THF, chloroform, etc.) prompted us to check the MOP core's intactness using solution-based molecular weight characterization methods. The Cu(pi) core without solvent incorporated and axial ligands bound to copper has a molecular weight of 6761.04. Since there are maximum 24 click reaction sites, the theoretical molecular weight of Cu(pi)-PEG5k should be 6761.04 + 5000*n ($1 \leq n \leq 24$). Gel permeation chromatography (GPC) was used to detect its molecular weight and distribution. As seen in Figure 51, except for the unreacted PEG5k-N_3 peak (1, peak MW: 6538, PDI: 1.04), three new peaks were easily identified (2, peak MW: 12636; 3, peak MW: 18079; 4, peak MW: 26568. PDI all less than 1.04). The possibility of higher molecular weight caused by pure PEG molecular chain entanglement was ruled out by data obtained from the pure PEG5k-N_3 run at the same condition. Due to the dendrimeric shape of Cu(pi)-PEG5k, it is hard to draw precise molecular weight information from the GPC method, which is based on random coil model. However, these peaks with higher molecular weight and narrow molecular weight distribution do shed light on the presumed graft product.

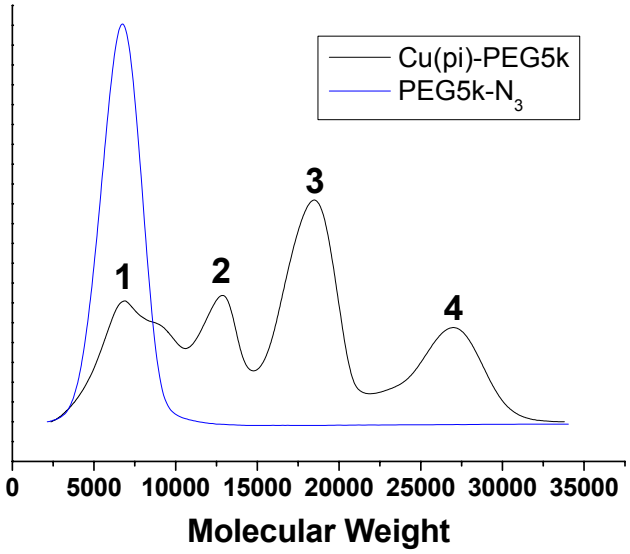

Figure 51. GPC results of Cu(pi)-PEG5k (black) vs. PEG5k-N_3 (blue).

Compared to GPC, mass spectrometry (MS) can give direct molecular weight information. In order to prevent the Cu(pi) core from decomposing, a milder ionization method (matrix assisted laser desorption ionization, MALDI) was used. From the MALDI MS data (Figure 52), we can clearly see the Cu(pi) MOP core that has been grafted with one, two, three, and four PEG chains. The possibility of higher molecular weight caused by pure PEG molecular chain entanglement was ruled out by the data obtained from the pure PEG5k-N_3 run at the same condition (Figure 53). It is hard to tell exactly how many PEG chains have been grafted on one Cu(pi) core. Based on the N and Cu content in Cu(pi)-PEG5k, the ratio of PEG to Cu(pi) core can be calculated, which is ~14. Counting the unreacted PEG5k-N_3, the grafted PEG chains in one Cu(pi)-PEG5k molecule should be even less.

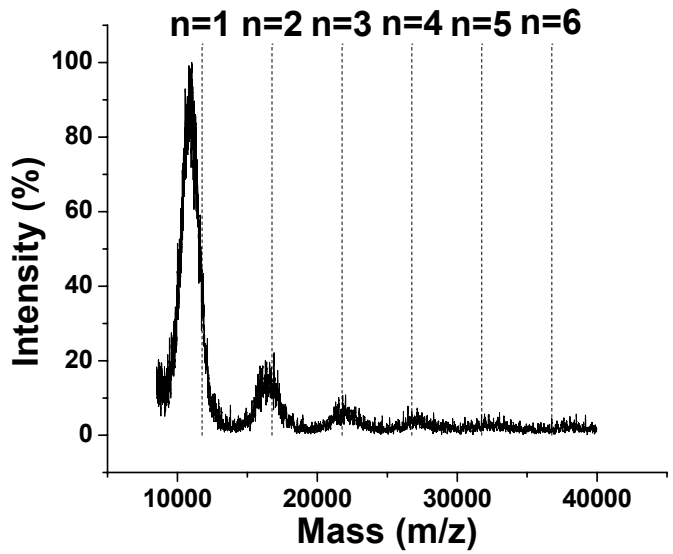

Figure 52. MALDI MS data of Cu(pi)-PEG5k, dash lines represent the theoretical molecular weight of Cu(pi) grafted with various PEG chains.

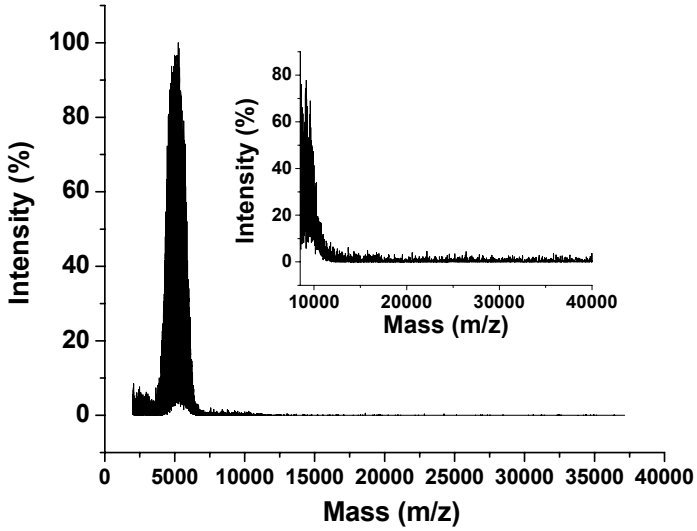

Figure 53. MALDI MS data of pure PEG5k-N_3 (imbedded: zoomed in).

An image taken using dark-field transmission electron microscopy (D-F TEM) (Figure 54) shows nanoparticles with a diameter of around 20 nm, which is consistent with the dynamic light scattering (DLS) data (Figure 55). Energy dispersive spectroscopy (EDS) analysis of these nanoparticles reveals high copper content (Figure 56), a strong indication of the Cu(pi) MOP core. Attempts in getting higher resolution images of these nanoparticles were unsuccessful due to ease of decomposition under intensified electron beam. The dispersed nanoparticles also strongly support successful PEG grafting, otherwise an intense agglomeration would be expected. However, the size of these nanoparticles is much larger than that of an expected single Cu(pi)-PEG5k molecule (the MOP core has a diameter of around 3 nm), which is probably due to the intermolecular aggregation caused by insufficient grafting.

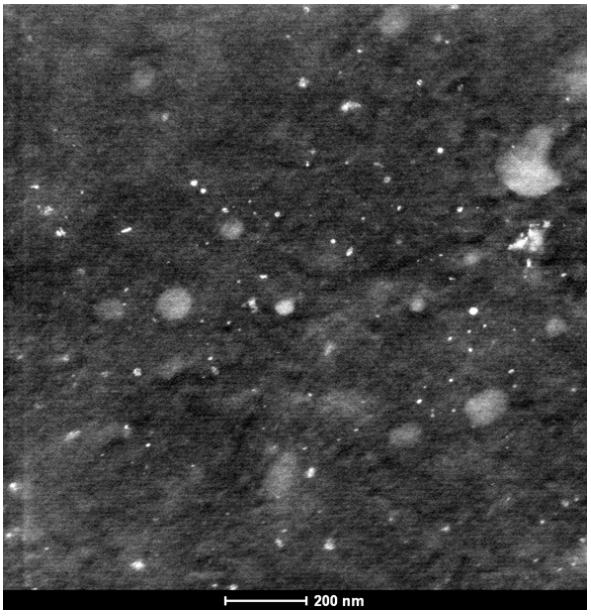

Figure 54. D-F TEM image of Cu(pi)-PEG5k, bar = 200 nm.

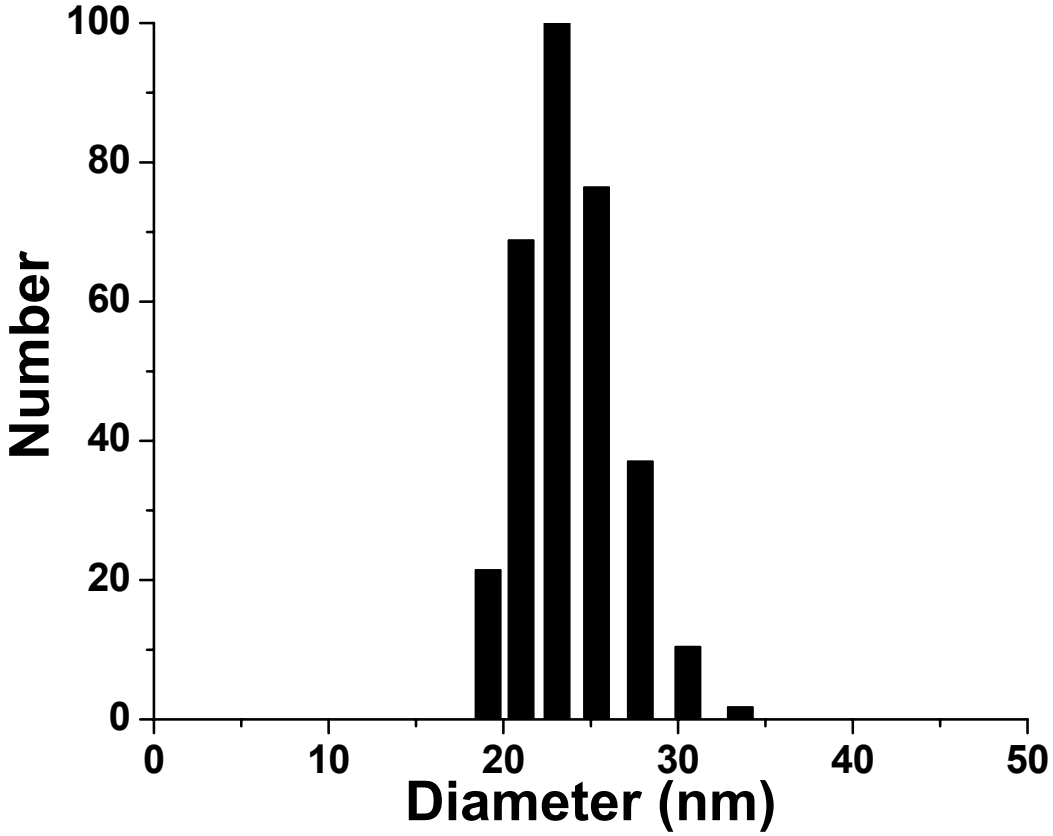

Figure 55. Particle size distribution data of Cu(pi)-PEG5k obtained from DLS.

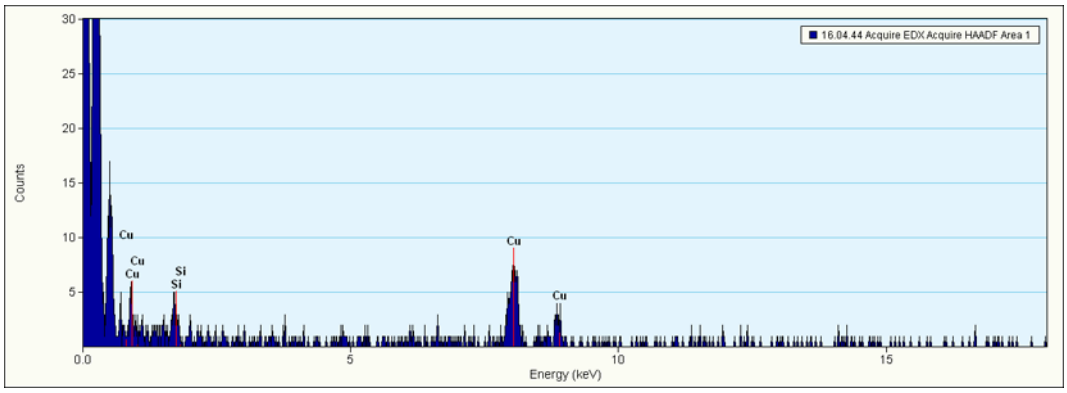

Figure 56. Energy dispersive spectrum (EDS) of TEM area in Figure 54.

It has been well documented that the dicopper paddlewheel cluster is unstable in aqueous condition due to its liability to undergo ligand exchange with water.[201] In order to test its water stability, Cu(pi)-PEG5k was dissolved in water and dialyzed against water for 24 hours. After being lyophilized, the sample was redissolved in methanol and UV-Vis absorption spectrum was taken. As can be seen from Figure 50, the 700 nm absorption band barely changes, indicating the intactness of dicopper paddle cluster and accordingly the stability of Cu(pi)-PEG5k in water. The Cu(pi) MOP were actually turned into metallomicelles once being grafted with PEG chain.[202] Its special water stability may come from the outer polymeric shell and intermolecular aggregation, which protects the dicopper paddle by preventing the water molecules from accessing the MOP core. In addition, the gain of thermodynamic complex stability due to the macrocyclic effect is also a possibility.[15,203]

Given the proven composition and water stability, Cu(pi)-PEG5k was used as a carrier for drug release experimentation. 5-Fluorouracil (5-FU) is a widely used

anticancer drug.[204] It was selected as a perfect model in this study due to its size, which is suitable for loading into the inner void of the Cu(pi) core. Loading 5-FU into Cu(pi)-PEG5k was based on its solubility difference between chloroform and methanol and the loading content was determined to be 4.38 wt % by the elemental analysis of fluorine content in the drug-loaded sample (referred to as 5-FU@Cu(pi)-PEG5k hereafter). The dicopper paddlewheel cluster was not affected by the 5-FU loading, seen from the UV-Vis absorption spectrum (Figure 50). Pure PEG5k-N_3 was also subjected to the same drug loading procedure to distinguish the polymeric corona's contribution. The drug loading content in PEG5K-N_3 is only 0.82 wt %, indicating a higher drug loading capacity in the Cu(pi) core.

Drug release experiments were carried out by dialyzing 5-FU@Cu(pi)-PEG5k against PBS buffer solution (pH 7.4) at room temperature. Pure 5-FU was also dialyzed as a control experiment, in which close to 90% was released within 7 hours (Figure 57). However, for 5-FU@Cu(pi)-PEG5k, less than 20% of the drug was released in the initial burst (2 hours) followed by much flatter release curve monitored for 24 hours. The initial burst release may come from the drug that was imbedded within the outer polymeric corona. The rest of the drug, presumably loaded within the void of Cu(pi) core, was released very slowly, possibly due to the much slower diffusion rate imposed by the strong Cu(pi)-drug interaction.

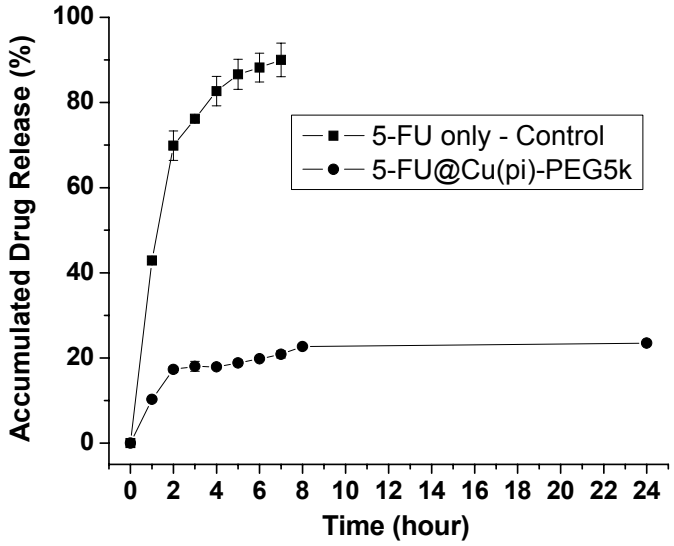

Figure 57. 5-FU release profile from control (square) and Cu(pi)-PEG5k (circle). Data points are mean values of duplicates.

5.4 Conclusions

In summary, a clickable metal-organic cuboctahedron covered with alkyne groups was synthesized through kinetic control. The postsynthetic modification via click reaction with azide-terminated polyethylene glycol turned them into metallomicelles, which showed controlled release of an anticancer drug 5-fluorouracil. In addition, due to paramagnetism of the Cu^{2+} adopted, this PEG grafted MOP may have dual functionality as contrast agent in magnetic resonance imaging applications.[205]

6. CONCLUSIONS

In this dissertation, the chemistry and applications of two kinds of metal-organic materials (MOFs and MOP) have been discussed. It is found that a series of isoreticular MOFs with the same (3,24)-connected network topology can be generated based on hexatopic ligands with C_3 symmetry. In these structures, there are cuboctahedra building units, which have micro-windows that effectively narrow down the opening towards the meso-cavities and stabilize the framework. In addition, these cuboctahedra building units prevent the framework from undergoing interpenetration, leading to high porosity and surface area. One of the MOFs, PCN-68, has a Langmuir surface area as high as 6033 m^2 g^{-1}. At 77 K, it can reversibly uptake 73.2 mg of H_2 per gram, which is among the highest reported so far.

Besides the (3,24)-connected MOFs, we've also discussed a NbO-type MOF that is constructed based on a polyyne-coupled di-isophthalate ligand formed *in situ*. The ensuing MOF has permanent porosity after the removal of guest molecules, with a BET surface area of 2500 m^2 g^{-1} and a uniform pore size around 6.8 Å. The polyyne units in this MOF exhibit high heat of hydrogen adsorption and excellent stability under high-pressure hydrogen. The total methane uptake capacity at 298 K and 35 bar is 172 v(STP)/v, which is very close to DOE 180 v(STP)/v target. In addition, the density of carbon dioxide adsorbed could reach that of liquid carbon dioxide at much lower pressure, indicating that the carbon dioxide stored within MOFs are highly compressed and MOFs-based carbon dioxide capturing is an efficient and energy-reserving approach.

MOP are discrete porous coordination nanocages. Their porosity comes from the inner void of these discrete nanocages, although it is possible that the spacing between these nanocages contributes to their porosity as well. We designed and synthesized a MOP that was formed between 24 isophthalate moieties and 12 dicopper paddlewheel SBU. The bulky TIPS groups covered outside reduced their opening. At a certain temperature range, this material exhibits a thermosensitive gate opening property, to which we attribute as a result of the dynamic opening of the pore and /or sufficient kinetic energy of the gas molecules to overcome a diffusion barrier above a critical temperature. By plotting different gas uptake data at the same temperature together, we can see a distinct molecular sieving effect, especially at 77 K and 87 K, where the gas being mostly adsorbed is the smallest one, while the larger gas exhibits less sorption. This property can be used for gas separation purpose.

Most of the MOP reported so far are hydrophobic, which greatly limits their application in aqueous environment. We designed and synthesized a MOP covered with alkyne groups via kinetic control. The click reaction between these alkyne groups and azide terminated PEG turns this MOP into a “unimolecular metallomicelle”, which can be readily dissolved in water. The intactness of the MOP core and the formation of PEG functionalized MOP were confirmed by UV-Vis, GPC, MALDI MS, TEM, and DLS. This PEG functionalized MOP exhibits the incorporation and controlled release of an anti-cancer drug 5-FU.

REFERENCES

(1) Whitesides, G. M.; Grzybowski, B. *Science* **2002**, *295*, 2418-2421.

(2) Steed, J. W.; Atwood, J. L. *Supramolecular Chemistry*, 2 ed.; Wiley: New York, 2009.

(3) Yaghi, O. M.; O'Keeffe, M.; Ockwig, N. W.; Chae, H. K.; Eddaoudi, M.; Kim, J. *Nature* **2003**, *423*, 705-714.

(4) Kitagawa, S.; Kitaura, R.; Noro, S. *Angew. Chem., Int. Ed.* **2004**, *43*, 2334-2375.

(5) Férey, G. *Chem. Soc. Rev.* **2008**, *37*, 191-214.

(6) Eddaoudi, M.; Kim, J.; Wachter, J. B.; Chae, H. K.; O'Keeffe, M.; Yaghi, O. M. *J. Am. Chem. Soc.* **2001**, *123*, 4368-4369.

(7) Abourahma, H.; Coleman, A. W.; Moulton, B.; Rather, B.; Shahgaldian, P.; Zaworotko, M. J. *Chem. Commun.* **2001**, 2380-2381.

(8) Moulton, B.; Lu, J. J.; Mondal, A.; Zaworotko, M. J. *Chem. Commun.* **2001**, 863-864.

(9) Ke, Y. X.; Collins, D. J.; Zhou, H. C. *Inorg. Chem.* **2005**, *44*, 4154-4156.

(10) Furukawa, H.; Kim, J.; Plass, K. E.; Yaghi, O. M. *J. Am. Chem. Soc.* **2006**, *128*, 8398-8399.

(11) Tranchemontagne, D. J.; Ni, Z.; O'Keeffe, M.; Yaghi, O. M. *Angew. Chem., Int. Ed.* **2008**, *47*, 5136-5147.

(12) Mohomed, K.; Abourahma, H.; Zaworotko, M. J.; Harmon, J. P. *Chem. Commun.* **2005**, 3277-3279.

(13) Furukawa, H.; Kim, J.; Ockwig, N. W.; O'Keeffe, M.; Yaghi, O. M. *J. Am. Chem. Soc.* **2008**, *130*, 11650-11661.

(14) Jung, M.; Kim, H.; Baek, K.; Kim, K. *Angew. Chem., Int. Ed.* **2008**, *47*, 5755-5757.

(15) Tonigold, M.; Hitzbleck, J.; Bahnmuller, S.; Langstein, G.; Volkmer, D. *Dalton Trans.* **2009**, 1363-1371.

(16) Li, J. R.; Timmons, D. J.; Zhou, H. C. *J. Am. Chem. Soc.* **2009**, *131*, 6368-6369.

(17) Perry, J. J.; Perman, J. A.; Zaworotko, M. J. *Chem. Soc. Rev.* **2009**, *38*, 1400-1417.

(18) Sudik, A. C.; Millward, A. R.; Ockwig, N. W.; Cote, A. P.; Kim, J.; Yaghi, O. M. *J. Am. Chem. Soc.* **2005**, *127*, 7110-7118.

(19) Ni, Z.; Yassar, A.; Antoun, T.; Yaghi, O. M. *J. Am. Chem. Soc.* **2005**, *127*, 12752-12753.

(20) Li, J. R.; Zhou, H. C. *Angew. Chem., Int. Ed.* **2009**, *48*, 8465-8468.

(21) Morris, R. E.; Wheatley, P. S. *Angew. Chem., Int. Ed.* **2008**, *47*, 4966-4981.

(22) van den Berg, A. W. C.; Areán, C. O. *Chem. Commun.* **2008**, 668-681.

(23) Schlapbach, L.; Züttel, A. *Nature* **2001**, *414*, 353-358.

(24) Yang, J.; Sudik, A.; Wolverton, C.; Siegel, D. J. *Chem. Soc. Rev.* **2010**, *39*, 656-675.

(25) Grochala, W.; Edwards, P. P. *Chem. Rev.* **2004**, *104*, 1283-1315.

(26) Rosi, N. L.; Eckert, J.; Eddaoudi, M.; Vodak, D. T.; Kim, J.; O'Keeffe, M.; Yaghi, O. M. *Science* **2003**, *300*, 1127-1129.

(27) Zhao, D.; Yuan, D. Q.; Zhou, H. C. *Energy Environ. Sci.* **2008**, *1*, 222-235.

(28) Wong-Foy, A. G.; Matzger, A. J.; Yaghi, O. M. *J. Am. Chem. Soc.* **2006**, *128*, 3494-3495.

(29) Kaye, S. S.; Dailly, A.; Yaghi, O. M.; Long, J. R. *J. Am. Chem. Soc.* **2007**, *129*, 14176-14177.

(30) Dincă, M.; Dailly, A.; Liu, Y.; Brown, C. M.; Neumann, D. A.; Long, J. R. *J. Am. Chem. Soc.* **2006**, *128*, 16876-16883.

(31) Rowsell, J. L. C.; Yaghi, O. M. *J. Am. Chem. Soc.* **2006**, *128*, 1304-1315.

(32) Furukawa, H.; Miller, M. A.; Yaghi, O. M. *J. Mater. Chem.* **2007**, *17*, 3197-3204.

(33) Nijkamp, M. G.; Raaymakers, J. E. M. J.; van Dillen, A. J.; de Jong, K. P. *Appl. Phys. A-Mater. Sci. Process.* **2001**, *72*, 619-623.

(34) Panella, B.; Hirscher, M.; Roth, S. *Carbon* **2005**, *43*, 2209-2214.

(35) Collins, D. J.; Zhou, H. C. *J. Mater. Chem.* **2007**, *17*, 3154-3160.

(36) Züttel, A.; Sudan, P.; Mauron, P.; Wenger, P. *Appl. Phys. A-Mater. Sci. Process.* **2004**, *78*, 941-946.

(37) Liu, Y.; Kabbour, H.; Brown, C. M.; Neumann, D. A.; Ahn, C. C. *Langmuir* **2008**, *24*, 4772-4777.

(38) Bénard, P.; Chahine, R. *Scr. Mater.* **2007**, *56*, 803-808.

(39) Wang, Q. Y.; Johnson, J. K. *J. Chem. Phys.* **1999**, *110*, 577-586.

(40) Peterson, V. K.; Liu, Y.; Brown, C. M.; Kepert, C. J. *J. Am. Chem. Soc.* **2006**, *128*, 15578-15579.

(41) Liu, Y.; Brown, C. M.; Neumann, D. A.; Peterson, V. K.; Kepert, C. J. *J. Alloy. Compd.* **2007**, *446*, 385-388.

(42) Panella, B.; Hönes, K.; Müller, U.; Trukhan, N.; Schubert, M.; Pütter, H.; Hirscher, M. *Angew. Chem., Int. Ed.* **2008**, *47*, 2138-2142.

(43) Han, S. S.; Deng, W. Q.; Goddard, W. A. *Angew. Chem., Int. Ed.* **2007**, *46*, 6289-6292.

(44) Sagara, T.; Ortony, J.; Ganz, E. *J. Chem. Phys.* **2005**, *123*, 214707.

(45) Wu, H.; Zhou, W.; Yildirim, T. *J. Am. Chem. Soc.* **2007**, *129*, 5314-5315.

(46) Mulder, F. M.; Dingemans, T. J.; Wagemaker, M.; Kearley, G. J. *Chem. Phys.* **2005**, *317*, 113-118.

(47) Chun, H.; Dybtsev, D. N.; Kim, H.; Kim, K. *Chem.-Eur. J.* **2005**, *11*, 3521-3529.

(48) Chen, B. L.; Eddaoudi, M.; Reineke, T. M.; Kampf, J. W.; O'Keeffe, M.; Yaghi, O. M. *J. Am. Chem. Soc.* **2000**, *122*, 11559-11560.

(49) Prestipino, C.; Regli, L.; Vitillo, J. G.; Bonino, F.; Damin, A.; Lamberti, C.; Zecchina, A.; Solari, P. L.; Kongshaug, K. O.; Bordiga, S. *Chem. Mat.* **2006**, *18*, 1337-1346.

(50) Dincă, M.; Han, W. S.; Liu, Y.; Dailly, A.; Brown, C. M.; Long, J. R. *Angew. Chem., Int. Ed.* **2007**, *46*, 1419-1422.

(51) Sun, Y. Y.; Kim, Y. H.; Zhang, S. B. *J. Am. Chem. Soc.* **2007**, *129*, 12606-12607.

(52) Dincă, M.; Long, J. R. *J. Am. Chem. Soc.* **2007**, *129*, 11172-11176.

(53) Yang, Q. Y.; Zhong, C. L. *J. Phys. Chem. B* **2006**, *110*, 655-658.

(54) Moon, H. R.; Kobayashi, N.; Suh, M. P. *Inorg. Chem.* **2006**, *45*, 8672-8676.

(55) Dincă, M.; Long, J. R. *J. Am. Chem. Soc.* **2005**, *127*, 9376-9377.

(56) Lochan, R. C.; Head-Gordon, M. *Phys. Chem. Chem. Phys.* **2006**, *8*, 1357-1370.

(57) Blomqvist, A.; Araújo, C. M.; Srepusharawoot, P.; Ahuja, R. *Proc. Natl. Acad. Sci. U. S. A.* **2007**, *104*, 20173-20176.

(58) Mulfort, K. L.; Hupp, J. T. *J. Am. Chem. Soc.* **2007**, *129*, 9604-9605.

(59) Trewin, A.; Darling, G. R.; Cooper, A. I. *New J. Chem.* **2008**, *32*, 17-20.

(60) Li, Y. W.; Yang, R. T. *J. Am. Chem. Soc.* **2006**, *128*, 726-727.

(61) Li, Y. W.; Yang, R. T. *J. Am. Chem. Soc.* **2006**, *128*, 8136-8137.

(62) Liu, Y. Y.; Zeng, J. L.; Zhang, J.; Xu, F.; Sun, L. X. *Int. J. Hydrog. Energy* **2007**, *32*, 4005-4010.

(63) Sabo, M.; Henschel, A.; Fröde, H.; Klemm, E.; Kaskel, S. *J. Mater. Chem.* **2007**, *17*, 3827-3832.

(64) Xiao, B.; Wheatley, P. S.; Zhao, X. B.; Fletcher, A. J.; Fox, S.; Rossi, A. G.; Megson, I. L.; Bordiga, S.; Regli, L.; Thomas, K. M.; Morris, R. E. *J. Am. Chem. Soc.* **2007**, *129*, 1203-1209.

(65) Broom, D. P. *Int. J. Hydrog. Energy* **2007**, *32*, 4871-4888.

(66) Navarro, J. A. R.; Barea, E.; Salas, J. M.; Masciocchi, N.; Galli, S.; Sironi, A.; Ania, C. O.; Parra, J. B. *Inorg. Chem.* **2006**, *45*, 2397-2399.

(67) Li, Y. W.; Yang, R. T. *AICHE J.* **2008**, *54*, 269-279.

(68) Panella, B.; Hirscher, M. *Adv. Mater.* **2005**, *17*, 538-541.

(69) Li, Y. W.; Yang, R. T. *Langmuir* **2007**, *23*, 12937-12944.

(70) Poirier, E.; Chahine, R.; Bénard, P.; Lafi, L.; Dorval-Douville, G.; Chandonia, P. A. *Langmuir* **2006**, *22*, 8784-8789.

(71) Frost, H.; Snurr, R. Q. *J. Phys. Chem. C* **2007**, *111*, 18794-18803.

(72) Frost, H.; Düren, T.; Snurr, R. Q. *J. Phys. Chem. B* **2006**, *110*, 9565-9570.

(73) Lin, X.; Jia, J. H.; Zhao, X. B.; Thomas, K. M.; Blake, A. J.; Walker, G. S.; Champness, N. R.; Hubberstey, P.; Schröder, M. *Angew. Chem., Int. Ed.* **2006**, *45*, 7358-7364.

(74) Culp, J. T.; Natesakhawat, S.; Smith, M. R.; Bittner, E.; Matranga, C.; Bockrath, B. *J. Phys. Chem. C* **2008**, *112*, 7079-7083.

(75) Hirscher, M.; Panella, B. *Scr. Mater.* **2007**, *56*, 809-812.

(76) Bhatia, S. K.; Myers, A. L. *Langmuir* **2006**, *22*, 1688-1700.

(77) Yildirim, T.; Hartman, M. R. *Phys. Rev. Lett.* **2005**, *95*, 215504.

(78) Mueller, T.; Ceder, G. *J. Phys. Chem. B* **2005**, *109*, 17974-17983.

(79) Bordiga, S.; Vitillo, J. G.; Ricchiardi, G.; Regli, L.; Cocina, D.; Zecchina, A.; Arstad, B.; Bjørgen, M.; Hafizovic, J.; Lillerud, K. P. *J. Phys. Chem. B* **2005**, *109*, 18237-18242.

(80) Garberoglio, G.; Skoulidas, A. I.; Johnson, J. K. *J. Phys. Chem. B* **2005**, *109*, 13094-13103.

(81) Liu, Y. L.; Eubank, J. F.; Cairns, A. J.; Eckert, J.; Kravtsov, V. C.; Luebke, R.; Eddaoudi, M. *Angew. Chem., Int. Ed.* **2007**, *46*, 3278-3283.

(82) Sava, D. F.; Kravtsov, V. C.; Nouar, F.; Wojtas, L.; Eubank, J. F.; Eddaoudi, M. *J. Am. Chem. Soc.* **2008**, *130*, 3768-3770.

(83) Belof, J. L.; Stern, A. C.; Eddaoudi, M.; Space, B. *J. Am. Chem. Soc.* **2007**, *129*, 15202-15210.

(84) Simonyan, V. V.; Diep, P.; Johnson, J. K. *J. Chem. Phys.* **1999**, *111*, 9778-9783.

(85) Yoon, M.; Yang, S. Y.; Wang, E. G.; Zhang, Z. Y. *Nano Lett.* **2007**, *7*, 2578-2583.

(86) Menon, V. C.; Komarneni, S. *J. Porous Mat.* **1998**, *5*, 43-58.

(87) Wegrzyn, J.; Gurevich, M. *Appl. Energy* **1996**, *55*, 71-83.

(88) Kondo, M.; Yoshitomi, T.; Seki, K.; Matsuzaka, H.; Kitagawa, S. *Angew. Chem., Int. Ed.* **1997**, *36*, 1725-1727.

(89) Düren, T.; Sarkisov, L.; Yaghi, O. M.; Snurr, R. Q. *Langmuir* **2004**, *20*, 2683-2689.

(90) Ma, S. Q.; Sun, D. F.; Simmons, J. M.; Collier, C. D.; Yuan, D. Q.; Zhou, H. C. *J. Am. Chem. Soc.* **2008**, *130*, 1012-1016.

(91) Senkovska, I.; Kaskel, S. *Microporous Mesoporous Mat.* **2008**, *112*, 108-115.

(92) Haszeldine, R. S. *Science* **2009**, *325*, 1647-1652.

(93) Ma, S. Q.; Zhou, H. C. *Chem. Commun.* **2010**, *46*, 44-53.

(94) Llewellyn, P. L.; Bourrelly, S.; Serre, C.; Vimont, A.; Daturi, M.; Hamon, L.; De Weireld, G.; Chang, J. S.; Hong, D. Y.; Hwang, Y. K.; Jhung, S. H.; Férey, G. *Langmuir* **2008**, *24*, 7245-7250.

(95) Millward, A. R.; Yaghi, O. M. *J. Am. Chem. Soc.* **2005**, *127*, 17998-17999.

(96) Demessence, A.; D'Alessandro, D. M.; Foo, M. L.; Long, J. R. *J. Am. Chem. Soc.* **2009**, *131*, 8784-8786.

(97) Férey, G. *J. Solid State Chem.* **2000**, *152*, 37-48.

(98) Mellot-Draznieks, C.; Dutour, J.; Férey, G. *Angew. Chem., Int. Ed.* **2004**, *43*, 6290-6296.

(99) Férey, G.; Mellot-Draznieks, C.; Serre, C.; Millange, F. *Accounts Chem. Res.* **2005**, *38*, 217-225.

(100) Eddaoudi, M.; Moler, D. B.; Li, H. L.; Chen, B. L.; Reineke, T. M.; O'Keeffe, M.; Yaghi, O. M. *Accounts Chem. Res.* **2001**, *34*, 319-330.

(101) Ockwig, N. W.; Delgado-Friedrichs, O.; O'Keeffe, M.; Yaghi, O. M. *Accounts Chem. Res.* **2005**, *38*, 176-182.

(102) O'Keeffe, M.; Peskov, M. A.; Ramsden, S. J.; Yaghi, O. M. *Accounts Chem. Res.* **2008**, *41*, 1782-1789.

(103) Chae, H. K.; Siberio-Pérez, D. Y.; Kim, J.; Go, Y. B.; Eddaoudi, M.; Matzger, A. J.; O'Keeffe, M.; Yaghi, O. M. *Nature* **2004**, *427*, 523-527.

(104) Walton, K. S.; Snurr, R. Q. *J. Am. Chem. Soc.* **2007**, *129*, 8552-8556.

(105) Han, S. S.; Goddard, W. A. *J. Phys. Chem. C* **2008**, *112*, 13431-13436.

(106) Wang, X. S.; Ma, S. Q.; Sun, D. F.; Parkin, S.; Zhou, H. C. *J. Am. Chem. Soc.* **2006**, *128*, 16474-16475.

(107) Ma, S. Q.; Sun, D. F.; Ambrogio, M.; Fillinger, J. A.; Parkin, S.; Zhou, H. C. *J. Am. Chem. Soc.* **2007**, *129*, 1858-1859.

(108) Moulton, B.; Zaworotko, M. J. *Chem. Rev.* **2001**, *101*, 1629-1658.

(109) Seidel, S. R.; Stang, P. J. *Accounts Chem. Res.* **2002**, *35*, 972-983.

(110) Fujita, M.; Tominaga, M.; Hori, A.; Therrien, B. *Accounts Chem. Res.* **2005**, *38*, 371-380.

(111) Lu, J. J.; Mondal, A.; Moulton, B.; Zaworotko, M. J. *Angew. Chem., Int. Ed.* **2001**, *40*, 2113-2116.

(112) McManus, G. J.; Wang, Z. Q.; Zaworotko, M. J. *Cryst. Growth Des.* **2004**, *4*, 11-13.

(113) Perry, J. J.; Kravtsov, V. C.; McManus, G. J.; Zaworotko, M. J. *J. Am. Chem. Soc.* **2007**, *129*, 10076-10077.

(114) Cairns, A. J.; Perman, J. A.; Wojtas, L.; Kravtsov, V. C.; Alkordi, M. H.; Eddaoudi, M.; Zaworotko, M. J. *J. Am. Chem. Soc.* **2008**, *130*, 1560-1561.

(115) Nouar, F.; Eubank, J. F.; Bousquet, T.; Wojtas, L.; Zaworotko, M. J.; Eddaoudi, M. *J. Am. Chem. Soc.* **2008**, *130*, 1833-1835.

(116) Chun, H. *J. Am. Chem. Soc.* **2008**, *130*, 800-801.

(117) Zou, Y.; Park, M.; Hong, S.; Lah, M. S. *Chem. Commun.* **2008**, 2340-2342.

(118) Wang, X. S.; Ma, S. Q.; Forster, P. M.; Yuan, D. Q.; Eckert, J.; López, J. J.; Murphy, B. J.; Parise, J. B.; Zhou, H. C. *Angew. Chem., Int. Ed.* **2008**, *47*, 7263-7266.

(119) Aujard, I.; Baltaze, J. P.; Baudin, J. B.; Cogné, E.; Ferrage, F.; Jullien, L.; Perez, E.; Prévost, V.; Qian, L. M.; Ruel, O. *J. Am. Chem. Soc.* **2001**, *123*, 8177-8188.

(120) McIlroy, S. P.; Cló, E.; Nikolajsen, L.; Frederiksen, P. K.; Nielsen, C. B.; Mikkelsen, K. V.; Gothelf, K. V.; Ogilby, P. R. *J. Org. Chem.* **2005**, *70*, 1134-1146.

(121) Weber, E.; Hecker, M.; Koepp, E.; Orlia, W.; Czugler, M.; Csoregh, I. *J. Chem. Soc., Perkin Trans. 2* **1988**, 1251-1257.

(122) Sheldrick, G. M. *SHELXTL*, version 6.14; Bruker AXS: Madison, WI, 2003.

(123) Spek, A. L. *J. Appl. Crystallogr.* **2003**, *36*, 7-13.

(124) Férey, G.; Serre, C.; Mellot-Draznieks, C.; Millange, F.; Surblé, S.; Dutour, J.; Margiolaki, I. *Angew. Chem., Int. Ed.* **2004**, *43*, 6296-6301.

(125) Férey, G.; Mellot-Draznieks, C.; Serre, C.; Millange, F.; Dutour, J.; Surblé, S.; Margiolaki, I. *Science* **2005**, *309*, 2040-2042.

(126) Horcajada, P.; Surblé, S.; Serre, C.; Hong, D. Y.; Seo, Y. K.; Chang, J. S.; Grenèche, J. M.; Margiolaki, I.; Férey, G. *Chem. Commun.* **2007**, 2820-2822.

(127) Fang, Q. R.; Zhu, G. S.; Jin, Z.; Ji, Y. Y.; Ye, J. W.; Xue, M.; Yang, H.; Wang, Y.; Qiu, S. L. *Angew. Chem., Int. Ed.* **2007**, *46*, 6638-6642.

(128) Park, Y. K.; Choi, S. B.; Kim, H.; Kim, K.; Won, B. H.; Choi, K.; Choi, J. S.; Ahn, W. S.; Won, N.; Kim, S.; Jung, D. H.; Choi, S. H.; Kim, G. H.; Cha, S. S.; Jhon, Y. H.; Yang, J. K.; Kim, J. *Angew. Chem., Int. Ed.* **2007**, *46*, 8230-8233.

(129) Koh, K.; Wong-Foy, A. G.; Matzger, A. J. *Angew. Chem., Int. Ed.* **2008**, *47*, 677-680.

(130) Brunauer, S.; Emmett, P. H.; Teller, E. *J. Am. Chem. Soc.* **1938**, *60*, 309-319.

(131) Koh, K.; Wong-Foy, A. G.; Matzger, A. J. *J. Am. Chem. Soc.* **2009**, *131*, 4184-4185.

(132) Chui, S. S. Y.; Lo, S. M. F.; Charmant, J. P. H.; Orpen, A. G.; Williams, I. D. *Science* **1999**, *283*, 1148-1150.

(133) Sun, D. F.; Ma, S. Q.; Ke, Y. X.; Collins, D. J.; Zhou, H. C. *J. Am. Chem. Soc.* **2006**, *128*, 3896-3897.

(134) Ma, L. Q.; Mihalcik, D. J.; Lin, W. B. *J. Am. Chem. Soc.* **2009**, *131*, 4610-4612.

(135) Murray, L. J.; Dinca, M.; Long, J. R. *Chem. Soc. Rev.* **2009**, *38*, 1294-1314.

(136) Klein, N.; Senkovska, I.; Gedrich, K.; Stoeck, U.; Henschel, A.; Mueller, U.; Kaskel, S. *Angew. Chem., Int. Ed.* **2009**, *48*, 9954-9957.

(137) Mueller, U.; Schubert, M.; Teich, F.; Puetter, H.; Schierle-Arndt, K.; Pastré, J. *J. Mater. Chem.* **2006**, *16*, 626-636.

(138) Robson, R. *Dalton Trans.* **2008**, 5113-5131.

(139) Czaja, A. U.; Trukhan, N.; Muller, U. *Chem. Soc. Rev.* **2009**, *38*, 1284-1293.

(140) Rowsell, J. L. C.; Yaghi, O. M. *Angew. Chem., Int. Ed.* **2005**, *44*, 4670-4679.

(141) Eddaoudi, M.; Kim, J.; Rosi, N.; Vodak, D.; Wachter, J.; O'Keeffe, M.; Yaghi, O. M. *Science* **2002**, *295*, 469-472.

(142) Wang, X. S.; Ma, S. Q.; Rauch, K.; Simmons, J. M.; Yuan, D. Q.; Wang, X. P.; Yildirim, T.; Cole, W. C.; López, J. J.; de Meijere, A.; Zhou, H. C. *Chem. Mat.* **2008**, *20*, 3145-3152.

(143) Wu, H.; Zhou, W.; Yildirim, T. *J. Am. Chem. Soc.* **2009**, *131*, 4995-5000.

(144) Lin, X.; Telepeni, I.; Blake, A. J.; Dailly, A.; Brown, C. M.; Simmons, J. M.; Zoppi, M.; Walker, G. S.; Thomas, K. M.; Mays, T. J.; Hubberstey, P.; Champness, N. R.; Schroder, M. *J. Am. Chem. Soc.* **2009**, *131*, 2159-2171.

(145) Chen, B. L.; Ockwig, N. W.; Millward, A. R.; Contreras, D. S.; Yaghi, O. M. *Angew. Chem., Int. Ed.* **2005**, *44*, 4745-4749.

(146) Lee, Y. G.; Moon, H. R.; Cheon, Y. E.; Suh, M. P. *Angew. Chem., Int. Ed.* **2008**, *47*, 7741-7745.

(147) Xue, M.; Zhu, G. S.; Li, Y. X.; Zhao, X. J.; Jin, Z.; Kang, E.; Qiu, S. L. *Cryst. Growth Des.* **2008**, *8*, 2478-2483.

(148) Hu, Y. X.; Xiang, S. C.; Zhang, W. W.; Zhang, Z. X.; Wang, L.; Bai, J. F.; Chen, B. L. *Chem. Commun.* **2009**, 7551-7553.

(149) Sun, D. F.; Ma, S. Q.; Simmons, J. M.; Li, J. R.; Yuan, D. Q.; Zhou, H. C. *Chem. Commun.* **2010**, *46*, 1329-1331.

(150) Ma, S. Q.; Simmons, J. M.; Sun, D. F.; Yuan, D. Q.; Zhou, H. C. *Inorg. Chem.* **2009**, *48*, 5263-5268.

(151) Sheldrick, G. M. *SADABS*, version 2008/1; Bruker AXS: Madison, WI, 1998.

(152) Zhang, X. M. *Coord. Chem. Rev.* **2005**, *249*, 1201-1219.

(153) Chen, X. M.; Tong, M. L. *Accounts Chem. Res.* **2007**, *40*, 162-170.

(154) Glaser, C. *Ber. Dtsch. Chem. Ges.* **1869**, *2*, 422-424.

(155) Horvath, G.; Kawazoe, K. *J. Chem. Eng. Japan* **1983**, *16*, 470-475.

(156) Burchell, T.; Rogers, M. *SAE Tech. Pap. Ser.* **2000**, 2000-2001-2205.

(157) Figueroa, J. D.; Fout, T.; Plasynski, S.; McIlvried, H.; Srivastava, R. D. *Int. J. Greenh. Gas Control* **2008**, *2*, 9-20.

(158) Pierantozzi, R. *Kirk-Othmer Encyclopedia of Chemical Technology*; John Wiley & Sons, Inc.: Weinheim, 2003.

(159) Yang, R. T. *Gas Separation by Adsorption Processes*; Imperial College Press: London, 1997.

(160) Kuznicki, S. M.; Bell, V. A.; Nair, S.; Hillhouse, H. W.; Jacubinas, R. M.; Braunbarth, C. M.; Toby, B. H.; Tsapatsis, M. *Nature* **2001**, *412*, 720-724.

(161) Ma, S. Q.; Sun, D. F.; Wang, X. S.; Zhou, H. C. *Angew. Chem., Int. Ed.* **2007**, *46*, 2458-2462.

(162) Ma, S. Q.; Sun, D. F.; Yuan, D. Q.; Wang, X. S.; Zhou, H. C. *J. Am. Chem. Soc.* **2009**, *131*, 6445-6451.

(163) Li, J. R.; Kuppler, R. J.; Zhou, H. C. *Chem. Soc. Rev.* **2009**, *38*, 1477-1504.

(164) Rondeau, R. E. *J. Chem. Eng. Data* **1966**, *11*, 124.

(165) Rappe, A. K.; Casewit, C. J.; Colwell, K. S.; Goddard, W. A.; Skiff, W. M. *J. Am. Chem. Soc.* **1992**, *114*, 10024-10035.

(166) Mayo, S. L.; Olafson, B. D.; Goddard, W. A. *J. Phys. Chem.* **1990**, *94*, 8897-8909.

(167) Ryckaert, J. P.; Bellemans, A. *Faraday Discuss.* **1978**, 95-106.

(168) Dubbeldam, D.; Calero, S.; Vlugt, T. J. H.; Krishna, R.; Maesen, T. L. M.; Smit, B. *J. Phys. Chem. B* **2004**, *108*, 12301-12313.

(169) Skoulidas, A. I.; Sholl, D. S. *J. Phys. Chem. B* **2002**, *106*, 5058-5067.

(170) Vlugt, T. J. H.; Krishna, R.; Smit, B. *J. Phys. Chem. B* **1999**, *103*, 1102-1118.

(171) Calero, S.; Dubbeldam, D.; Krishna, R.; Smit, B.; Vlugt, T. J. H.; Denayer, J. F. M.; Martens, J. A.; Maesen, T. L. M. *J. Am. Chem. Soc.* **2004**, *126*, 11377-11386.

(172) Myers, A. L.; Prausnitz, J. M. *AICHE J.* **1965**, *11*, 121-127.

(173) Larsen, R. W. *J. Am. Chem. Soc.* **2008**, *130*, 11246-11247.

(174) Krishna, R. *J. Phys. Chem. C* **2009**, *113*, 19756-19781.

(175) Krishna, R.; van Baten, J. M. *Chem. Eng. Sci.* **2008**, *63*, 3120-3140.

(176) Krishna, R.; van Baten, J. M. *Chem. Eng. Sci.* **2009**, *64*, 3159-3178.

(177) Nguyen, T. X.; Bhatia, S. K. *J. Phys. Chem. C* **2007**, *111*, 2212-2222.

(178) Zhang, J. P.; Chen, X. M. *J. Am. Chem. Soc.* **2008**, *130*, 6010-6017.

(179) Maggs, F. A. P. *Nature* **1952**, *169*, 793-794.

(180) Maggs, F. A. P. *Res. Corresp.* **1953**, *6*, 13S-14S.

(181) Breck, D. W.; Eversole, W. G.; Milton, R. M.; Reed, T. B.; Thomas, T. L. *J. Am. Chem. Soc.* **1956**, *78*, 5963-5971.

(182) Kim, H.; Samsonenko, D. G.; Yoon, M.; Yoon, J. W.; Hwang, Y. K.; Chang, J. S.; Kim, K. *Chem. Commun.* **2008**, 4697-4699.

(183) Bae, Y. S.; Farha, O. K.; Hupp, J. T.; Snurr, R. Q. *J. Mater. Chem.* **2009**, *19*, 2131-2134.

(184) Nakagawa, K.; Tanaka, D.; Horike, S.; Shimomura, S.; Higuchi, M.; Kitagawa, S. *Chem. Commun.* **2010**, *46*, 4258-4260.

(185) Nguyen, T. X.; Bhatia, S. K. *Langmuir* **2008**, *24*, 146-154.

(186) Krishna, R.; van Baten, J. M. *J. Membr. Sci.* **2010**, *360*, 323-333.

(187) Yoshizawa, M.; Klosterman, J. K.; Fujita, M. *Angew. Chem., Int. Ed.* **2009**, *48*, 3418-3438.

(188) Northrop, B. H.; Zheng, Y. R.; Chi, K. W.; Stang, P. J. *Accounts Chem. Res.* **2009**, *42*, 1554-1563.

(189) Pluth, M. D.; Bergman, R. G.; Raymond, K. N. *Accounts Chem. Res.* **2009**, *42*, 1650-1659.

(190) Wang, Z. Q.; Cohen, S. M. *Chem. Soc. Rev.* **2009**, *38*, 1315-1329.

(191) Zhao, Y. L.; Dichtel, W. R.; Trabolsi, A.; Saha, S.; Aprahamian, I.; Stoddart, J. F. *J. Am. Chem. Soc.* **2008**, *130*, 11294-11296.

(192) Gao, H. F.; Matyjaszewski, K. *J. Am. Chem. Soc.* **2007**, *129*, 6633-6639.

(193) Kolb, H. C.; Finn, M. G.; Sharpless, K. B. *Angew. Chem., Int. Ed.* **2001**, *40*, 2004-2021.

(194) Goto, Y.; Sato, H.; Shinkai, S.; Sada, K. *J. Am. Chem. Soc.* **2008**, *130*, 14354-14355.

(195) Gadzikwa, T.; Lu, G.; Stern, C. L.; Wilson, S. R.; Hupp, J. T.; Nguyen, S. T. *Chem. Commun.* **2008**, 5493-5495.

(196) Gadzikwa, T.; Farha, O. K.; Malliakas, C. D.; Kanatzidis, M. G.; Hupp, J. T.; Nguyen, S. T. *J. Am. Chem. Soc.* **2009**, *131*, 13613-13615.

(197) Zhao, X. B.; Xiao, B.; Fletcher, A. J.; Thomas, K. M.; Bradshaw, D.; Rosseinsky, M. J. *Science* **2004**, *306*, 1012-1015.

(198) Steiner, T.; Starikov, E. B.; Amado, A. M.; Teixeira-Dias, J. J. C. *J. Chem. Soc., Perkin Trans. 2* **1995**, 1321-1326.

(199) Tonnet, M. L.; Yamada, S.; Ross, I. G. *Trans. Faraday Soc.* **1964**, *60*, 840-849.

(200) Larsen, R. W.; McManus, G. J.; Perry, J. J.; Rivera-Otero, E.; Zaworotko, M. J. *Inorg. Chem.* **2007**, *46*, 5904-5910.

(201) Low, J. J.; Benin, A. I.; Jakubczak, P.; Abrahamian, J. F.; Faheem, S. A.; Willis, R. R. *J. Am. Chem. Soc.* **2009**, *131*, 15834-15842.

(202) Gohy, J. F. *Coord. Chem. Rev.* **2009**, *253*, 2214-2225.

(203) Sato, S.; Ishido, Y.; Fujita, M. *J. Am. Chem. Soc.* **2009**, *131*, 6064-6065.

(204) Longley, D. B.; Harkin, D. P.; Johnston, P. G. *Nat. Rev. Cancer* **2003**, *3*, 330-338.

(205) Schwert, D. D.; Davies, J. A.; Richardson, N. *Top. Curr. Chem.* **2002**, *221*, 165-199.

VITA

Dan Zhao was born in Anhui, China. He received his B.S. degree in polymer materials and engineering (2003) and M.S. degree in polymer chemistry & physics (2006) from Zhejiang University. After that, he joined Professor Hong-Cai Zhou's group as a graduate student, first at Miami University from 2006 to 2008, and then at Texas A&M University from 2008 to 2010 when he graduated with his Ph.D. His research interests include metal-organic nanoporous materials and their applications in gas storage and gas separation for clean and renewable energy applications.

Dr. Zhao can be reached at the following address after graduation:

Dan Zhao

Department of Chemistry

Texas A&M University

PO Box 30012

College Station, TX 77842-3012